Chair of Geology and Economic Geology

Master's Thesis

The Geochemical Landscape of the Arno River Basin (Tuscany, Italy)

Petra Diendorfer, BSc

March 2021

MONTANUNIVERSITÄT LEOBEN
www.unileoben.ac.at

EIDESSTATTLICHE ERKLÄRUNG

Ich erkläre an Eides statt, dass ich diese Arbeit selbständig verfasst, andere als die angegebenen Quellen und Hilfsmittel nicht benutzt, und mich auch sonst keiner unerlaubten Hilfsmittel bedient habe.

Ich erkläre, dass ich die Richtlinien des Senats der Montanuniversität Leoben zu "Gute wissenschaftliche Praxis" gelesen, verstanden und befolgt habe.

Weiters erkläre ich, dass die elektronische und gedruckte Version der eingereichten wissenschaftlichen Abschlussarbeit formal und inhaltlich identisch sind.

Datum 16.02.2021

Unterschrift Verfasser/in
Petra Diendorfer

ABSTRACT

The Arno River Basin is the second largest catchment in central Italy with a drainage area of 8,228 km^2. A total of 33 stream sediment samples of the Arno river, and its main tributaries, were analyzed to characterize its geochemical landscape. Major and trace elements' geochemistry was examined and the magnetic susceptibility was measured to detect metallic anomalies. The obtained data were analyzed using the Compositional Data Analysis approach by combining Robust Factor Analysis with the calculation of the Robust Mahalanobis distance, which have proven to be effective tools to explain compositional changes throughout the basin. The investigated stream sediment data correlate well with the major geological units, but certain locations are affected by anthropogenic contaminations. The stream sediment composition of the upper reaches is mainly determined by the weathering of the bedrock. Major changes are observed in the Chiana valley, where industrial and agricultural activities are considered to be significant sources of contaminants. The rivers Era, Greve, Pesa, Elsa, Egola and Era around and downstream Florence, are mainly influenced by the weathering of ophiolitic rocks and to a minor extent by carbonates. P and Cu anomalies, resulting from industrial settlements and horticulture (flower and plant gardens), characterize the Ombrone, Bisenzio and Usciana rivers. Overall, stream sediments of tributaries are more affected by compositional changes than those of the main course, suggesting the Arno river sediments to be more resilient to geochemical threats.

ZUSAMMENFASSUNG

Die geochemische Landschaft des Arnoflussbeckens (Toskana, Italien)

Das Arnoflussbecken stellt mit einer Größe von 8.228 km^2 das zweitgrößte Einzugsgebiet in Zentralitalien dar. Um die geochemische Landschaft dieses Flusssystemes zu charakterisieren und zu erklären, wurden 33 Bachsedimentproben des Arnos und seiner Hauptzuflüsse untersucht. Es wurden sowohl die Haupt- und Spurenelemente unter Berücksichtigung ihrer kompositionellen Natur analysiert, als auch die magnetische Suszeptibilität gemessen, um metallische Anomalien aufzudecken. Die gewonnenen Daten wurden mittels kompositioneller Datenanalyse, durch die Kombination von robuster Faktoranalyse und der Berechnung der robusten Mahalanobis Distanzen ausgewertet, was sich als effektives Werkzeug zur Erklärung kompositioneller Änderungen entlang des Flusses bewährt. Die geochemische Zusammensetzung der Bachsedimente korreliert gut mit der geologischen Zusammensetzung des Einzugsgebietes, jedoch werden manche Bereiche durch anthropogene Kontaminationen überprägt. Während die Bachsedimente der oberen Teile des Flussbeckens durch das unterliegende Gestein charakterisiert werden, können im Chiana-Tal Veränderungen, hervorgerufen durch industrielle und landwirtschaftliche Aktivitäten, beobachtet werden. Die Flüsse Era, Greve, Pesa, Elsa, Egola und Era, die sich in der Umgebung und flussabwärts von Florenz befinden, werden hauptsächlich ophiolitisch, aber auch in geringerem Ausmaß karbonatisch beeinflusst. P und Cu Anomalien sind auf industrielle Einflüsse, sowie Garten- und Landschaftsbau zurückzuführen und kontaminieren die Flüsse Ombrone, Bisenzio und Usciana. Die Bachsedimente der Zuflüsse sind insgesamt stärker durch kompositionelle Veränderungen beeinflusst als der Hauptfluss, wodurch auf eine höhere geochemische Widerstandsfähigkeit der Arnosedimente geschlossen wird.

ACKNOWLEDGMENTS

Special thanks to Prof. Gerd Rantitsch for the very patient supervision, support and all the constructive talks. Many thanks to Dr. Caterina Gozzi and Prof. Antonella Buccianti for the collaboration and support not only during my stay in Florence, but also for all the help during those unexpected times, I really appreciate it. Furthermore, I would like to express my gratitude to Prof. Barbara Nisi, Prof. Orlando Vaselli, Dr. Caterina Gozzi and Anna Bauer for all the support during the sampling campaign. Special thanks to my dear friend Anna Bauer for taking on this project with me, thanks for all the help in the lab, field and the many conversations. My thanks are also adressed to Prof. Robert Scholger, who helped with the analysis of the magnetic susceptibility. I am especially grateful for my family, who made everything possible and for my sister Carina with her awesome moral support. Finally, I want to thank my dear Jakub, for always being there for me and all his encouragement.

Table of Contents

Chapter One

Introduction

The geochemical analysis of stream sediments is an important tool to investigate river systems. They are traditionally examined to explore mineral deposits (Levinson, 1974), but can also be used for research problems related to the environment (e.g. Howarth and Thornton, 1983; Förstner, 1983).

Stream sediments substantially reflect the mineralogical composition and the presence of rock types in the catchment upstream its sampling location (Rose et al., 1979). The lithological and morphological setting of the catchment are one of the major controlling factors influencing the chemistry of stream sediments (Rantitsch, 2001). Furthermore, climate plays a vital role in a basin, since precipitation controls not only weathering rates and erosion of bedrock and soils, but also characterizes the prevailing vegetation cover (e.g. Salomons and Förstner, 1984). Grassi et al. (2007) proposes a reduced flow in the major rivers in Tuscany during the last century due to a long term trend of decreasing precipitation. Anthropogenic activities, on the other hand, are another important influencing factor, which depend on land use, population density, pollution and other parameters (Berner and Berner, 1996). Weathering processes connected to ore deposits or other rocks with special compositions occasionally lead to natural pollutions.

There are two options for the disposition of contaminants within a river system:

- Stream sediments can act as a sink and pollutants are stored within the bed load,

where they can turn into a pollution source themselves, eventually.

- Stream sediments can act as a carrier and pollutants are transported away from their source.

This work is a collaboration project with Dr. Caterina Gozzi and Prof. Antonella Buccianti from the Università degli Studi di Firenze and focuses on the stream sediments of the Arno river basin (ARB) in Tuscany (Italy), considering the compositional nature of the analyzed geochemical data (Aitchison, 1986). The used methods follow the example of Gozzi (2020), in order to obtain comparable results and to find similarities and universal behaviors of stream sediments from different basins. This study aims to reveal the processes that characterize the geochemical landscape of the ARB to understand the physical and chemical weathering processes of the river system. Possible contaminations and their origins are discussed as well.
Some results of this study were presented at the EGU General Assembly 2020 (see Appendix D).

Chapter Two

Background

2.1 General Setting of the Arno River Basin

Geographically, the ARB lies almost completely within the region Tuscany (Italy), which borders the regions of Liguria to the northwest, Emilia-Romagna to the north, Marche to the northeast, Umbria to the east and Lazio to the southeast. The western border is set by the Tyrrhenian sea (Fig. 1). 1.6% of the catchment is located in the region Umbria.
The Arno river basin has a size of 8,228 km^2. 86% of that area lies underneath an elevation of 600m and has an average elevation of 353m. The highest peaks reach up to 1,650m and are located in the northeastern part of basin along the Apennine chain. 15% of the basin are composed of low mountain areas, 68% of hilly landscapes and 17% are lowlands (Cencetti and Tacconi, 2005). The 242km long Arno river flows from E to W - from the Apennines mountain ridge to the Tyrrhenian Sea. It has an average slope slightly below 0.06%, is the 8th longest river in Italy and crosses the provinces of Arezzo, the Metropolitan City of Florence and the province of Pisa. The Arno is the biggest river in Tuscany and after the Tiber river also the most important one in central Italy, regarding its length.

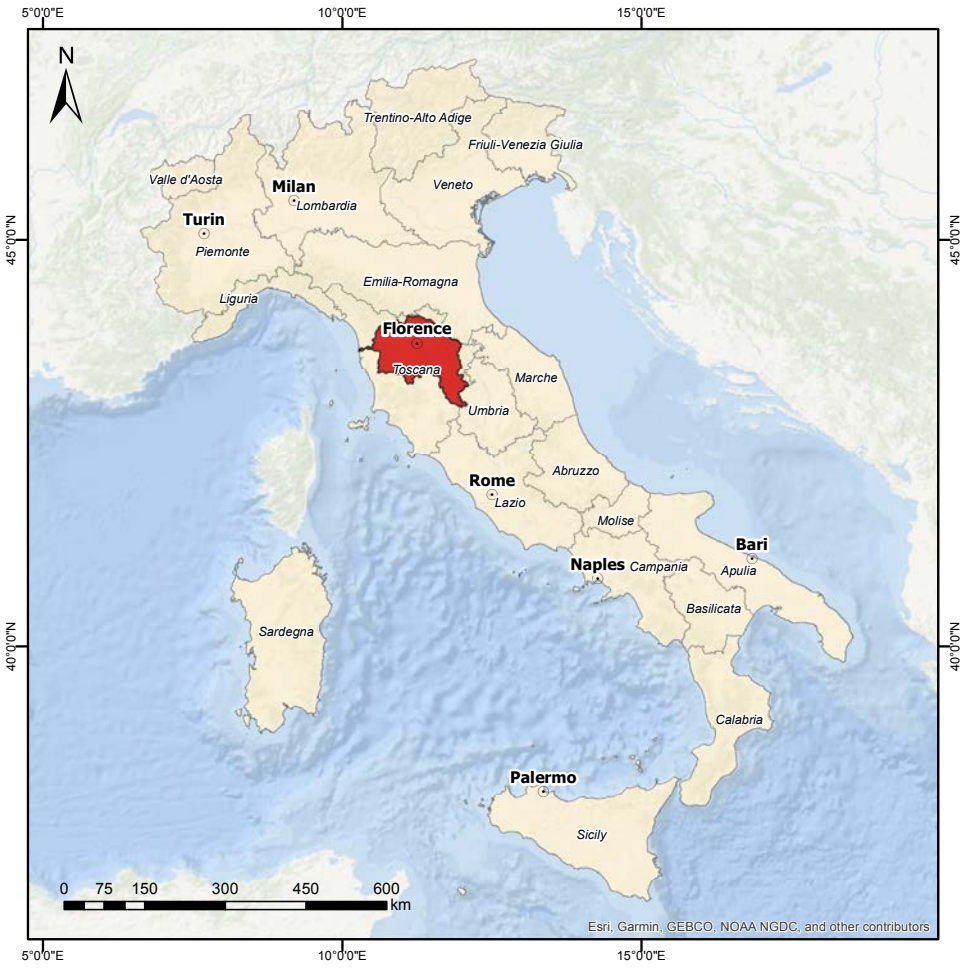

Figure 1 Location of the catchment within Italy. Modified map based on ISPRA (2020).

The Arno river originates on Monte Falterona at an elevation of 1,385m, located in the Casentino area of the Northern Apennines (Fig. 2). On the way towards its mouth into the Tyrrhenian sea at Marina di Pisa, many tributaries flow into the river, including Sieve, Bisenzio, Ombrone and Usciana from the right-hand bank of the main course and Chiana, Era, Elsa, Pesa and Pescia from the left-hand bank. Along the way to the mouth it flows through the towns of Florence and Pisa. The basin's geomorphological borders are the Tuscan-Emilian Apennine ridge to the N and E and the Chianti hills and Colline Metallifere hills in the southern part of the basin.

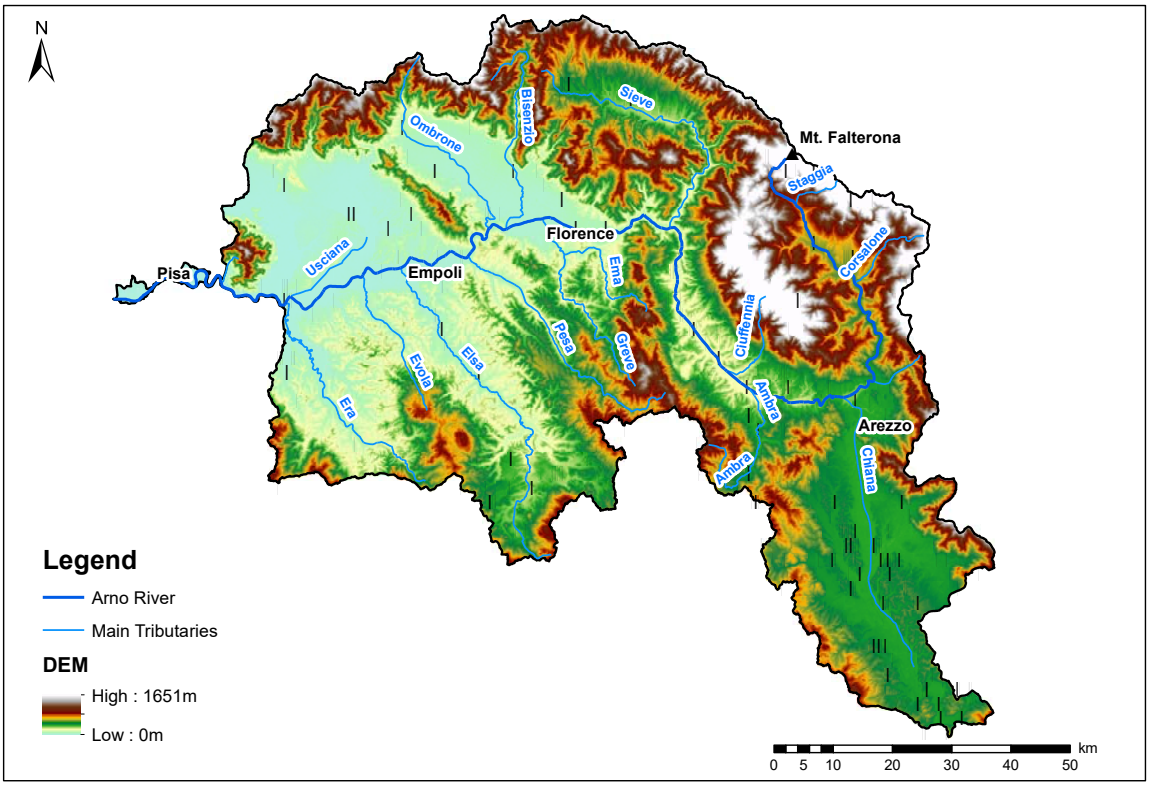

Figure 2 Modified geomorphological map of the Arno river basin based on ISPRA (2020) showing its main tributaries, source and bigger towns within the catchment area.

2.2 Climate and Hydrology

Near the coast, the climate within the ARB is Mediterranean and sub-littoral in the hinterland. The mean annual air temperature ranges between 15°C at the coast and 11°C behind at an elevation of about 1,000m. The maximum and minimum mean temperatures occur in July and January with 20°C and 4°C. The annual precipitation generally ranges between 600mm (mainly in the lowlands) and a maximum of 3,000mm on the Apennine ridge (Pranzini, 1994). According to Nardi (1993), the flow at S. Giovanni alla Vena station (near Pisa) amounts 90m^3/sec for an average flow, 2.2m^3/sec for a minimum flow and 2,250m^3/sec

for a maximum flow.

2.3 Geological Setting

Due to the geology of the Apennine chain (e.g. Elter et al., 1975; Boccaletti and Coli, 1983; Carmignani et al., 1994), the ARB is mainly composed of Mesozoic and Cenozoic metasediments (e.g. Abbate et al., 1992; Moretti, 1994). Conti et al. (2020) summarize five tectonic phases of relevance in the ARB, from oldest to youngest:

- Carboniferous Variscan phases that formed the Variscan chain
- Jurassic extension lead to the opening of the Piedmont-Ligurian ocean
- Late Cretaceous-Paleogene Ligurian phases form the closure of the Piedmont-Ligurian ocean and the total subduction of oceanic crust
- Miocene Tuscan phases, where the Ligurian units were emplaced on the Tuscan Domain
- Miocene-Quarternary tectonics of the Tyrrhenian margin (change of tectonic regime from compressional to extensional)

In the investigated area, following nappes of the Northern Apennines are found (from the footwall): the Tuscan Metamorphic Units, the Tuscan Nappe, the Ligurian Units and the post-orogenic sedimentary succession from Middle Miocene to Quaternary.
Tuscan metamorphic units represent the Variscan tectonic phase within the catchment area. In the ARB, they occur in the Monte Pisani area along the Zambra tributary, which is located right-hand the Arno river in the north of Pisa (Fig. 3). This area is dominated by alternating albite-bearing chlorite-phyllite and quartzite Paleozoic formations (Bagnoli et al., 1979). The headwaters of the Elsa tributary are dominated by metamorphic cherty limestones, calcschists, metaradiolarites, phyllites and metacalcarenites as well as dolostones, dolomitic marbles and marbles. They also belong to the Tuscan metamorphic units and show

a Late Triassic to Early Jurassic age (Rau and Tongiorgi, 1974).

Sandstones of Oligocene-Miocene arenaceous flysches (Andreozzi and Di Giulio, 1994; Dinelli et al., 1999a) are prevalent in the upper part of the basin and the source areas of the side tributaries Bisenzio, Pesa, Greve and partly Sieve. According to Carmignani et al. (2013), those sandstones are part of the Tuscan Nappe and Cervarola Unit.

The Ligurian domain is found in the central part around Florence as well as in the southern part of the basin. Those areas are dominated by Cretaceous-Paleocene sandstones, shales and calcareous rocks interbedded with clay with scattered ophiolitic blocks, mainly serpentinites (Abbate et al., 1992).

Pre-evaporitic Messinian marine deposits, evaporitic and post-Messinian lacustrine and lagoonal deposits are found in the headwaters of the rivers Elsa, Egola and Era (Dinelli et al., 1999b).

The Chiana valley, which is characterized as the most important tributary of the Arno river in the upper section, is shaped by marls, clay and minor sandstones belonging to a sequence of Plio-Pleistocene marine, continental and lacustrine deposits (Aruta et al., 2003). The plain area, located from Florence to the lower sections of the Bisenzio and Ombrone rivers, consists of clastic deposits, belonging to a Late Pleistocene lacustrine basin (Capecchi et al., 1975; Bossio et al., 1993). The right-bank tributaries downstream Florence, comprising the catchments of the Bisenzio, Ombrone and Usciana rivers, are dominated by sandstones of the Macigno Formation and cherty limestones. The lower sections of the main left-side tributaries (Greve, Egola, Pesa, Elsa and Era) drain Plio-Quaternary fine-grained marine and lacustrine clayey and sandy deposits. The coastal plain around Pisa is composed of a structural low, filled by alluvial deposits (Bossio et al., 1993; Bruni et al., 1994).

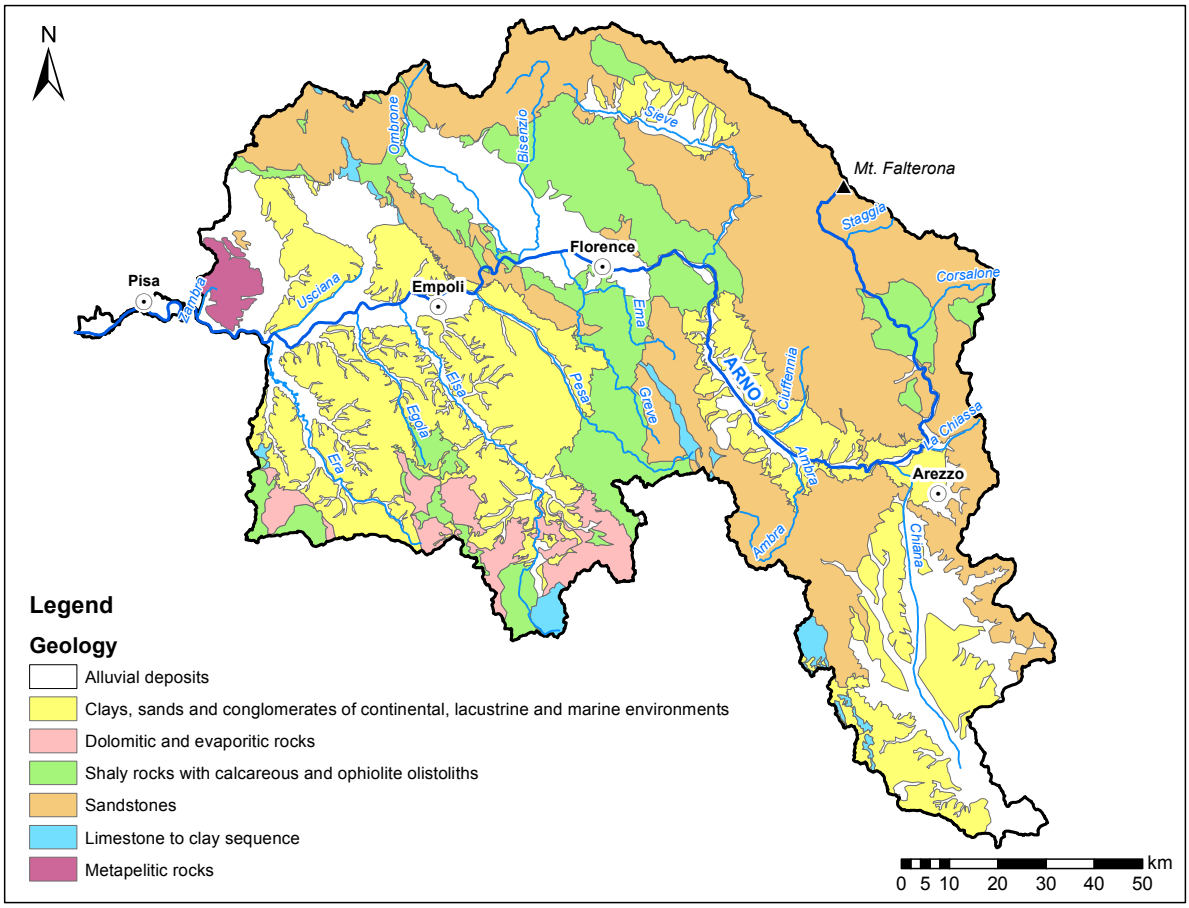

Figure 3 Schematic lithological map of the Arno river basin modified after Carmignani et al. (2013).

2.3.1 River Sediments

Bencini and Malesani (1993) explored the mineralogy and heavy metal content of both the suspended and bedload sediments of the Arno river and its tributaries. They found a general mineral composition of quartz (9 - 44%), feldspars (7 - 32%) and clay minerals (11 - 80%). The most common clay minerals in the basin are vermiculite, chlorite, illite and kaolinite. The metal content analysed (Cu, Pb, Zn, Ni, Cr, Mn) is mainly trapped within the minerals (92 - 99%), with clay minerals being the preferred host. Furthermore, metals were related to metal-organic complexes (0.6 - 8%) and to adsorbation on clay particles (0.1 - 0.4%).

2.3.2 Mining Activities

Two areas in the ARB are effected by mining activities, namely the Santa Barbara lignite district and different mineral deposits in ophiolites and serpentinites.

The Santa Barbara lignite mining district consits of three large deposits: Castelnuovo, Allori and San Donato Gaville. They are located on the left-side bank of the Arno river to the west of San Giovanni Valdarno (between Florence and Arezzo), hosted by the Meleto Clay Unit (Albianelli et al., 1997) in two distinctive lignite seams (Ielpi, 2011). The Meleto Clay Unit is composed of an up to 200m thick succession of muds with a high content of plant debris (Albianelli et al., 1997). Mining activities first started in the 19th century in the Castelnuovo deposit as an open-pit mine. Later on, the excavation operations were extended from open-pit to underground and to the deposits Allori and San Donato Gaville. Large scale open-pit mining took place in the years 1955-1994.

The ophiolitic blocks sometimes contain Copper (Dessau, 1974). Accordingly, several enrichments were found in the southern part of the catchment. Though, there are no active copper mines today.

2.4 Anthropogenic Influences

Anthropogenic contaminations in the ARB include organic substances, phosphates and coliform bacteria, detergents and potentially harmful metals (Bencini and Malesani, 1993; Cortecci et al., 2002; Dinelli et al., 2005; Nisi et al., 2005) (Fig. 4). The ARB counts roughly $2.6 \cdot 10^6$ inhabitants, one third live in the major towns. Though, the contamination load is estimated to be equivalent to $8.5 \cdot 10^6$ inhabitants, which corresponds to 1,033 polluters per km^2. Due to the high contamination load, the entire basin has to be considered as contaminated (no section is completeley uncontaminated).

According to Consorzio Pisa Ricerche (1998), major anthropogenic inputs in the Arno river downstream of Florence include:

- direct discharge of domestic black and white waters from the city of Florence. This pollution is estimated to a contamination load equivalent of 10^6 inhabitants.

- waste waters, feeding the Bisenzio and Ombrone rivers from industrial settlements and flower and plant nurseries around Pistoia and Prato. Waste waters from the textile industry around Prato (approximately 80 % of which are treated) correspond to a contamination load equivalent of $1.4 \cdot 10^6$ inhabitants. The Bisenzio river holds further domestic waste waters from the Vaiano municipality and the northern part of Florence through the Macinante Canal. Domestic water input from the Ombrone river is treated.

- discharges from many tanneries in the leather district (95 % treated) into the Usciana river, corresponding to contamination equivalent load of $3.2 \cdot 10^6$ inhabitants. Additionally, paper-mills release their treated waste waters into this tributary.

Upstream of Florence, the main source of contamination is traced back to the Chiana valley, where waste waters from electrochemical plants processing Au in the Arezzo district are released into the drainage system. Dall'Aglio (1971) describes an Hg anomaly in the stream sediments caused by these industries. Furthermore, untreated effluents from intensive agricultural-zootechnic activities put further anthropogenic pressure onto the river.

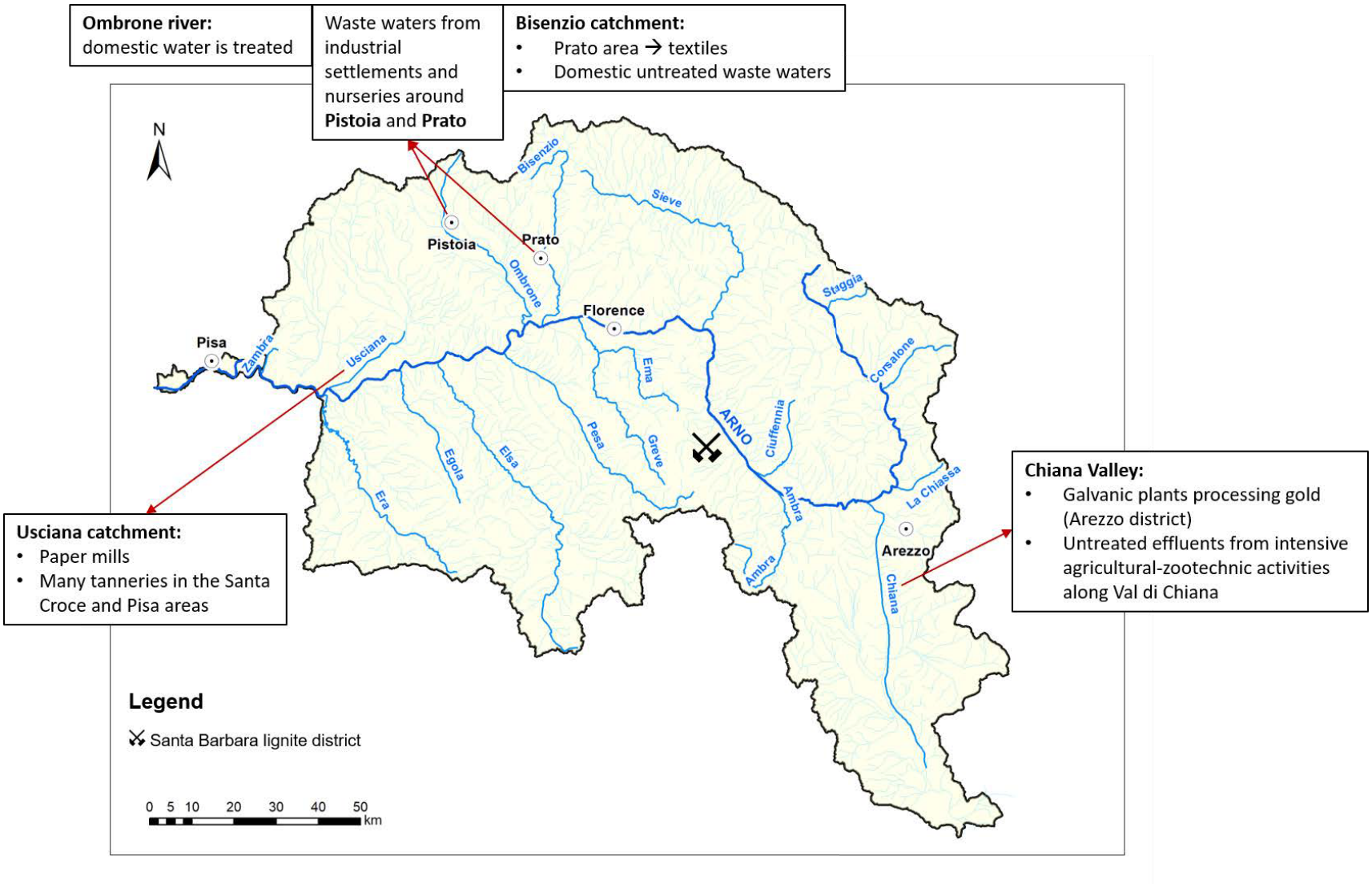

Figure 4 Summarized anthropogenic pressures on the ARB (Consorzio Pisa Ricerche, 1998).

Chapter Three

Materials and Methods

3.1 Field Sampling Methods

Within this research, a combined sampling campaign was carried out to collect river waters (not described in this study) and stream sediments of the Arno river catchment. Sampling took place on August 26 - 27, 2019.

The sampling spots of the Arno river basin were chosen based on the locations of previous water analysis of Nisi et al. (2008). The placement of sampling points starts close to the Arno spring (Monte Falterona) in the north-easternmost part of the catchment and ends at the river mouth into the Tyrrhenian sea close to Pisa in the most western part of the basin. To evaluate the input of the drainage system, the main tributaries were sampled as well.

In total, 33 river water and stream sediment samples were taken (Fig. 5). 17 were collected from the main tributaries close to the confluence with the Arno river, including one sample located far offside the main course. This is due to a special lithological environment within the catchment of this tributary. The other 16 sampling points were set at locations along the main course. To guarantee a maximum of comparability, both river waters and stream sediments were taken at the same location.

Samples of the Arno river were labeled 'ARN' with a roman number attached, ordered from source to mouth (e.g. ARNI for the sample closest to the source, see Fig. 5 and Appendix

A). To identify the main tributaries, they were labeled with the first two letters of the river name, followed by a cardinal number and ordered by their distance to the Arno river source (e.g. CH3).

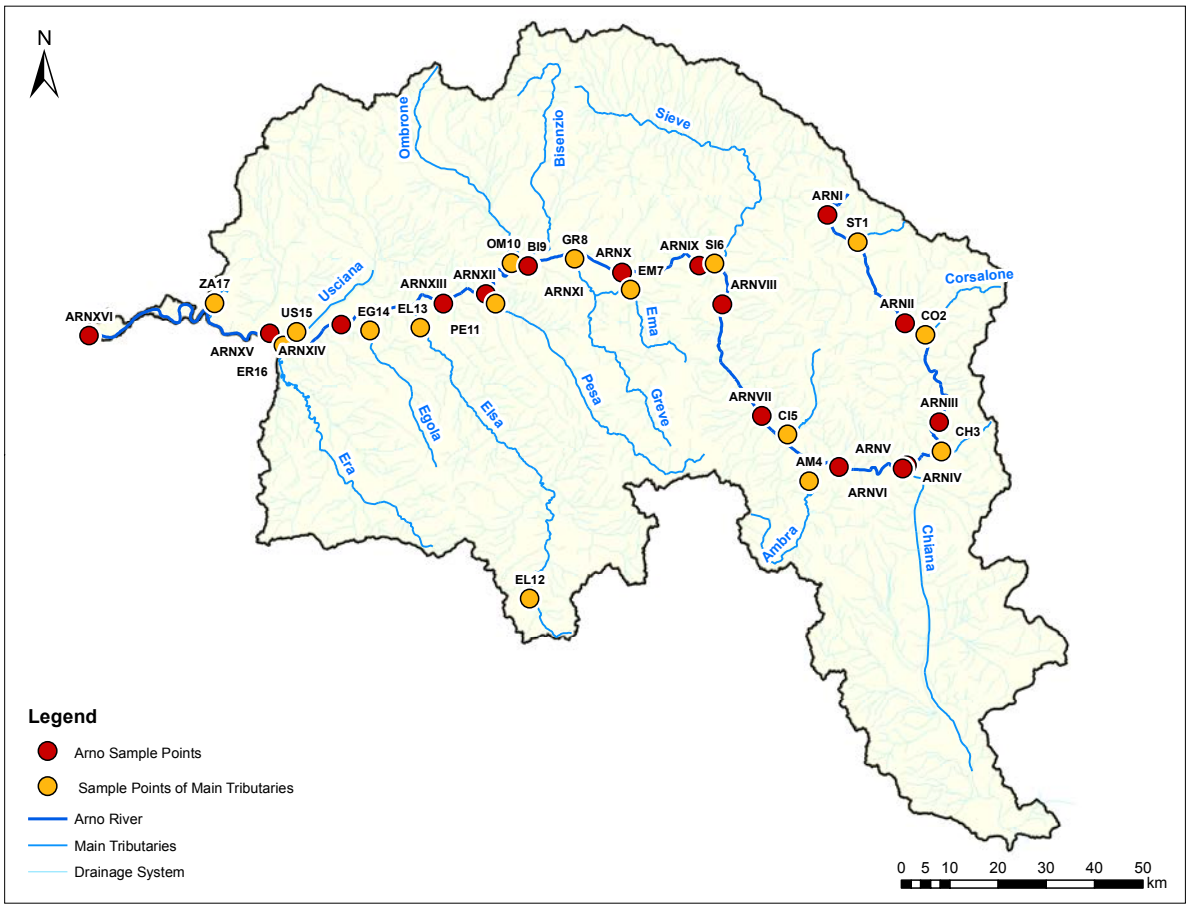

Figure 5 Sample locations within the Arno catchment area.

3.1.1 Stream Sediments

To obtain a stream sediment sample, about 1kg of the fine grained fraction of the stream sediment was taken from the river bank within shallow water areas with (almost) no river current, or otherwise as close to the water body as possible. To acquire a representative sample, the stream sediment was collected from several spots along the river bank using a stainless steel hollow-core sampler (Auger, Fig. 6) or a plastic shovel (Fig. 7). The collected

samples were then stored in plastic bags.

Figure 6 Collection of stream sediments in shallow water areas using a stainless steel hollow-core sampler here illustrated at sample sites (a) ARNXIII and (b) ARNXV. (c) Stainless steel hollow-core sampler.

Figure 7 (a) Plastic shovel used for the sampling campaign. Examples of sampling with the plastic shovel at sample sites (b) PE11, (c) ARNVIII, (d) US15, (e) ARNXII and (f) CI5.

3.2 Analytical Methods

3.2.1 Sample Preparation

The wet samples were put into glass bowls and dried at 70°C in a drying cabinet until constant mass was reached. Using a mortar, the dry sediments were then loosened before sieving them at a mesh width of 0.18mm. To obtain a homogenized powder sample, the fraction <0.18mm was milled with a mortar grinder (Retsch RM 100) for at least 15min.

3.2.2 Chemical Analysis of Stream Sediments

5 - 6g powder of each sample was put into ceramic crucibles, dried overnight at 105°C in a drying cabinet and left to cool down to room temperature in a desiccator.
Before creating glass beads, the loss of ignition (LOI) was determined by executing following steps:

- Weigh an empty ceramic crucible
- Fill 4 - 5g of powder sample (from the desiccator) into the crucible and weigh them together
- Burn crucible with powder sample in a muffle oven at 1,050°C for two hours
- Let hot crucibles cool down in desiccator
- Weighing of burned crucible plus sample

The LOI (in weight percent) was calculated from the weight differences of the different masses.
The XRF analysis was performed with fused beads. The burned sample was homogenized, dried at 105°C for 1 hour and left to cool down to room temperature in a desiccator. For the production of one fused bead, 1g of sample and 8g of a fluxing agent (Di-Lithiumtetraborat)

were mixed in a platinum crucible. The mixture was molten in an Eagon melting oven at 1,050°C, poured into a platinum crucible and left to cool down afterwards.
The beads were analyzed by X-ray fluorescence (XRF) analysis using a PANalytical Axios XRF Spectrometer, applying a calibration established with GeoPT-rock standards.

3.2.3 Magnetic Susceptibility

The magnetic susceptibility estimates the content of ferromagnetic particles in a sample (Scholger, 1998). In stream sediments, those particles derive from two different environments. One possible origin is their natural occurrence as Fe-oxides (magnetite, hematite). The second source is anthropogenic pollution, such as residues from steel industry or fly ash (Hanesch et al., 2007). Although the measurement of magnetic susceptibility cannot distinguish the source of particle input, it offers a quick indication where metallic anomalies are located.
Analogous to the chemical analysis, powder samples were used. This configuration enables a correlation of the results of both analyses. 10g of powder sample were weighed and transferred into plastic cylinders of $10cm^3$. The mass specific magnetic susceptibility of all stream sediment samples was measured three times and the resulting mean was calculated for each sample individually, expressed in the unit $10^{-8}m^3/kg$. The measurements were carried out in the Paleomagnetic Laboratory of the Institute for Geophysics (Montanuniversität Leoben) in Gams, Austria, using a AGICO MFK1 with a field intensity of 200A/m and a frequency of 976Hz (Fig. 8).
The shape of magnetic particles provides a useful tool to gather information on their origin, since particles from anthropogenic sources show perfectly spherical surfaces, while naturally occurring ones are rather irregular. Hence, further investigations on an optical microscope verify their origin.

Figure 8 (a) Powder Samples in plastic cylinders; (b) and (c) setup for measuring the magnetic susceptibility with an AGICO MFK1.

3.3 Statistical Methods

3.3.1 Compositional Data Analysis

Compositional data are defined as parts of some given numerical total, which only carry realtive information between them (Aitchison, 1986). The data sums up to a constant and the only relevant information is contained in the ratios between its components. Data, which sum up to a known total, usually 1, 100% or 10^6 ppm are called closed data. Considering this fact, the data only have positive values and they are not free to vary independently. As a result they do not vary from -∞ to +∞. Since this definition describes geochemical data, they can be considered and treated as compositional data. The closure of the data causes many problems for correlation and multivariate statistical analyses. Compositional data do not follow the usual Euclidean geometry, but they rather follow the simplex (often called the Aitchison geometry, e.g. Pawlowsky-Glahn and Egozcue, 2001). In order to avoid misleading results, it is needed to open up the compositional closed data. Aitchison (1986) suggests to transform them by the centered log-ratio (clr) transformation or additive log-ratio (alr) transformations to open the dataset. Egozcue et al. (2003) introduced the isometric log-ratio (ilr) transformation. These transformations allow the application of classical statistical

analysis.

The clr transformation as defined in Equation 3.1

$$\text{clr(x)} = \left(\ln\frac{x_i}{g(x)}\right)_{i=1,...,D} \qquad \text{with} \qquad g(x) = \sqrt[D]{x_1 \cdot x_2 \cdot ... \cdot x_D} \tag{3.1}$$

is obtained by dividing each component x_i by the geometric mean g(x) of all considered parts (in this case chemical elements).

In this study, clr transformed data were used to describe the data variability (clr variance). The isometric log-ratio (ilr) transformation expresses the clr images in an orthonormal basis on the hyperplane y1 + ... + yD = 0 and is defined by Egozcue et al. (2003) by following equation (for composition x):

$$z = \text{ilr(x)} = (z_1, ..., z_{D-1})^T, \qquad z_i = \sqrt{\frac{i}{i+1}}\ln\frac{\sqrt[i]{\Pi_{j=1}^{i} x_j}}{x_{i+1}} \qquad \text{for} \qquad i = 1, ..., D-1 \tag{3.2}$$

The ilr-transformation was used for calculating the robust Mahalanobis distances and performing the robust factor analysis.

3.3.2 Correlation Analysis

Due to the relative nature of compositional data, a correlation analysis carried out on original compositional data does not provide interpretable results for a fixed constant sum constraint. This is especially induced by the scale invariance, which causes a negative bias of the correlation structure. Accordingly, Kynclová et al. (2017) suggests to perform a correlation analysis on compositional data using orthonormal logratio coordinates. The strength of association between compositional parts is measured in this method. For this purpose, the correlation coefficient between a particular choice of orthonormal coordinates is utilized with respect to the Aitchison geometry. A correlation coefficient is referred as a summarizing information of variable relations illustrated in a scatter plot. The logratios, on which the orthonormal

coordinates are based, are always formed by a part of interest and the residual variables, aggregated according to a weighted geometric mean. Since the resulting coordinates are logratios of individual parts to a weighted 'average representative', they show the influence of those parts on the composition on an average. This method is based on Filzmoser et al. (2009a), which describes all relative information about the parts of interest with logratio coordinates.

In this study, a correlation analysis for compositional data based on the non-parametric Spearman correlation coefficient was performed in R using the packages robCompositions (Templ et al., 2011) and gplots (Warnes et al., 2020) for the stream sediment data according to the method of Kynclová et al. (2017) (used script is in Appendix C).

3.3.3 Robust Factor Analysis

A factor analysis (FA) is used to summarize multivariate information into a more compact shape. It extracts certain directions in the data space, the so called factors. Therefore, the FA aims to reduce the given dimensions to a number of representative factors (Reimann et al., 2002). Those factors are not directly measureable, though they represent certain features inherent in the data (e.g., Basilevsky, 1994; Johnson and Wichern, 2007). This analysis is applied to explore a certain amount of new variables (factors) that are not linked evidently and thus offers an enhanced perception on the data.

It is essential to apply a suitable data transformation when performing a factor analysis on compositional data. In this study, a robust factor analysis (RFA) according to Filzmoser et al. (2009b) was executed, where data are clr transformed. In order to run a robust covariance estimation, further transformation is needed. Thus, the robust covariance estimation is performed in the ilr space and subsequently transformed back to the clr space for interpretation.

The results of the RFA are visualized in a loading plot, where high values represent a high

influence of the corresponding clr variable on the factor. The pattern of the highly influential variables helps for the interpretation of the factor. In this study, RFA was performed in R using the packages robustbase (Maechler et al., 2019), StatDA (Reimann et al., 2008) and MASS (Ripley et al., 2019) to discover the underlying processes that control the data variability, aiming to differentiate processes. For this analysis, twice as many measured points than variables are needed. Due to that, a selection of 16 elements was necessary. The data was selected following way: all major elements and the six trace elements with the highest clr-variability. All selected variables have less than 15 % of values below the lower detection limit (LDL).

3.3.4 Robust Mahalanobis Distances

Mahalanobis distances (MD) measures distances between objects. They identify multivariate outliers, thus revealing data points showing atypical phenomena (e.g. Filzmoser et al., 2012). MD are based on the estimation of the covariance structure, which is used to assign a distance to each observation from the center of the multivariate data cloud. Robust estimates for the center μ_R and the covariance matrix $\sum_R$ are essential to obtain reliable distance measures (Rousseeuw and van Zomeren, 1990; Maronna et al., 2006). Rousseeuw and van Zomeren (1990) define the robust Mahalanobis distance (RMD) for observations $x_1, ..., x_n$ in the p-dimenstional space with center μ_R and covariance $\sum_R$, as

$$RMD_i = \sqrt{(x_i - \mu_R) \sum_R^{-1} (x_i - \mu_R)^T} \qquad \text{for} \qquad i = 1, ..., n \tag{3.3}$$

In this study, Mahalanobis distances were calculated to discover compositional changes of the stream sediment chemistry within the ARB. The R package robustbase (Maechler et al., 2019) was used for this purpose and the Minimum Covariance Determinant (MCD) was employed as the robust estimator (Filzmoser and Hron, 2008; Filzmoser et al., 2012). Since the given data is compositional, an ilr-tranformation was performed before via the

function pivotCoord in the R package robCompositions (Templ et al., 2011).

Before calculating RMD, the data set was ordered from source to mouth and divided into two sets. Firstly the main elements and secondly the ten trace elements showing the highest clr-variance. Due to statistical reasons, the compositional center was computed for both data sets by the first 18 samples from the source.

Chapter Four

Results

4.1 Geochemical Pattern

The original data set obtained by XRF analysis are presented in Appendix A. The statistical summary of the major elements as shown in Table 1, shows values above the detection limits for all major elements. The data are given for the bulk sample, respecting the loss of ignition (LOI) and the oxides are corrected to their elementary form.

The highest median is represented by Si (29% wt), followed by Al (6% wt) and Ca (4% wt). The rest of the major elements illustrates medians below 3% wt. In general, the mean and median of the major elements are located quite close to each other. The highest difference between those two values is observed for Ca (1.3% wt) and Si (0.9% wt); all other major elements show a difference of max. 0.1% wt. This indicates, that Ca and Si are the elements with the largest asymmetry.

Table 1 Statistical summary (minimum and maximum values, median, mean, 1st and 3rd quartile) of major elements in the Arno river basin sediments in weight %.

Element	Min.	Max.	Median	Mean	1st Qu.	3rd Qu.
Si	19.70	34.24	29.33	28.48	25.80	31.96
Ti	0.23	0.38	0.30	0.30	0.29	0.33
Al	4.21	6.57	5.92	5.83	5.64	6.13
Fe	1.80	3.49	2.52	2.63	2.39	2.89
Mn	0.04	0.24	0.06	0.07	0.05	0.08
Mg	0.77	1.89	1.07	1.13	0.96	1.26
Ca	1.05	13.83	4.24	5.52	2.31	7.20
Na	0.07	1.40	1.01	0.91	0.72	1.11
K	0.71	1.96	1.61	1.55	1.44	1.71
P	0.04	0.15	0.06	0.07	0.05	0.08

For trace elements, Ba represents the highest median with 420mg/kg, followed by Sr (197mg/kg) and Zr (195mg/kg) (Table 2). The majority of the data comprises medians below 100mg/kg.

The biggest deviation between the median and mean is observed for Sr (42mg/kg) and Cr (32mg/kg). For the rest of the data, those deviations are rather small.

Table 2 Percentage of samples with values below the detection limit (LDL), number of samples with values above the LDL and statistical summary (minimum and maximum values, median, mean, 1st and 3rd quartile) of trace elements in the Arno river basin sediments in mg/kg.

Element	<LDL	Num	Min.	Max.	Median	Mean	1st Qu.	3rd Qu.
Cu	0.00	33	12	110	34	42	21	60
Ce	0.39	20	35	118	61	64	38	88
Nb	0.00	33	6	15	11	11	10	12
Zr	0.00	33	97	289	195	195	176	215
Y	0.00	33	14	40	22	22	20	23
Sr	0.00	33	54	629	197	239	152	275
Rb	0.00	33	29	103	82	80	77	87
Th	0.06	31	4	14	9	9	7	11
Pb	0.03	32	4	120	26	33	22	37
Ga	0.03	32	1	18	15	14	14	16
Zn	0.00	33	52	223	88	100	69	119
Ni	0.00	33	33	150	50	57	45	61
Co	0.12	29	5	25	11	12	10	14
V	0.00	33	46	87	63	63	59	67
La	1.00	0	-	-	-	-	-	-
Ba	0.00	33	127	649	420	402	365	433
Sc	0.00	33	5	16	12	11	9	14
Cr	0.00	33	65	546	114	146	98	151
Cs	1.00	0	-	-	-	-	-	-
Hf	0.64	12	4	13	5	6	5	8
Nd	0.24	25	14	44	26	26	22	32

To get an overview on the distribution of the data, logarithmic boxplots were created for both major (Fig. 9) and trace elements (Fig. 10).

As visualized in Fig. 9, Ca is the element with the greatest interquartile range compared to the other major elements. Al and Ti illustrate the smallest distributions. Most outliers (three) are found for Al and Na, with Na representing the highest range of data distribution. Cu comprises the greatest interquartile range for the trace elements (see Fig. 10), followed by Ce and Sr. Several outliers can be detected, with Pb showing the greatest range.

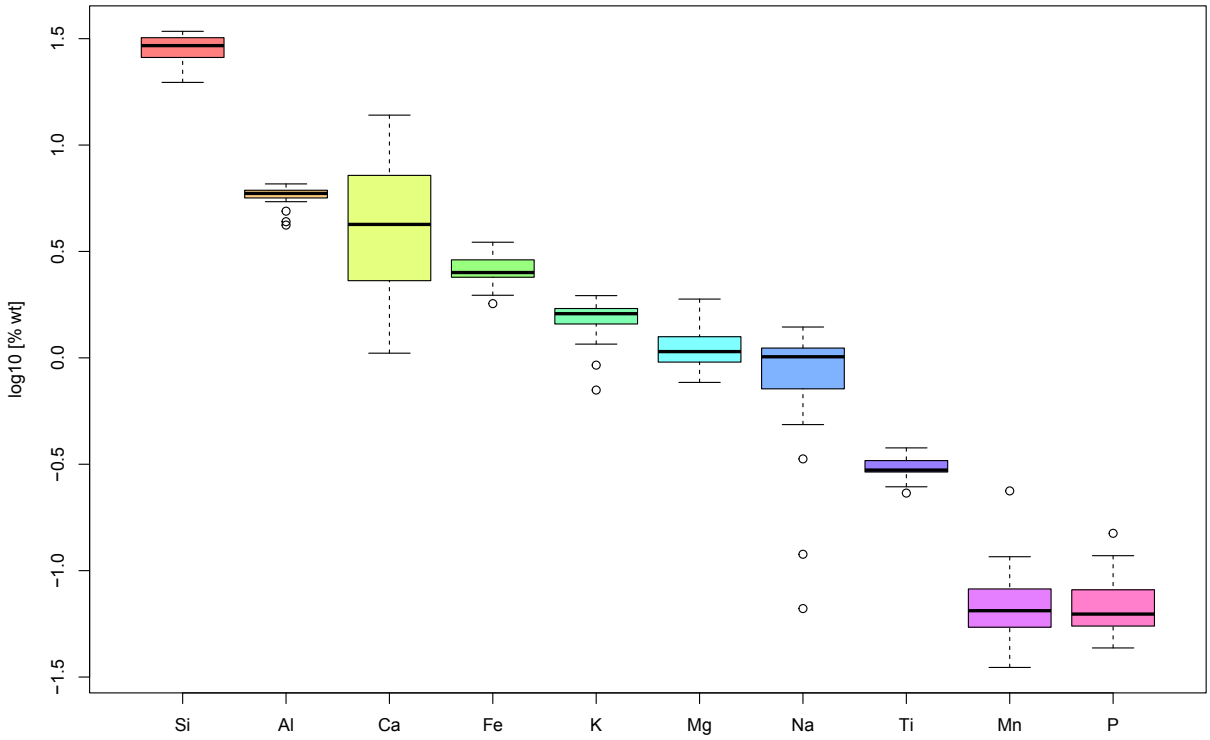

Figure 9 Logarithmic boxplot diagram of the major elements constructing the sediments of the Arno river basin, sorted from highest to lowest median. Each box includes the 25th and 75th percentiles with the median displayed as a line and outliers as circles. Concentrations are in log10 [% wt].

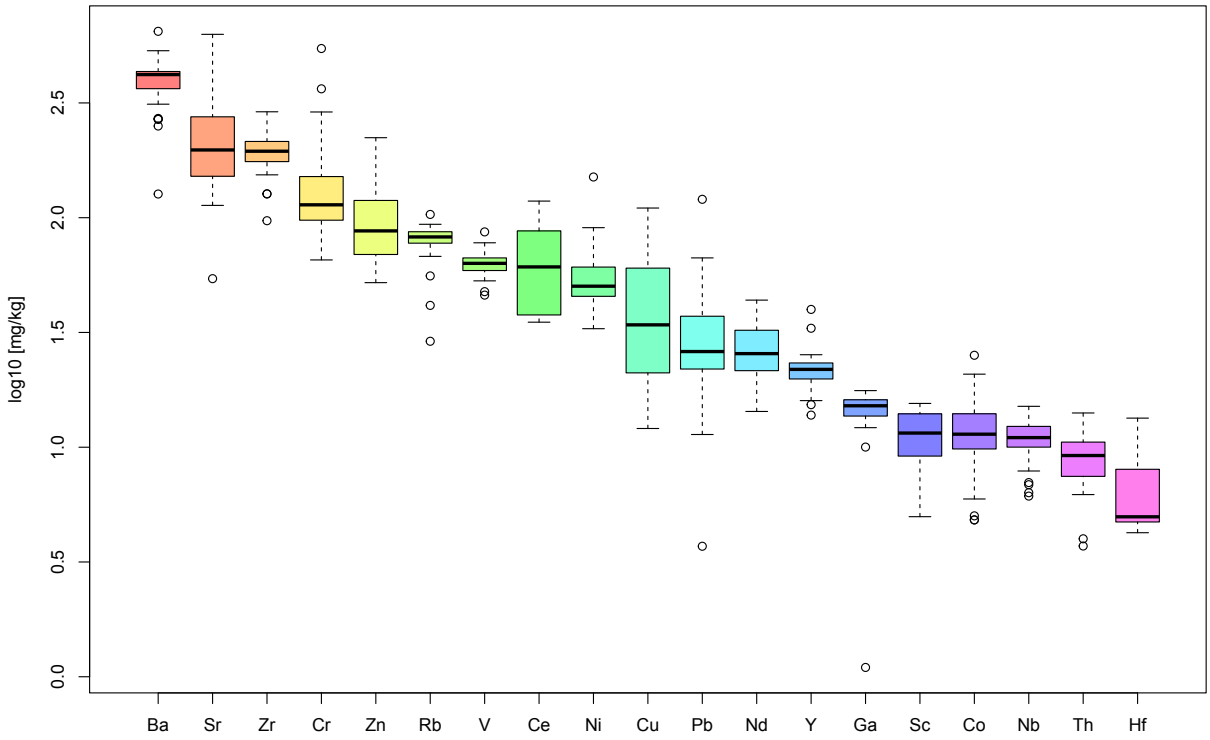

Figure 10 Logarithmic boxplot diagram of the trace elements constructing the sediments of the Arno river basin, sorted from highest to lowest median. Each box includes the 25th and 75th percentiles with the median displayed as a line and outliers as circles. Concentrations are in log10 [mg/kg].

Tukey boxplots were created for each element of the raw and clr-transformed data and the distributions obtained are correlated to a schematic lithological map. The resulting geochemical atlas is found in Appendix B. Elevated concentrations in Cu and P are observed around the Chiana valley and at sampling points AM4 and CI5. The elements Fe, Mg, Cr, Ni, Ti, Co and V are considerably higher at sample EL12 and around Florence. Increased concentrations of P and Pb are found in samples BI9 and OM10. Sample ZA17 is highlighted by Fe, Al, K, P and Ti and sample ARNXVI by Ca, Mg, Mn, Sr and V. There are some differences when comparing the distribution maps of the raw data to the clr-transformed data. The Tukey boxplots of the raw data show outliers for the elements Na and Rb at

sampling point ZA17. On the other hand, the clr-transformed data indicates also Ti, Al, Fe, P, Sr and Ni as outliers for this sample. Al outliers of the raw data at sampling spots EL12, EL13 and AM4 are part of the lower whisker in the Tukey boxplot for clr-transformed data. The Tukey boxplot for raw data identifies Mg and Ba from sample ARNI as an outlier, whereas they are not stated as such in the boxplot for clr-transformed data. This scheme is also observed for the element Ni, where samples ARNIV and GR8 are defined as outliers for the boxplot using raw data, but not for the clr-transformed data. Furthermore, for Sr, the samples ARNV and AM4, as well as for Cr the sample ER16 are all marked as outliers only by the Tukey boxplot based on raw data. For Fe, sample PE11 is identified as an outlier by the Tukey boxplot for clr-transformed data, not by the one for raw data. The same is observed for V, where samples EL12 and ARNXVI are outliers only for the clr-transformed data.

4.2 Compositional Data Analysis

To get an overview on the variation of specific elements, the clr variance was calculated. Therefore, the software CoDaPack (Comas-Cufí and Thió-Henestrosa, 2011) was used by producing a compositional summary related to logratios, which also includes the Variation Array and Total Variance (see Appendix A). Ca (13.75 %) and Na (11.03 %) show the highest variability. Furthermore, Cu (9.22 %) and Pb (9.40 %) are important factors of variability. All other clr variances are relatively homogeneous and are below 9 %.

The results of the correlation analysis for compositional data according to the method of Kynclová et al. (2017) are visualised in a heatmap, which rearranges the chemical variables according to their similarity using a hierarchical cluster analysis (Fig. 11).

The heatmap shows associations between elements. There are two major groups of positive correlation - Ca and Sr, and Ce and Nd. Furthermore, a bigger cluster can be observed in the upper right corner, including majorly Rb and K, but also Nb, Ga, Al, Sc, Si and Na. Sr

and Ca against Sc on the other hand indicate a negative correlation in the dataset.

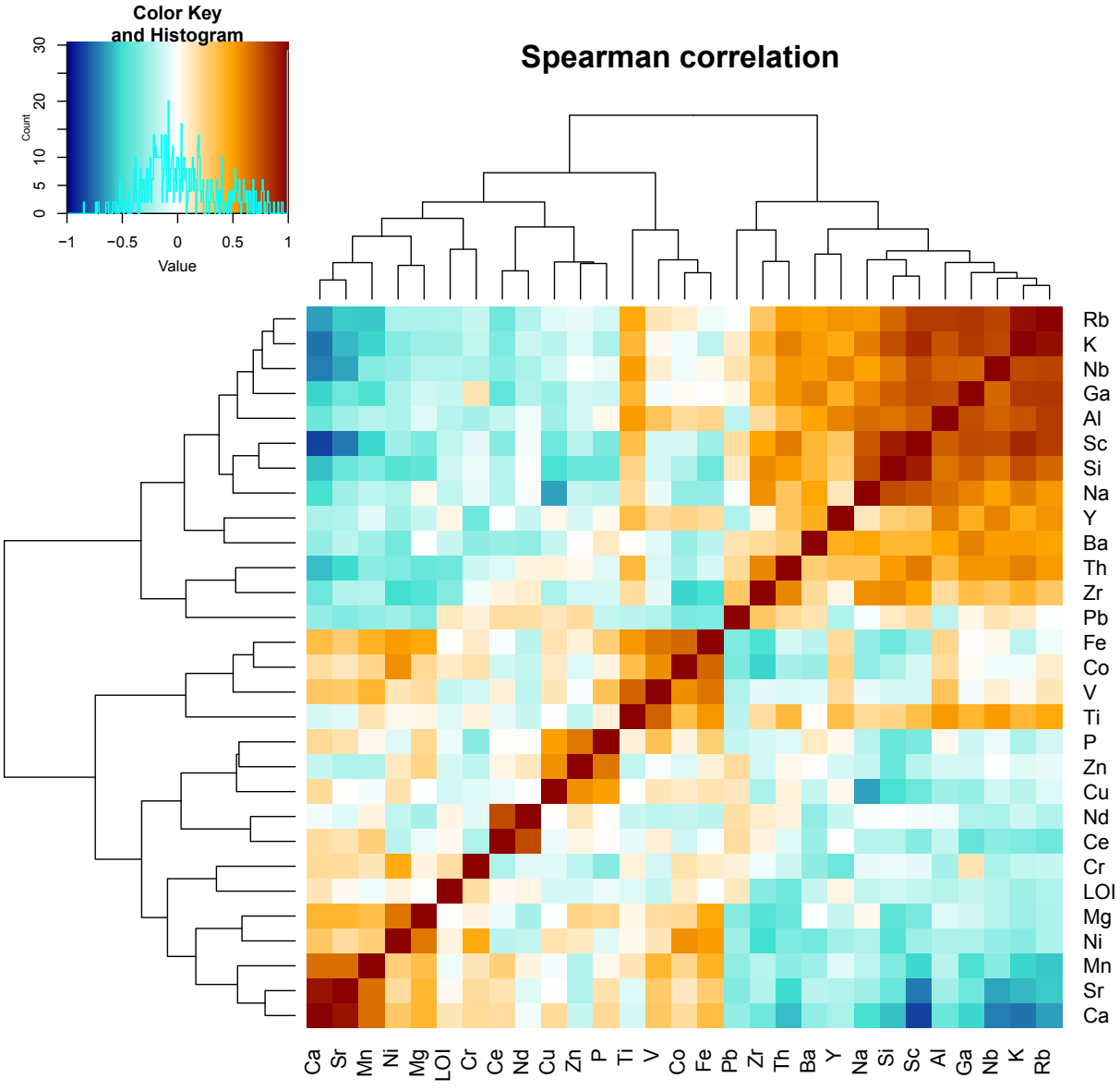

Figure 11 Heatmap of the stream sediments for the Arno river basin. Red indicates a positive correlation, while blue stands for a negative correlation. The darker the colour, the stronger is the correlation.

To discover the underlying processes that control the data distribution, a robust factor analysis according to Filzmoser et al. (2009b) was performed in R (used script in Appendix C). In this analysis, 4 factors explain 83 % of the total variability (Fig. 12).

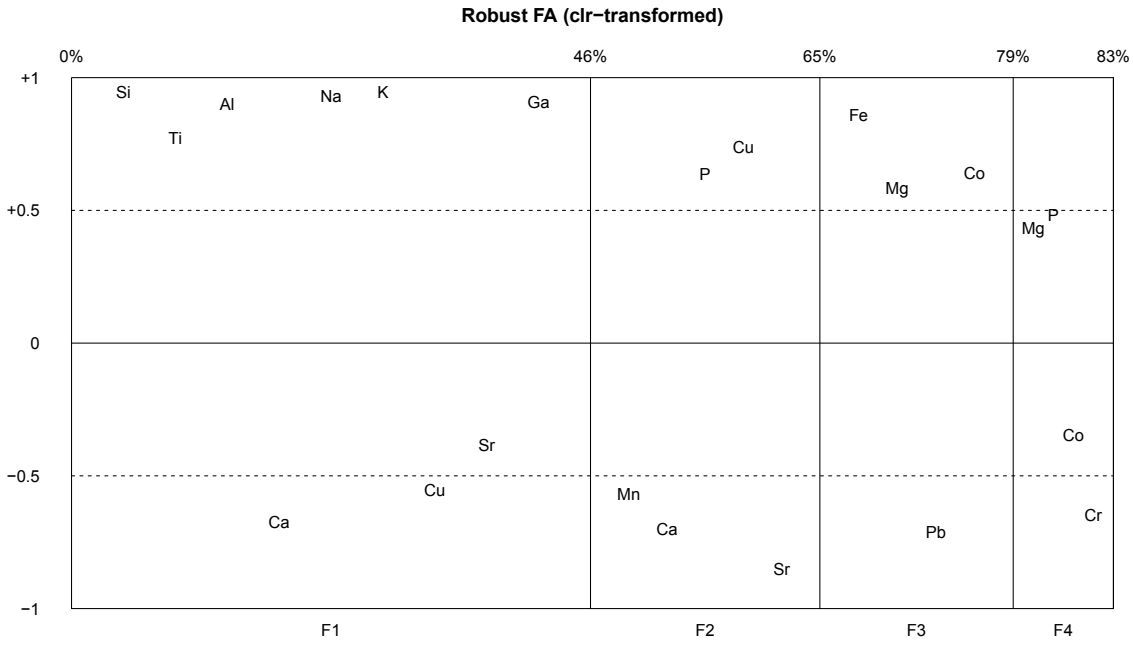

Figure 12 Factor loading plot for robust factor analysis based on clr-transformed data of the Arno river basin sediments. Elements with loadings between -0.3 and +0.3 are not plotted.

The first factor (F1) explains almost half of the data variability, whereas Factor 2 and 3 comprise 19 and 14%. F4 describes only 4% of the total variability and therefore is considered as noise.

Factor 1 reflects the major underlying lithologies. It is dominated by elements associated with siliciclastic rocks (e.g. Si, Al, Na, Ka). The carbonatic influence (Ca, Sr) and Cu characterize the negative loadings. Factor 2 appears to reflect the antropogenic input in its positive loadings (P, Cu) and the influence of carbonatic rocks (Mn, Ca, Sr) in its negative loadings. Fe, Mg and Co indicate the ophiolitic input into the basin, which is represented in Factor 3 and 4.

The regional distribution maps for scores of factors 1, 2 and 3 for the centered log transformed data are correlated to a schematic geological map of the basin.

The map of Factor 1 (Fig. 13a) illustrates a clear correlation between positive scores

and the presence of siliciclastic rocks. According to Carmignani et al. (2013), they are sandstones from the Tuscan domain and clays, sands and conglomerates from Pliocene-Pleistocene marine deposits. Negative scores overlap with carbonatic rocks, classified by Carmignani et al. (2013) as Tuscan domain and evaporitic and post-Messinian lacustrine and lagoonal deposits. Positive scores of Factor 2 (Fig. 13b) do not appear to be linked with geologic processes, whereas negative scores coincide very well with carbonatic rocks occurring within the southern part of the basin. Positive scores of factor 3 (Fig. 13c) reflect the metallic input into the river system, which can partly be correlated with underlying lithologic processes.

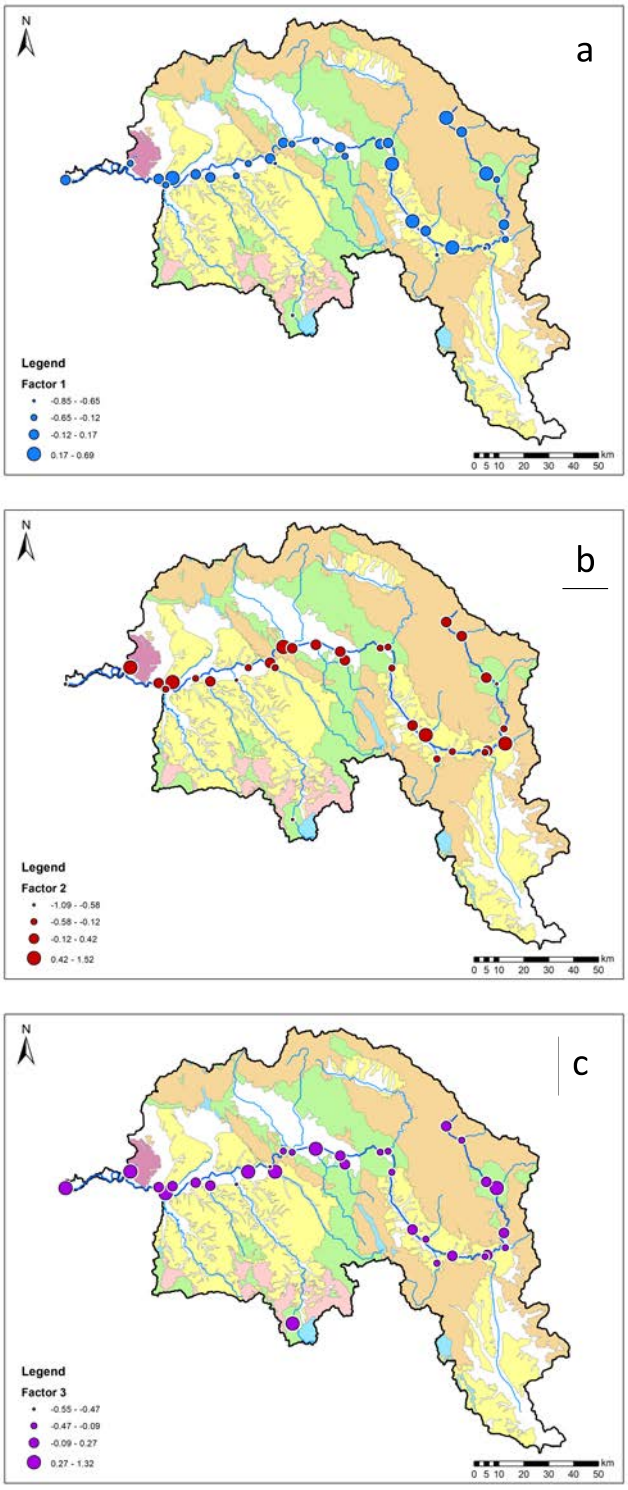

Figure 13 Scores of Factor 1 (a), 2 (b) and 3 (c) illustrated on a schematic lithological map modified after Carmignani et al. (2013). Legend for lithologies in Fig. 3.

Robust Mahalanobis Distances were calculated based on section 3.3.4 in R (used script is in Appendix C), following Gozzi et al. (2019). The results are visualized as a plot (Fig. 14) and on a schematic geological map (Fig. 15). High RMD values are deduced from samples with a bigger distance to the compositional center and therefore denoting a greater compositional change. The cut-off value is defined as the 97.5% quartile and is illustrated as a red line. Values above that line are considered as multivariate outliers (Rousseeuw and van Zomeren, 1990; Maronna et al., 2006).

In the RMD plot for major elements (Fig. 14a), Group 1 implies that the first 19 samples show mostly RMD values below the cut-off grade of 5. Consequently, points 6 (CH3) and 15 (ARNIX) are compositional outliers with RMD values of 32 and 19. For Group 2, persistent changes are visible. Even though there is a higher input of different compositions arising from side tributaries within this group, RMD values of the Arno river samples increase only on a smaller level. The RMD peak is represented by point 25 (EL12) with a value of 59.

Overall, the RMD plot for trace elements (Fig. 14b) looks similar to the plot for major elements. Though, compositional changes generally occur on a smaller extent. Similar to the other plot, most samples from Group 1 are located underneath the cut-off grad of 5. However, point 4 (CO2), 8 (ARNV) and 10 (AM4) from the source form exceptions and sample AM4 represents the plot peak with a RMD value of 30. Group 2 shows a persistent change in composition. Unlike the RMD for major elements, there are no significant compositional changes between side tributaries and the main course, except point 25 (EL12), which acts as a compositional outlier.

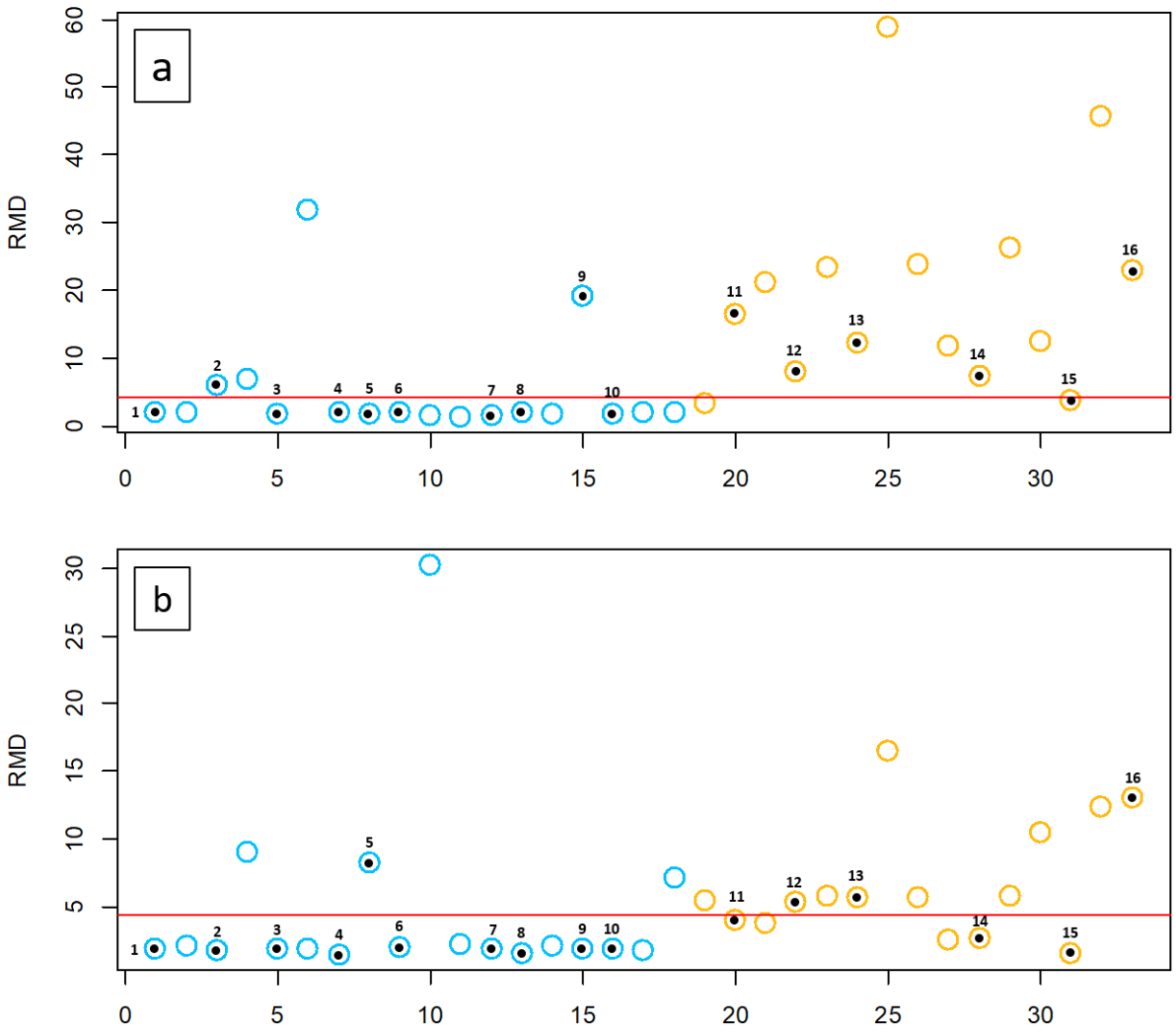

Figure 14 Robust Mahalanobis distances from the compositional center of the Arno stream sediments. Blue points indicate samples used to calculate the compositional center. The rest of the samples is in orange. Samples are ordered from source to mouth. Samples from the Arno are marked with numbers from 1 to 16. The red line shows the outlier cut-off grade. RMD for major elements (a) and for trace elements (b).

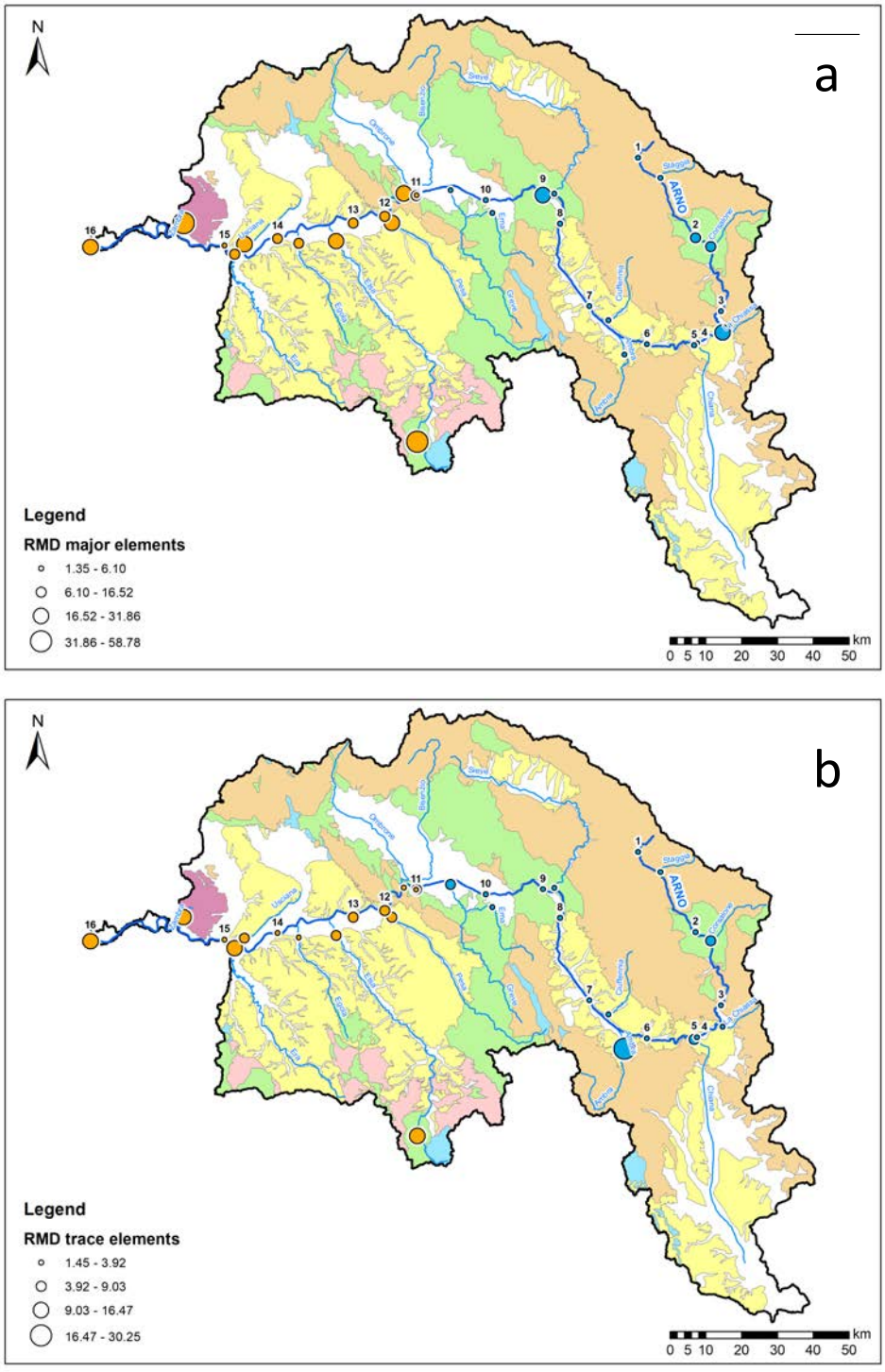

Figure 15 Schematic lithological map modified after Carmignani et al. (2013) with the robust Mahalanobis distances for major (a) and trace elements (b).The Arno sampling points are numbered source to mouth from 1 to 16. Legend for lithologies in Fig. 3.

4.3 Magnetic Susceptibility

The magnetic susceptibility of the Arno river catchment is rather homogeneous. The majority of values range from 12 to 80 * 10^{-8} m^3/kg, with the ARNVII sample illustrating the minimum of the basin. Two samples represent anomalies (see Fig. 16): ZA17 is the maximum of the dataset with a measured value of 162 * 10^{-8} m^3/kg. Compared to the rest of the data, EL12 also shows an elevated magnetic susceptibility (84 * 10^{-8} m^3/kg).

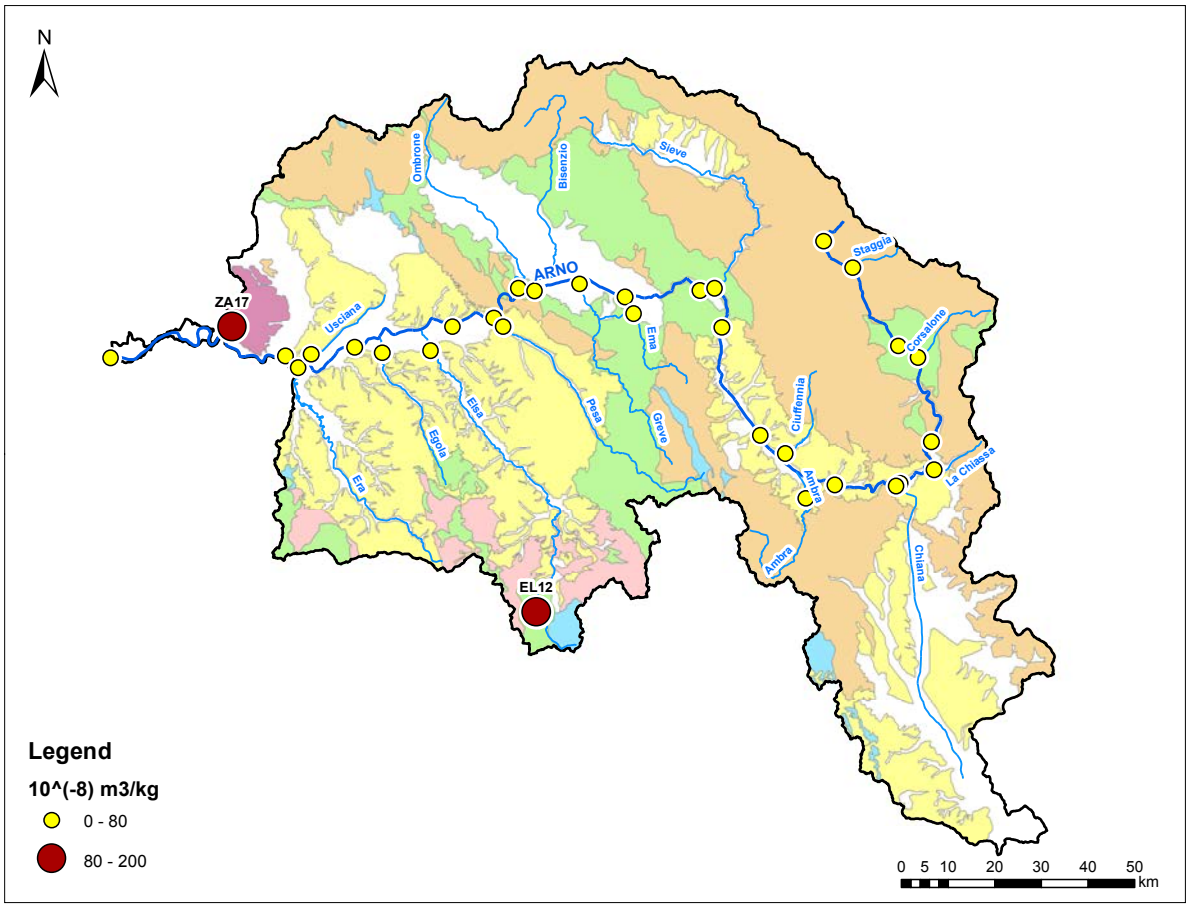

Figure 16 Schematic lithological map of the ARB modified after Carmignani et al. (2013) with the magnetic susceptibility in 10^{-8} [m^3/kg]. Legend for lithologies in Fig. 3.

Chapter Five

Discussion

5.1 Compositional changes throughout the Basin

The results of RMD on major elements (Fig. 14a) indicate deviating compositions for the lower basin. Here, the tributaries carry compositionally different sediments and therefore cause elevated RMD values. Though, the Arno samples below the confluence with those tributaries are not affected. There is a slightly increasing trend of compositional deviations along the lower course of the Arno river. As a result it is concluded, that the major element composition is rather resilient.

RMD on trace elements (Fig. 14b) show a very similar trend. Though, RMD values of trace elements are generally more stable, they fluctuate less. Major compositional changes occur at point 10 (sample AM4), 25 (EL12) and close to the river mouth.

5.2 Geochemical dissipation processes

The RFA based on the compositional data approach identifies 4 factors, which explain more than 80 % of data variability (Fig. 12). Those factors distinguish different processes controlling the data variability. All factors are linked to the lithological setting of the basin and pollutions. The majority of data variation is associated with siliciclastic, carbonatic and

ophiolitic rocks. However, according to Dinelli et al. (2005), P and Cu (positive loadings of Factor 2) as well as Pb (negative loadings of Factor 3) can be interpreted as 'pollution related', since they are commonly used in technological and agricultural activities (Cooper and Thornton, 1994).

The hierarchical cluster analysis according to the method of Kynclová et al. (2017) conforms the results of the RFA. The associations presented in the heatmap (Fig. 11) identify clusters with elements that commonly occur in siliciclastic rocks (positive correlation of Rb, K, Nb, Ga, Al, Sc, Si and Na), carbonatic rocks (positive correlation of Ca and Sr) and to a minor extent also ophiolitic rocks (Fe, Co, V and Ti). Those results coincide well with results of the RFA. Cr is not part of the ophiolitic cluster, which can be explained by the small amount of samples influenced by those rocks. Consequently it seems, that RFA is more suitable to pick up smaller influences as well.

To explain the anomalies found by performing RMD on major and trace elements, a comparison to the factors resulting from RFA is a promising strategy.

Sample CH3 (Fig. 17a) is controlled by carbonatic input as well as P, Cu and Pb, whereas the latter three elements can be interpreted as anthropogenic contamination. The sources of Copper in this specific area can be ascribed to agricultural activities and the sources of Phosphorous to domestic effluents and fertilizers.

Sample AM4 represents the peak RMD for trace elements. RFA analysis states negative scores for factor 1 and 2, indicating a significant carbonatic input in the catchment area of the sampling spot (Fig. 18a). This influence is characterized by Ca. Even though not illustrated in the schematic geological map (Fig. 18a), there are local carbonate outcrops in the catchment of the Ambra river (Carmignani et al., 2013), explaining the compositional change. Furthermore, slightly negative scores of factor 3 of the RFA (Pb) suggest an anthropogenic impact on the Ambra catchment, not confirmed by the raw XRF data. Here, no indication for elevated Pb concentrations is present. On the other hand, the raw XRF

data illustrates increased P and Cu concentrations, which may be attributed to agricultural use in the area, but was not recorded in the RFA.

Even though sample ARNIX indicates a significant compositional change for major elements, scores of the RFA are not informative (see Fig. 17b). The sampling area is influenced by its underlying geology. It is discharging from shaly rocks with calcareous and ophiolite olistoliths. Furthermore, Ti and Cr show elevated concentrations, which fits to the geological setting in this very area. The diffuse results of RFA analysis are probably due to the homogenizing effect of the main course.

RMD on sample OM10 defines another significant compositional change for major elements within the ARB. This is correlated to a conspicuous score of factor 2 at this location, indicating a strong influence of the elements P and Cu (Fig. 17c). They are derived from anthropogenic sources, waste waters from industrial settlements and horticultural activities around Pistoia in particular. Interestingly, the Bisenzio river is exposed to similar anthropogenic pressure around the town of Prato, but does not cause any RMD anomalies. This may be explained by the geological setting. While Bisenzio mainly flows through alluvial deposits, the Ombrone river is more influenced by shaly rocks with calcareous and ophiolite olistoliths (especially near the sampling location) and is therefore compositionally more different.

Sample PE11 shows high RMD values for major elements. The present compositional change originates from calcareous, as well as ophiolitic input. This is deduced both from the RFA (negative scores of factor 1 and positive scores of factor 3) and the prevalent geological setting (Fig. 17d). Those results coincide well with the original data, where concentrations of Ca, Mn and Sr (carbonatic input) and Fe, Ti, Co and V (reflect ultramafic fraction of the sediment) are particularly high. Additionally, the Al concentration is elevated, indicating clay mineral input from Pliocene-Quaternary fine-grained marine and lacustrine clayey and sandy deposits, on which the sampling spot is located.

Sample EL12 represents a major anomaly within the basin. The sample spot is located far off

the main course on ultramafic rocks and is surrounded by Triassic limestones, dolostone and anhydric and Messinian evaporitic formations (Dinelli et al., 1999b). Accordingly, anomalies in RMD for both major and trace elements can be expected. RFA analysis predicts a carbonatic (negative scores of factor 1 and 2) and ultramafic influence (positive scores of factor 3). It seems that the sample is equally composed of those factors (Fig. 17e and Fig. 18b). Thus, all anomalies are of geogenic origin.

Sample EL13 shows significantly higher RMD values for major elements. According to the RFA results, this sampling spot is mainly influenced by carbonatic sources (negative scores of factor 2). Even though there are ophiolitic rocks in the catchment area of this sample, there are no signs of ultramafic influences at sampling point EL13, neither in the RFA, nor in the raw data (Fig. 17f). As a result it is concluded, that ultramafic rocks are not transported into the main course (e.g. due to a higher physical/chemical resilience of ultramafic minerals and lower solubility in water). However, Pb seems to be an important factor (negative loadings of factor 3), suggesting a stronger anthropogenic influence due to industrial settlements in the area.

RMD on major elements display a considerable compositional difference for sample US15, which is dominated by silicates (positive scores of factor 1) as well as P and Cu (positive scores of factor 2) (Fig. 17g). This sampling point is underlain by clays, sands and conglomerates of continental, lacustrine and marine environments, which explains the silicatic influence. P and Cu may originate from anthropogenic sources, tanneries and paper-mills specifically.

The results of RMD for trace elements state a significant compositional difference for sample ER16. Scores of RFA specify those changes to a carbonatic (negative scores of factor 2) and ophiolitic influence (positive scores of factor 3). The scores are smaller compared to those of sample EL12, which was exctracted at a location directly underlain by ophiolites. This observation proposes a greater distance of the ophiolites to the sampling spot, which is supported also by the lithological map (Fig. 18c).

ZA17 shows elevated RMD for both major and trace elements. According to RFA, the sample is greatly influenced by positive scores of factor 2 (P and Cu) and moderately influenced by carbonates (negative scores of factor 1) and Fe, Mg and Cr (positive scores of factor 3) (Fig. 17h and Fig 18d). When comparing those results with the raw data, it seems that RFA might lead to a misjudgement, since no elements that are usually represented in carbonatic minerals show increased concentrations in the sample. This misleading result can possibly be deduced from the fact that the chemical composition from this investigated spot is located in a catchment area that is geologically completely different from the rest of the ARB. Alternating albite-bearing chlorite-phyllite and quartzite formations dominate the Monti Pisani area (Bagnoli et al., 1979) and drain into the Zambra river, along which sample ZA17 was extracted. XRF data show increased concentrations of the elements Ti, Al, Fe, K, P, Cu, Pb, Zn, and V.

All other sampling sites show no significant compositional changes. The stream sediments of the Arno river seem to be less affected. This is deduced by both the RMD and RFA analysis. Dinelli et al. (2005) describes a homogenizing effect of the Arno river, which is also visible in this study. The stream sediments of the main course are more resilient to compositional changes than the side tributaries.

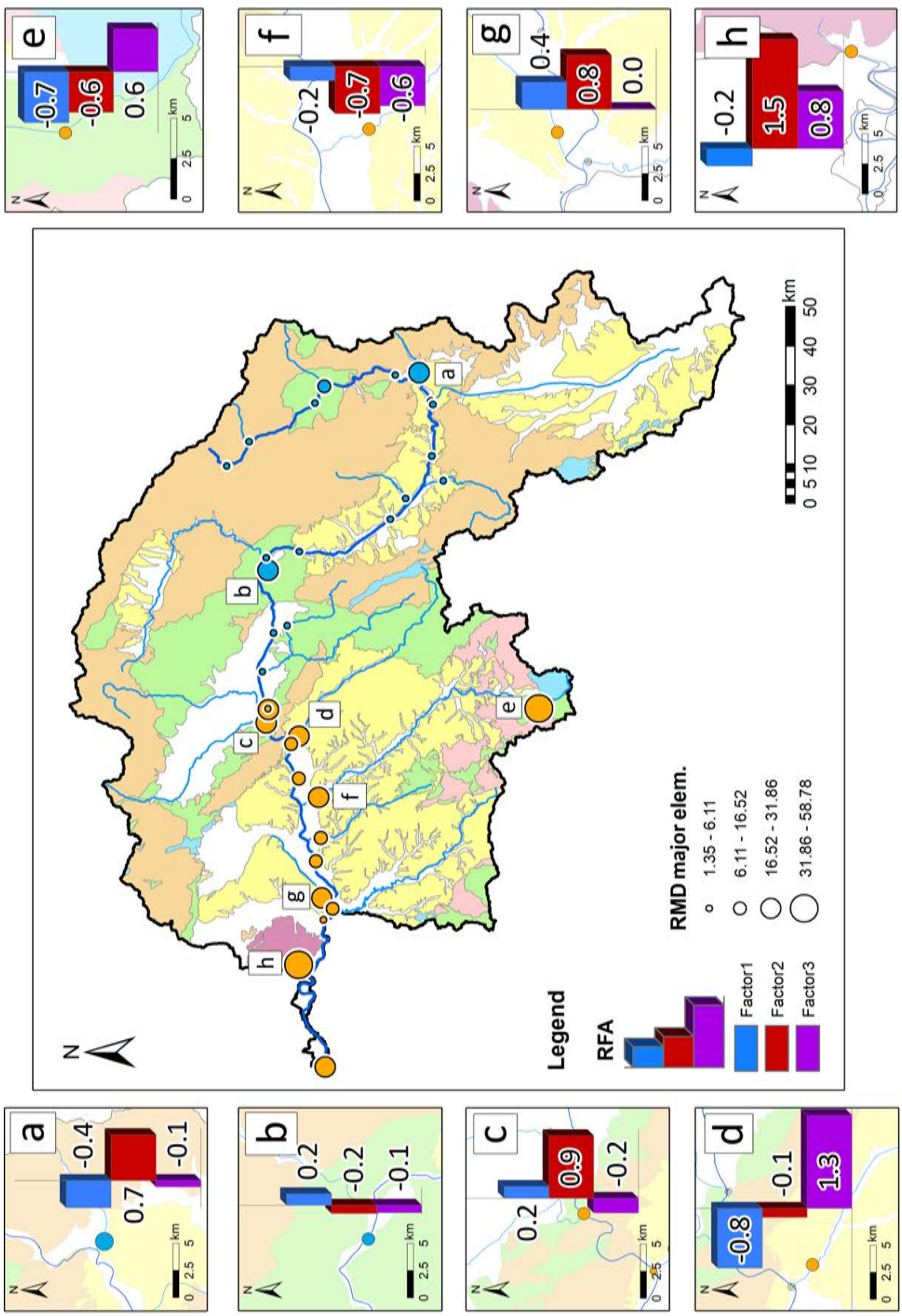

Figure 17 RMD for major elements illustrated on a schematic lithological map modified after Carmignani et al. (2013) and correlated with the results of the RFA for samples CH3 (a), ARNIX (b), OM10 (c), PE11 (d), EL12 (e), EL13 (f), US15 (g) and ZA17 (h). Legend for lithologies in Fig. 3.

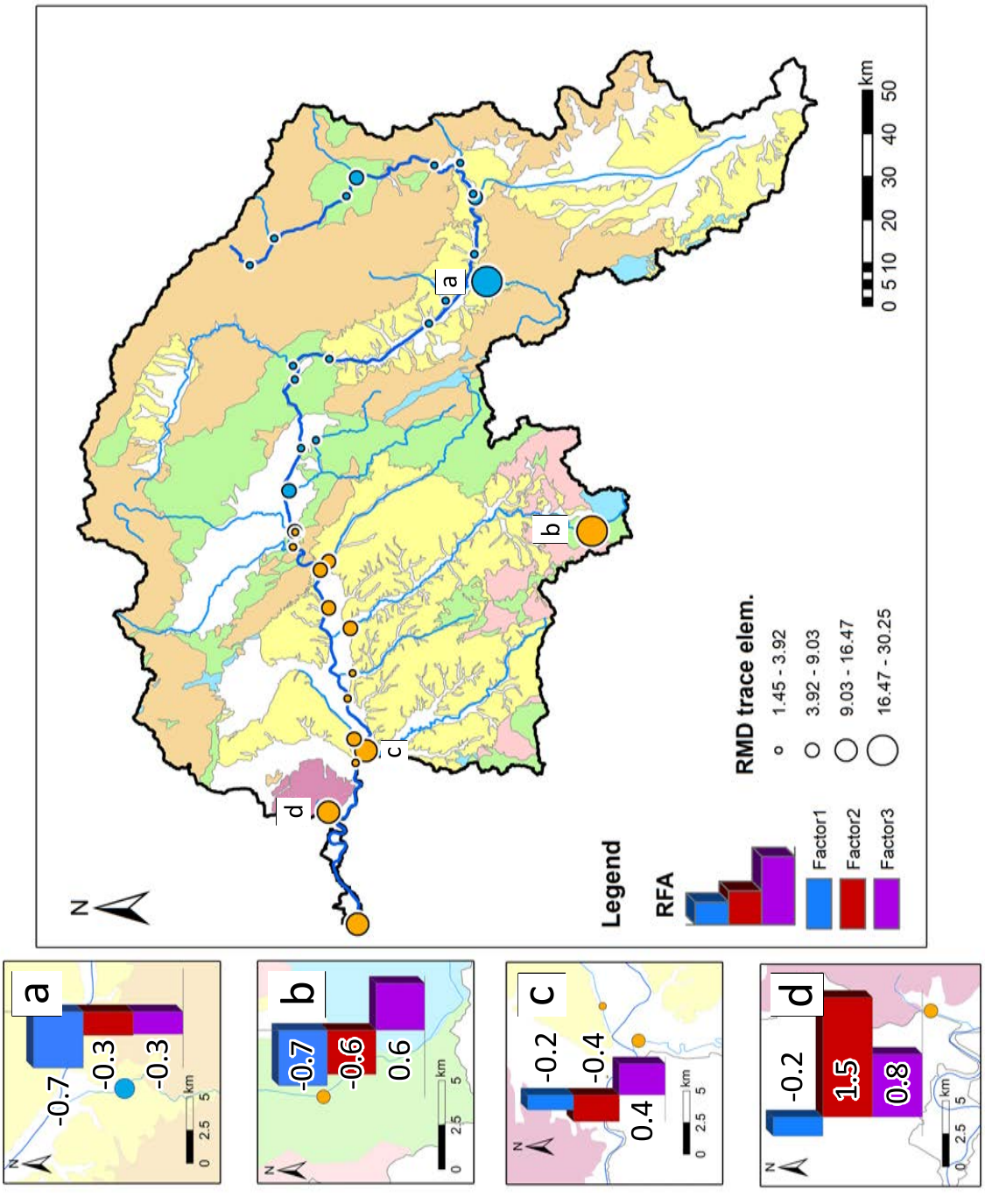

Figure 18 RMD for trace elements illustrated on a schematic lithological map modified after Carmignani et al. (2013) and correlated with the results of the RFA for samples AM4 (a), EL12 (b), ER16 (c) and ZA17 (d). Legend for lithologies in Fig. 3.

5.3 Magnetic Susceptibility

The results of the magnetic susceptibility coincide well with the findings described above. EL12 represents an outlier of the data and is explained by it's lithological features, supporting the outcome of all other analysis.

ZA17 represents the maximum measured magnetic susceptibility within the basin. This sample is draining from albite-bearing chlorite-phyllite and quartzite formations in the Monti Pisani area (Bagnoli et al., 1979), which might be the source of the high amount of ferromagnetic particles.

Chapter Six

Conclusions

A chemical analysis of stream sediments from the Arno river and its most important side tributaries was carried out. The obtained data were treated according to the approach of compositional data analysis. Methodically, the calculation of Robust Mahalanobis Distances, combined with a Robust Factor Analysis are effective tools to reveal and explain geochemical processes within the basin. Stream sediments of tributaries are more effected by changes than those of the main course. Thus, the Arno river sediments are resilient to geochemical threats. The chemical compositions of the investigated stream sediments reflect the bedrock geology prevalent in the catchment, but anthropogenic contaminations have to be considered as an important contributor to certain locations as well. The chemistry of stream sediments in the upstream part of the basin correlates well with the bedrock geology. Major changes are observed in the Chiana valley, where industrial and agricultural activities significantly influence the stream sediments. The stream sediments in the central and southern part of the basin around and downstream Florence are mainly dominated by the presence of ophiolitic rocks and to a minor extent of carbonates. P and Cu anomalies resulting from industrial settlements, as well as flower and plant gardens contaminate the Ombrone, Bisenzio and Usciana rivers.

References

Abbate, R., Castellucci, P., Ferrini, G.L., Pandeli, E., 1992. I dintorni di firenze. In Guide Geol. Reg., 4, Società Geologica Italiana , 214–223.

Aitchison, J., 1986. The Statistical Analysis of Compositional Data. Chapman and Hall, London, 416pp.

Albianelli, A., Azzaroli, A., Bertini, A., Ficcarelli, G., Napoleone, G., Torre, D., 1997. Paleomagnetic and palynologic investigations in the upper valdarno basin (central italy): calibration of an early villafranchian fauna. Rivista Italiana di Paleontologia e Stratigrafia 103, 111–118.

Andreozzi, M., Di Giulio, A., 1994. Stratigraphy and petrography of the mt. cervarola sandstones in the type area. Memorie della Società Geologica Italiana 48, 351–360.

Aruta, G., Bruni, P., Cecchi, G., Cipriani, N., Tredici, Y., 2003. Pliocene and pleistocene unconformity bounded units (ubsu) val di chiana. The Regione Toscana Project of Geological Mapping Case Hisories and Data Acquisition. Regione Toscana , pp. 133–136.

Bagnoli, G., Gianelli, G., Puxeddu, M., Rau, A., Squarci, P., Tongiorgi, M., 1979. A tentative stratigraphic reconstruction of the tuscan paleozoic basement. Memorie della Società Geologica Italiana 20, 99–116.

Basilevsky, A., 1994. Statistical Factor Analysis and Related Methods. Theory and Applications. Wiley, New York.

Bencini, A., Malesani, P., 1993. Fiume arno: acque, sedimenti e biosfera. Accademia Toscana Scienze Lettere "La Colombaria", studi 133 , 115 pp.

Berner, E.K., Berner, R.A., 1996. Global Environmental: Water, Air and Geochemical Cycles. Prentice-Hall, upper Saddle River NJ, p. 376.

Boccaletti, M., Coli, M., 1983. La tettonica della toscana: essetto ed evoluzione. Memorie della Società Geologica Italiana 25, 51–62.

Bossio, A., Costantini, A., Lazzarotto, A., Liotta, D., Mazzanti, R., Mazzei, R., Salvatorini, G., Sandrelli, F., 1993. Rassegna delle conoscenze sulla stratigrafia del neoautoctono toscano. Memorie della Società Geologica Italiana 49, 17–98.

Bruni, P., Cipriani, N., Pandeli, E., 1994. New sedimentological and petrographical data on the oligo-miocene turbiditic formations of the tuscan domain. Memorie della Società Geologica Italiana 48, 251–260.

Capecchi, F., Guazzone, G., Pranzini, G., 1975. Il bacino lacustre di firenze-prato-pistoia. geologia del sottosuolo e ricostruzione evolutiva. Boll. Soc. Geol. Ital. 94, 637–660.

Carmignani, L., Conti, P., Cornamusini, G., 2013. Geological map of tuscany (italy).

Carmignani, L., Decandia, F.A., Fantozzi, P.L., Lazzarotto, A., Liotta, D., Meccheri, M., 1994. Tertiary extensional tectonics in tuscany (northern apennines italy). Tectonophysics 238, 295–315.

Cencetti, C., Tacconi, P., 2005. The fluvial dynamics of the arno river. Giornale di Geologia Applicata 1, 193–202. doi:10.1474/GGA.2005-01.0-19.0019.

Comas-Cufí, M., Thió-Henestrosa, S. (Eds.), 2011. CoDaPack 2.0: a stand-alone, multi-platform compositional software. CoDaWork'11: 4th International Workshop on Compositional Data Analysis, Sant Feliu de Guíxols.

Consorzio Pisa Ricerche, 1998. Monitoraggio e controllo dell'inquinamento del fiume arno nel comprensorio del cuoio. Ed. ETS, Pisa , 1–29.

Conti, P., Cornamusini, G., Carmignani, L., 2020. An outline of the geology of the northern apennines (italy), with geological map at 1:250,000 scale. Italian Journal of Geosciences 139, 149–194. doi:10.3301/IJG.2019.25.

Cooper, D.C., Thornton, I., 1994. Drainage geochemistry in contaminated terrains. Handbook of Exploration Vol. 6 (Hale, M. and Plant, J. A., eds.), 447–497.

Cortecci, G., Dinelli, E., Bencini, A., Adorni Braccesi, A., La Ruffa, G., 2002. Natural and anthropogenic so4 sources in the arno river catchment, northern tuscany, italy: a chemical and isotopic reconnaissance. Applied Geochemistry 17, 79–92.

Dall'Aglio, M., 1971. La prospezione geochimica. Le Scienze 37, 13–21.

Dessau, G., 1974. Die lagerstätten toskanas im lichte der geologischen entwicklung des landes. Arch. Lagerstättenforsch. Ostalpen, Sonderbd. 2 (Festschrift O. M. Friedrich) , 51–77.

Dinelli, E., Cortecci, G., Lucchini, F., Zantedeschi, E., 2005. Sources of major and trace elements in the stream sediments of the arno river catchment (northern tuscany, italy). Geochemical Journal 39, 531–545.

Dinelli, E., Lucchini, F., Mordenti, A., Paganelli, L., 1999a. Geochemistry of oligocene-miocene sandstones of the northern apennines (italy) and evolution of chemical features in relation to provenance changes. Sedimentary Geology 127, 193–207.

Dinelli, E., Testa, G., Cortecci, G., Barbieri, M., 1999b. Stratigraphic and petrographic constrains to trace element and isoptope geochemistry of messinian sulphates of tuscany. Memorie della Società Geologica Italiana 54, 61–74.

Egozcue, J.J., Pawlowsky-Glahn, V., Mateu-Figueras, G., Barcel´o-Vidal, C., 2003. Isometric logratio transformations for compositional data analysis. Mathematical Geology 35, 270–300.

Elter, P., Giglia, G., Tongiorgi, M., Trevisan, L., 1975. Tensional and compressional areas (tortonian to present) evolution of the northern apennines. Bollettino di Geofisica Teorica Applicata 17, 3–18.

Filzmoser, P., Hron, K., 2008. Outlier detection for compositional data using robust methods. Mathematical Geosciences 40, 233–248. doi:10.1007/s11004-007-9141-5.

Filzmoser, P., Hron, K., Reimann, C., 2009a. Univariate statistical analysis of environmental (compositional) data: Problems and possibilities. Science of The Total Environment 407, 6100–6108. doi:10.1016/j.scitotenv.2009.08.008.

Filzmoser, P., Hron, K., Reimann, C., 2012. Interpretation of multivariate outliers for compositional data. Computers & Geosciences 39, 77–85. doi:10.1016/j.cageo.2011.06.014.

Filzmoser, P., Hron, K., Reimann, C., Garrett, R., 2009b. Robust factor analysis for compositional data. Computers & Geosciences 35, 1854–1861.

Förstner, U., 1983. Assessment of metal pollution in rivers and estuaries. Applied Environmental Geochemistry (Thornton, I., ed.) , 395–423.

Gozzi, C., Filzmoser, P., Buccianti, A., Vaselli, O., Nisi, B., 2019. Statistical methods for the geochemical characterisation of surface waters: The case study of the tiber river basin (central italy). Computers & Geosciences , 80–88doi:10.1016/j.cageo.2019.06.011.

Gozzi, G., 2020. Weathering and transport processes investigated through the statistical properties of the geochemical landscapes: the case study of the Tiber River Basin (central Italy). Phd thesis. Università di Pisa.

Grassi, S., Cortecci, G., Squarci, P., 2007. Groundwater resource degradation in coastal plains: the example of the cecina area (tuscany-central italy). Applied Geochemistry 22, 2273–2289.

Hanesch, M., Rantitsch, G., Hemetsberger, S., Scholger, R., 2007. Lithological and pedological influences on the magnetic susceptibility of soil: their consideration in magnetic pollution mapping. The Science of the total environment 382, 351–363. doi:10.1016/j.scitotenv.2007.04.007.

Howarth, R.J., Thornton, I., 1983. Regional geochemical mapping and its application to environmental studies. Applied Environmental Geochemistry (Thornton, I., ed.) , 41–73.

Ielpi, A., 2011. Geological map of the santa barbara basin (northern apennines, italy). Journal of Maps 7, 614–625.

ISPRA, 2020. Rete del sistema informativo nazionale ambientale. URL: http://www.sinanet.isprambiente.it/.

Johnson, R., Wichern, D., 2007. Applied Multivariate Statistical Analysis. Prentice-Hall, London,.

Kynclová, P., Hron, K., Filzmoser, P., 2017. Correlation between compositional parts based on symmetric balances. Mathematical Geosciences 49, 777–796.

Levinson, A.A., 1974. Introduction to Exploration Geochemistry. Applied Publ. Co., Calgary, 612 pp.

Maechler, M., Rousseeuw, P., Croux, C., Todorov, V., Ruckstuhl, A., Salibian-Barrera, M., Verbeke, T., Koller, M., Conceicao, E., Di Anna Palma, M., 2019. Basic robust statistics. URL: http://robustbase.r-forge.r-project.org/.

Maronna, R., Martin, D., Yohai, V., 2006. Robust Statistics: Theory and Methods. John Wiley & Sons Ltd., Toronto (ON), p.436.

Moretti, S., 1994. The northern apennines. Proceeding 76th Summer Meeting of the Italian Geological Society , 739–956.

Nardi, R., 1993. L'arno e le sue acque: contributo conoscitivo per l'elaborazione del piano di bacino. Quaderno n. 1, Autorità di Bacino del fiume Arno (Firenze) .

Nisi, B., Buccianti, A., Vaselli, O., Perini, G., Tassi, F., Minissale, A., Montegrossi, G., 2008. Hydrogeochemistry and strontium isotopes in the arno river basin (tuscany, italy): Constraints on natural controls by statistical modeling. Journal of Hydrology , 166–183doi:10.1016/j.jhydrol.2008.07.030.

Nisi, B., Vaselli, O., Buccianti, A., Silva, S.R., 2005. Sources of nitrate in the arno river waters: constraints d15n and d18o. GeoActa 4, 13–24.

Pawlowsky-Glahn, V., Egozcue, J.J., 2001. Geometric approach to statistical analysis on the simplex. Stoch Environ Res Risk Assess (SERRA) 15, 384–398.

Pranzini, G., 1994. Water resources of the arno basin. Memorie della Società Geologica Italiana 48, 785–794.

Rantitsch, G., 2001. The fractal properties of geochemical landscapes as an indicator of weathering and transport processes within the eastern alps. Journal of Geochemical Exploration 73, 27–42. doi:10.1016/S0375-6742(01)00168-6.

Rau, A., Tongiorgi, M., 1974. Geologia dei monti pisani a sud-est della valle del guappero. Memorie della Società Geologica Italiana 13, 227–408.

Reimann, C., Filzmoser, P., Garrett, R.G., 2002. Factor analysis applied to regional geochemical data: problems and possibilities. Applied Geochemistry 17, 185–206. doi:10.1016/S0883-2927(01)00066-X.

Reimann, C., Filzmoser, P., Garrett, R.G., Dutter, R., 2008. Statistical data analysis explained. John Wiley & Sons.

Ripley, B., Venables, B., Bates, D.M., Hornik, K., Gebhardt, A., Firth, D., 2019. Support functions and datasets for venables and ripley's mass. URL: http://www.stats.ox.ac.uk/pub/MASS4/.

Rose, A.W., Hawkes, M.E., Webb, J.S., 1979. Geochemistry in Mineral Exploration. 2nd ed., Academic Press, 657 pp.

Rousseeuw, P., van Zomeren, B., 1990. Unmasking multivariate outliers and leverage points. Journal of the American Statistical Association 85, 633–651.

Salomons, W., Förstner, U., 1984. Metals in the Hydrocycle. Springer-Verlag, 349 pp.

Scholger, R., 1998. Heavy metal pollution monitoring by magnetic susceptibility measurements applied to sediments of the river mur (styria, austria). Journal of Enviromental and Engineering Geophysics 3, 25–37.

Templ, M., Hron, K., Filzmoser, P., 2011. Compositional data analysis.

Warnes, G.R., Bolker, B., Bonebakker, L., Gentleman, R., Huber, W., Liaw, A., Lumley, T., Maechler, M., Magnusson, A., Moeller, S., Schwartz, M., Venables, B., Galili, T., 2020. Various r programming tools for plotting data.

APPENDICES

Appendix A

Stream Sediment Data

Sample		River name	Location	Date	Coordinates (WGS84)	
ID	ID after Nisi et al. (2008)				lat	lon
ARNI	2CAII	Arno	Casina	27.08.2019	43.680323	11.835019
ARNII	2CAVI	Arno	Ortignano Raggioto (Bibbiena)	27.08.2019	43.523571	11.865563
ARNIII	2CAXI	Arno	Capolona	27.08.2019	43.841599	11.653051
ARNIV	2CHXIV	Arno	Ponte a Buriano	27.08.2019	43.695976	11.796820
ARNV	CH1	Arno	Chiana	27.08.2019	43.562641	11.860859
ARNVI	2VASXVI	Arno	Ponte del Romito	27.08.2019	43.722728	11.035699
ARNVII	2VASXX	Arno	S. Giovanni Valdarno	27.08.2019	43.776432	11.443134
ARNVIII	2VASXXII	Arno	Rignano	27.08.2019	43.666257	10.640744
ARNIX	2VASXXV	Arno	Rosano	27.08.2019	43.684638	10.665222
ARNX	2VAMXXVIII	Arno	S. Niccolò	26.08.2019	43.324645	11.098912
ARNXI	Arno Signa	Arno	Arno a Signa	26.08.2019	43.773379	11.09743
ARNXII	2VAIXXXIV	Arno	Montelupo Fiorentino	26.08.2019	43.679464	10.279232
ARNXIII	2VAIXXXV	Arno	Empoli	26.08.2019	43.682245	10.615355
ARNXIV	2VAIXXXVIII	Arno	Castelfranco	26.08.2019	43.483285	11.618801
ARNXV	2VAIXL	Arno	Calcinaia	26.08.2019	43.546255	11.578893
ARNXVI	2VAIL	Arno	Foce	26.08.2019	43.741444	11.287172
ST1	Staggia	Staggia	Staggia	27.08.2019	43.764454	11.270425
CO2	2CA16T	Corsalone	Corsalone	27.08.2019	43.504445	11.800448
CH3	2CA28T	Chiassa	Ponte alla Chiassa	27.08.2019	43.78243	11.182413
AM4	2VAS38T	Ambra	Bucine	27.08.2019	43.723233	10.512962
CI5	2VAS45T	Loro Ciuffenna	Terranuova Bracciolini	27.08.2019	43.686478	10.802051
SI6	2SI62A	Sieve	Pontassieve	27.08.2019	43.689880	10.895807
EM7	Ema	Ema	Ponte a Ema	27.08.2019	43.804957	11.708819
GR8	2GR70H	Greve	Mantignano	26.08.2019	43.694257	10.748742
BI9	2VAM79T	Bisenzio	Ponte a Signa	26.08.2019	43.722760	10.938184
OM10	2VAM76T	Ombrone	Stazione Carmignano	26.08.2019	43.735261	11.017254
PE11	2PE75A	Pesa	Montelupo Fiorentino	26.08.2019	43.776869	11.065008
EL12	2VAI95T	Elsa	Pievescola	26.08.2019	43.721740	11.457139
EL13	2VAI89T	Elsa	Ponte a Elsa	26.08.2019	43.571540	11.530997
EG14	2VAI88T	Egola	Ponte a Egola	26.08.2019	43.502494	11.674888
US15	2VAI105T	Usciana	Montecalvoli	26.08.2019	43.773015	11.096162
ER16	2VAI103T	Era	Pontedera	26.08.2019	43.773649	11.414300
ZA17	2VAI133T	Zambra	Calci	26.08.2019	43.500677	11.793127

Table 3 Locations of the stream sediment samples.

Sample	ARNI	ARNII	ARNIII	ARNIV	ARNV	ARNVI	ARNVII	ARNVIII	ARNIX	ARNX	ARNXI	ARNXII	ARNXIII	ARNXIV	ARNXV	ARNXVI
Σ [% wt]	99.46	100.93	99.49	99.01	98.97	98.32	98.66	98.95	97.74	99.87	101.50	98.07	100.97	98.22	97.61	101.41
SiO2 [% wt]	67.54	71.14	59.43	56.95	54.63	69.16	70.55	72.48	66.84	64.53	62.86	68.00	53.17	66.18	63.85	44.78
TiO2 [% wt]	0.45	0.52	0.51	0.54	0.49	0.48	0.48	0.41	0.58	0.51	0.56	0.54	0.52	0.48	0.47	0.49
Al2O3 [% wt]	11.40	11.38	11.95	11.87	10.51	11.25	11.32	10.26	10.31	11.67	12.60	10.66	10.76	10.55	10.83	10.95
Fe2O3 [% wt]	3.07	3.91	4.10	4.61	3.47	3.48	3.33	2.78	3.19	3.59	4.02	3.53	4.75	3.46	3.51	4.07
MnO [% wt]	0.07	0.10	0.08	0.11	0.12	0.08	0.06	0.07	0.10	0.07	0.08	0.09	0.15	0.09	0.08	0.31
MgO [% wt]	2.05	1.66	2.31	2.19	1.84	1.56	1.48	1.26	1.41	1.71	1.80	1.60	1.92	1.48	1.62	2.93
CaO [% wt]	1.64	3.21	7.03	9.36	18.10	3.07	2.50	3.18	5.09	5.34	5.93	4.28	12.58	5.82	5.67	13.52
Na2O [% wt]	1.78	1.38	1.39	0.95	0.99	1.83	1.57	1.68	1.44	1.43	1.16	1.36	0.66	1.41	1.33	1.91
K2O [% wt]	2.25	1.74	1.92	2.03	1.71	1.91	2.05	2.02	1.94	2.00	1.94	2.02	1.64	1.87	1.94	1.13
P2O5 [% wt]	0.11	0.13	0.15	0.16	0.22	0.12	0.11	0.10	0.13	0.14	0.23	0.13	0.14	0.11	0.14	0.20
LOI [% wt]	9.00	5.57	10.53	10.15	6.77	5.34	5.13	4.63	6.71	8.73	9.99	5.80	14.38	6.73	8.21	20.66
Cu [mg*kg^{-1}]	12	18	19	75	78	13	23	12	23	34	61	23	58	21	43	14
Ce [mg*kg-1]	88	114	<60	98	64	<60	<60	62	<60	82	120	99	97	<60	<60	98
Nb [mg*kg-1]	12	13	12	11	8	12	11	10	14	13	11	11	10	11	11	6
Zr [mg*kg-1]	177	181	175	165	205	195	192	193	227	220	294	282	163	256	210	205
Y [mg*kg-1]	22	20	22	23	20	24	18	15	22	40	25	21	24	20	20	16
Sr [mg*kg-1]	150	139	221	223	623	145	130	144	175	175	200	168	294	194	187	601
Rb [mg*kg-1]	91	76	84	90	77	79	85	78	80	88	88	83	75	79	83	29
Th [mg*kg-1]	7	9	10	10	6	11	10	10	13	9	14	11	10	7	9	7
Pb [mg*kg-1]	37	26	17	54	28	11	29	30	25	26	52	118	22	23	21	<7
Ga [mg*kg-1]	15	13	16	15	14	16	16	16	15	13	18	15	14	15	14	10
Zn [mg*kg-1]	76	78	77	134	97	64	65	64	64	83	124	89	88	65	76	118
Ni [mg*kg-1]	50	44	56	85	43	45	47	36	40	55	55	48	70	46	59	65
Co [mg*kg-1]	10	12	12	16	11	13	11	7	8	15	11	<8	12	11	15	11
V [mg*kg-1]	55	63	59	74	68	55	59	47	59	67	65	64	65	59	64	70
La [mg*kg-1]	<63	<63	<63	<63	<63	<63	<63	<63	<63	<63	<63	<63	<63	<63	<63	<63
Ba [mg*kg-1]	427	311	431	427	370	378	421	417	493	401	523	412	271	391	395	273
Sc [mg*kg-1]	15	14	12	10	7	14	15	14	13	12	12	14	8	12	13	7
Cr [mg*kg-1]	106	84	91	165	93	82	96	137	148	99	140	111	152	166	111	134
Cs [mg*kg-1]	<43	<43	<43	<43	<43	<43	<43	<43	<43	<43	<43	<43	<43	<43	<43	<43
Hf [mg*kg-1]	8	7	<8	<8	8	8	11	<8	<8	<8	10	<8	<8	13	12	12
Nd [mg*kg-1]	33	38	<24	43	26	<24	<24	31	<24	25	44	36	30	<24	28	36
MS [10^{-8}*m^3*kg^{-1}]	24.64	52.48	17.82	14.79	14.15	12.27	12.04	19.10	28.44	15.66	33.53	43.85	25.71	20.18	16.00	21.97

Table 4 Chemical composition of Arno river stream sediments sampled in August 2019. The last line (MS) shows the measured magnetic susceptibilities.

Sample	ST1	CO2	CH3	AM4	CI5	SI6	EM7	GR8	BI9	OM10	PE11	EL12	EL13	EG14	US15	ER16	ZA17
Σ [% wt]	99.52	98.79	100.32	100.73	99.32	98.52	98.89	98.13	98.51	98.48	99.72	97.38	99.75	99.21	98.67	98.97	100.81
SiO2 [% wt]	63.44	49.19	54.26	49.78	69.45	61.92	56.17	54.68	61.81	67.67	44.54	41.04	61.61	65.97	72.04	56.44	51.27
TiO2 [% wt]	0.49	0.45	0.54	0.43	0.49	0.43	0.51	0.55	0.45	0.58	0.58	0.56	0.39	0.51	0.48	0.48	0.63
Al2O3 [% wt]	11.23	10.82	11.61	9.31	11.53	10.37	11.39	10.94	10.56	12.09	11.88	8.03	7.93	11.49	11.37	10.13	11.81
Fe2O3 [% wt]	3.53	4.15	3.97	3.05	3.45	3.13	4.26	4.51	3.37	4.07	4.98	4.27	2.56	3.56	3.27	3.78	4.24
MnO [% wt]	0.08	0.11	0.08	0.11	0.09	0.07	0.10	0.11	0.06	0.06	0.12	0.10	0.07	0.06	0.04	0.08	0.05
MgO [% wt]	2.08	2.06	2.32	1.62	1.96	1.50	2.03	2.30	1.76	2.11	1.77	3.05	1.29	1.64	1.30	2.22	1.36
CaO [% wt]	5.12	14.65	6.71	15.85	3.04	8.41	8.65	9.88	7.59	2.14	15.71	18.84	11.79	5.06	1.45	9.97	1.67
Na2O [% wt]	1.63	1.08	1.18	0.88	1.72	1.29	0.95	0.85	1.36	1.58	0.09	0.44	1.08	1.23	1.48	0.91	0.16
K2O [% wt]	2.02	1.66	2.03	1.54	2.10	1.71	1.92	1.82	1.78	2.14	1.58	0.83	1.39	2.09	2.10	1.87	2.38
P2O5 [% wt]	0.15	0.14	0.34	0.20	0.13	0.14	0.15	0.18	0.14	0.21	0.19	0.12	0.10	0.10	0.15	0.12	0.27
LOI [% wt]	9.61	14.48	17.04	17.67	5.24	9.54	12.72	12.35	9.62	5.76	18.18	20.48	11.43	7.41	4.91	12.95	26.60
Cu [mg*kg^{-1}]	26	14	97	64	61	27	64	57	39	55	69	31	19	31	44	34	111
Ce [mg*kg-1]	59	60	88	92	<60	<60	53	<60	<60	<60	62	61	86	<60	<60	52	77
Nb [mg*kg-1]	13	8	12	7	13	10	11	12	10	14	12	6	7	11	10	9	15
Zr [mg*kg-1]	239	126	169	197	208	151	174	176	178	254	126	94	222	184	201	160	197
Y [mg*kg-1]	23	23	24	18	23	20	23	22	18	20	25	13	17	25	20	18	33
Sr [mg*kg-1]	198	428	182	543	146	243	208	236	230	112	299	320	318	159	112	272	55
Rb [mg*kg-1]	84	72	93	68	85	71	86	81	77	92	82	40	56	91	92	80	104
Th [mg*kg-1]	11	<7	9	9	11	7	10	9	8	11	7	<7	7	10	9	8	12
Pb [mg*kg-1]	35	18	26	18	27	22	66	28	47	56	23	31	65	16	22	12	52
Ga [mg*kg-1]	17	14	16	<2	14	14	15	16	13	17	14	12	12	15	16	15	16
Zn [mg*kg-1]	224	73	153	83	107	68	118	113	125	159	101	67	52	61	131	90	184
Ni [mg*kg-1]	47	50	66	38	59	34	80	89	47	59	59	146	43	48	49	73	33
Co [mg*kg-1]	<8	16	10	9	10	<8	14	20	10	8	18	24	6	12	14	14	13
V [mg*kg-1]	58	64	63	58	58	52	63	67	59	70	86	76	46	56	59	60	74
La [mg*kg-1]	<63	<63	<63	<63	<63	<63	<63	<63	<63	<63	<63	<63	<63	<63	<63	<63	<63
Ba [mg*kg-1]	523	641	536	337	454	417	452	382	481	424	427	124	250	362	345	268	406
Sc [mg*kg-1]	11	7	10	6	15	11	9	10	11	15	6	5	8	13	15	9	12
Cr [mg*kg-1]	110	95	109	76	100	105	216	358	84	161	131	532	136	114	162	286	66
Cs [mg*kg-1]	<43	<43	<43	<43	<43	<43	<43	<43	<43	<43	<43	<43	<43	<43	<43	<43	<43
Hf [mg*kg-1]	<8	<8	<8	<8	<8	<8	<8	<8	<8	<8	<8	<8	<8	<8	7	9	6
Nd [mg*kg-1]	25	21	34	26	27	23	19	23	<24	<24	25	23	33	25	29	23	33
MS [10^{-8}*m^3*kg^{-1}]	55.95	12.13	19.78	16.01	25.65	16.21	45.46	65.67	22.99	31.49	15.71	84.06	16.34	28.48	14.57	33.68	162.39

Table 5 Chemical composition of stream sediments from the main tributaries of the ARB sampled in August 2019. The last line (MS) shows the measured magnetic susceptibilities.

Element	CLR Variance [%]
Ca	13.75
Na	11.03
Pb	9.40
Cu	9.22
Sr	6.90
Ga	5.14
Cr	4.90
Ce	4.36
Co	3.77
Hf	3.37
Mn	3.05
Sc	2.69
Nd	2.61
Zn	2.44
Ni	2.06
Ba	2.02
Th	1.96
P	1.92
Rb	1.36
Zr	1.29
Nb	1.21
Mg	1.08
K	1.00
Y	0.90
Si	0.84
Fe	0.40
V	0.32
La	0.28
Cs	0.28
Ti	0.24
Al	0.21

Table 6 Clr Variances sorted according to their values and calculated as described in section 4.2.

Appendix B

Geochemical Atlas

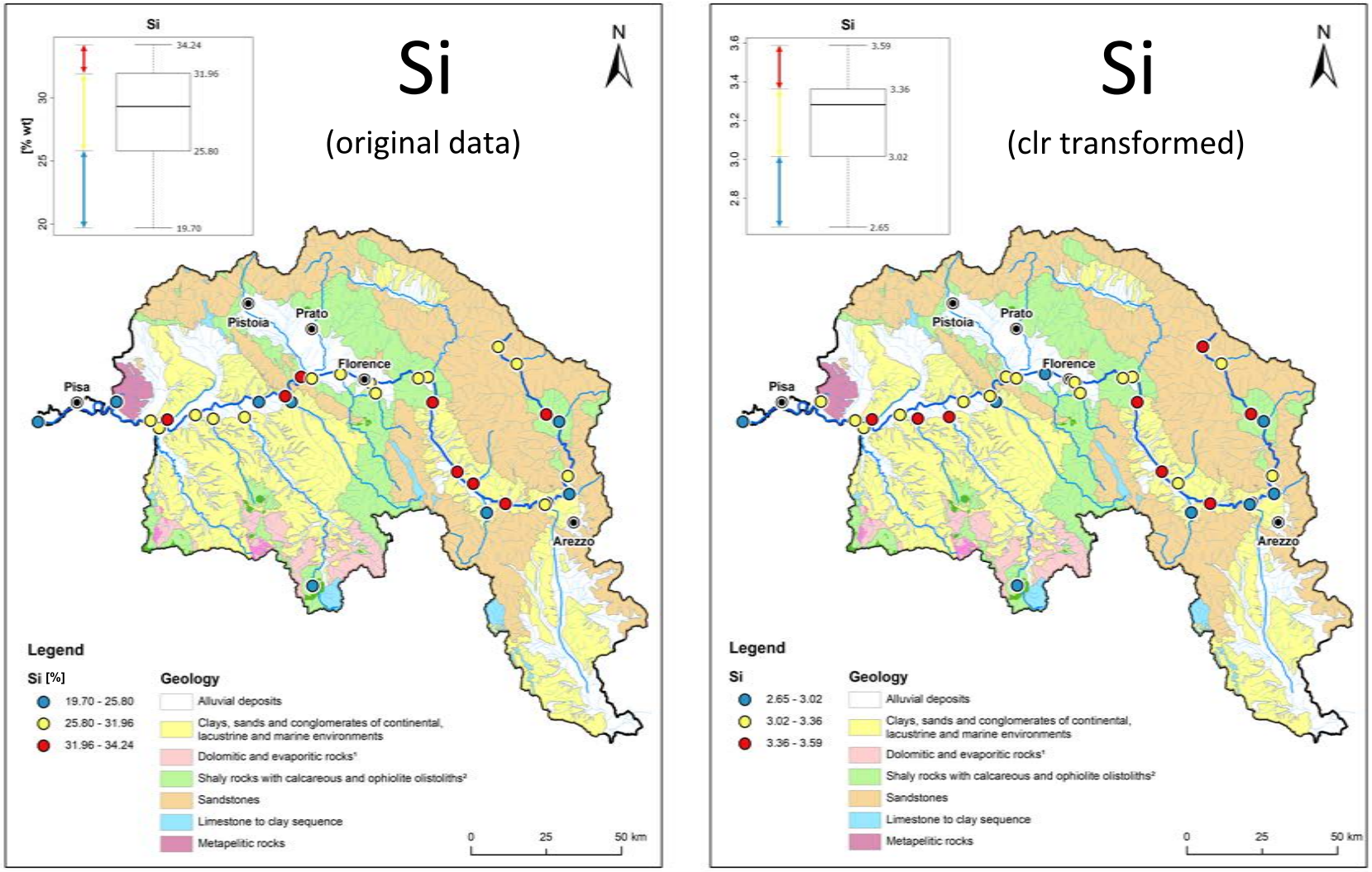

Figure 19 Distribution of the original data (left) and clr transformed data (right) of Si in stream sediments presented on a schematic lithological map modified after Carmignani et al. (2013).

[1]: Evaporites highlighted with a more saturated color. [2]: Ophiolites highlighted with a more saturated color.

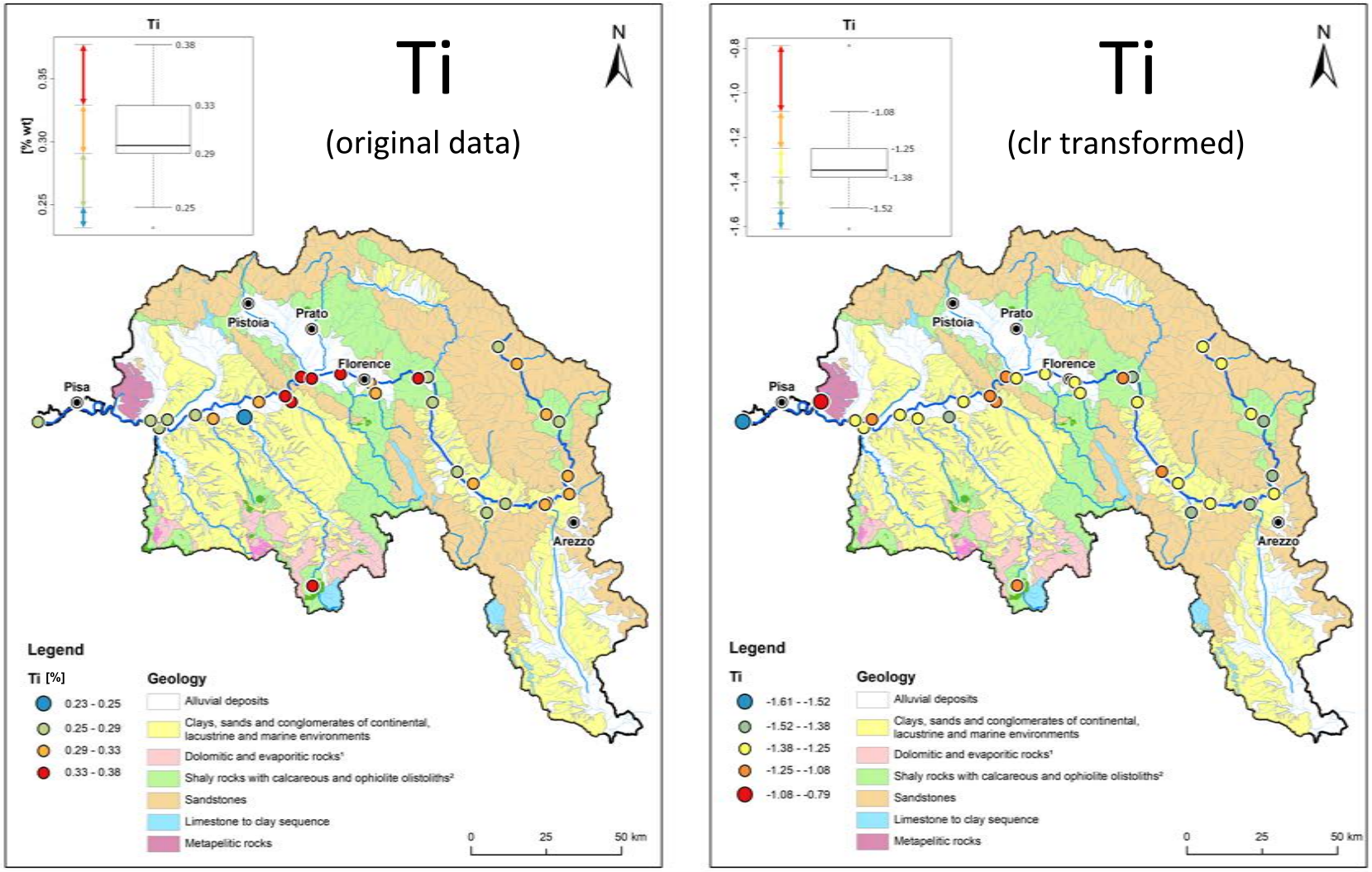

Figure 20 Distribution of the original data (left) and clr transformed data (right) of Ti in stream sediments presented on a schematic lithological map modified after Carmignani et al. (2013).

[1]: Evaporites highlighted with a more saturated color. [2]: Ophiolites highlighted with a more saturated color.

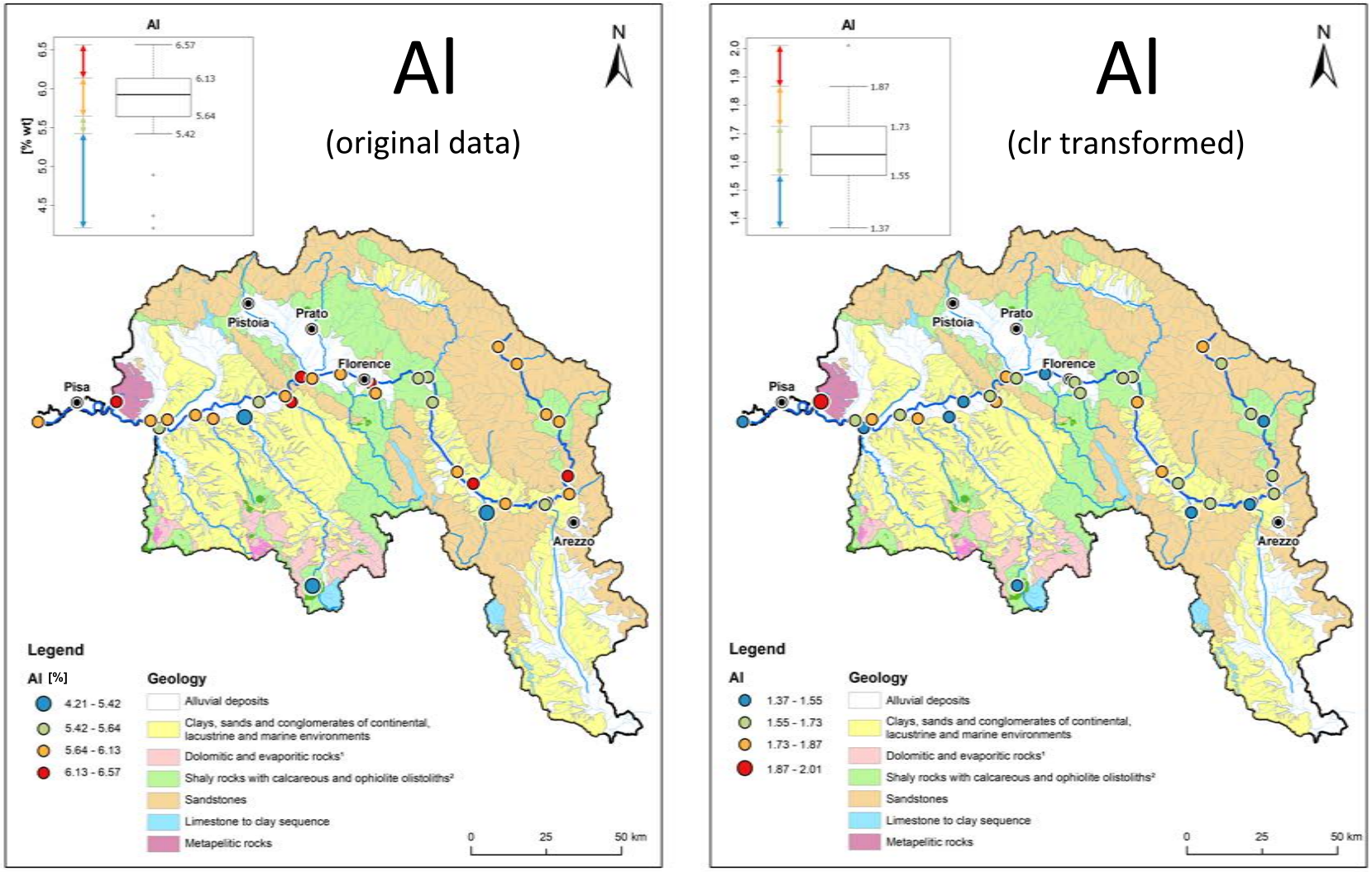

Figure 21 Distribution of the original data (left) and clr transformed data (right) of Al in stream sediments presented on a schematic lithological map modified after Carmignani et al. (2013).

[1]: Evaporites highlighted with a more saturated color. [2]: Ophiolites highlighted with a more saturated color.

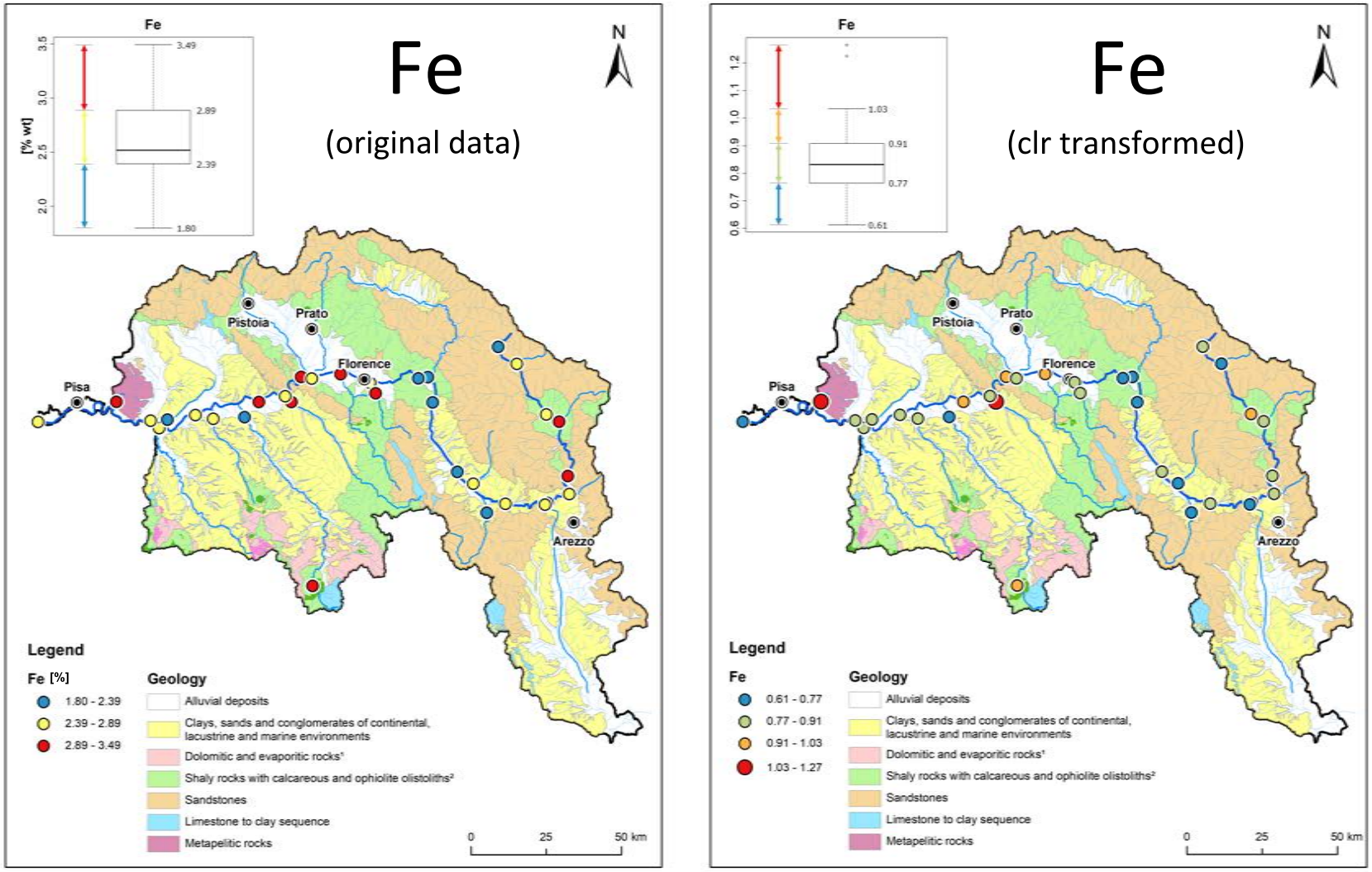

Figure 22 Distribution of the original data (left) and clr transformed data (right) of Fe in stream sediments presented on a schematic lithological map modified after Carmignani et al. (2013).

[1]: Evaporites highlighted with a more saturated color. [2]: Ophiolites highlighted with a more saturated color.

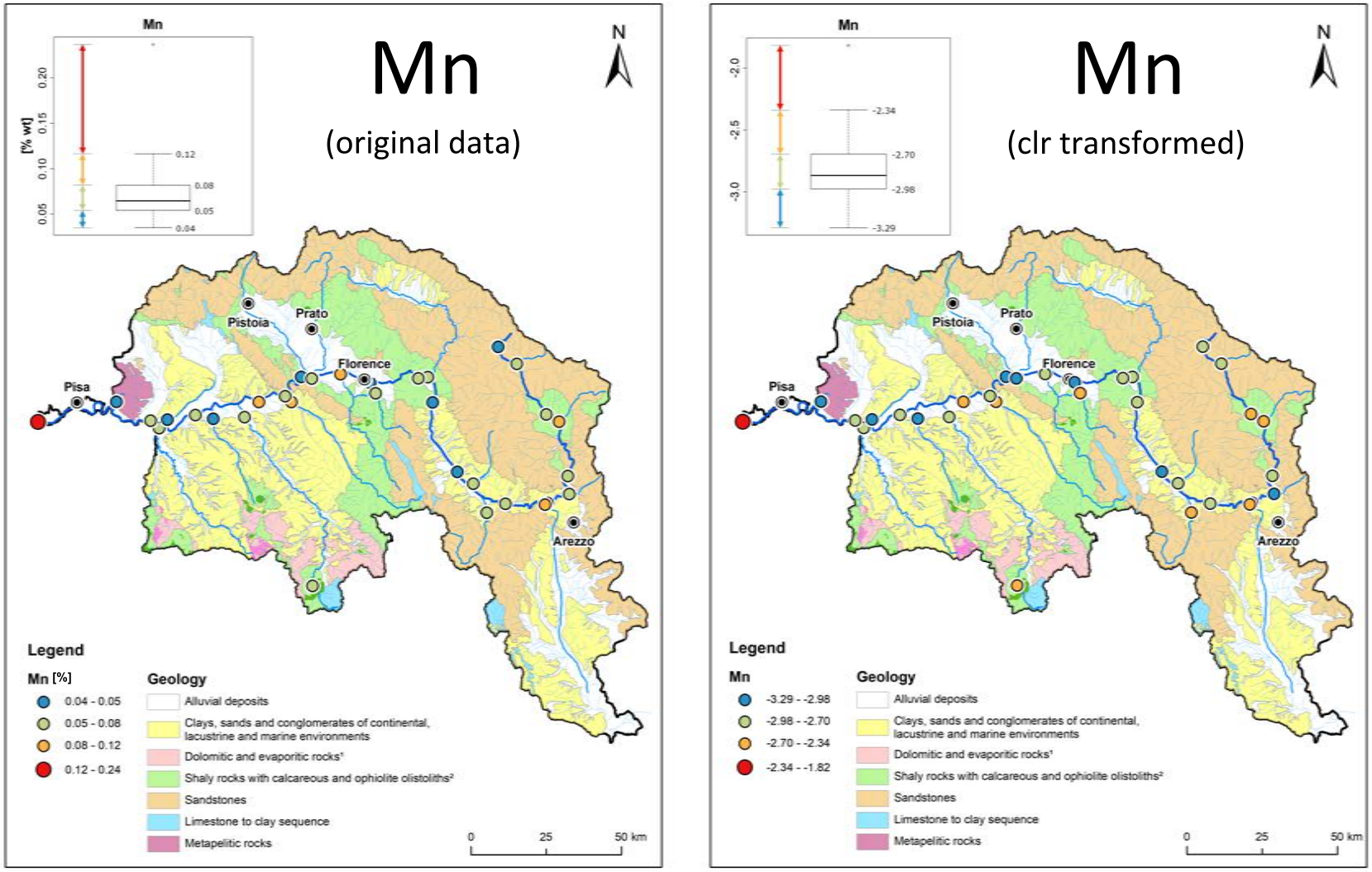

Figure 23 Distribution of the original data (left) and clr transformed data (right) of Mn in stream sediments presented on a schematic lithological map modified after Carmignani et al. (2013).

[1]: Evaporites highlighted with a more saturated color. [2]: Ophiolites highlighted with a more saturated color.

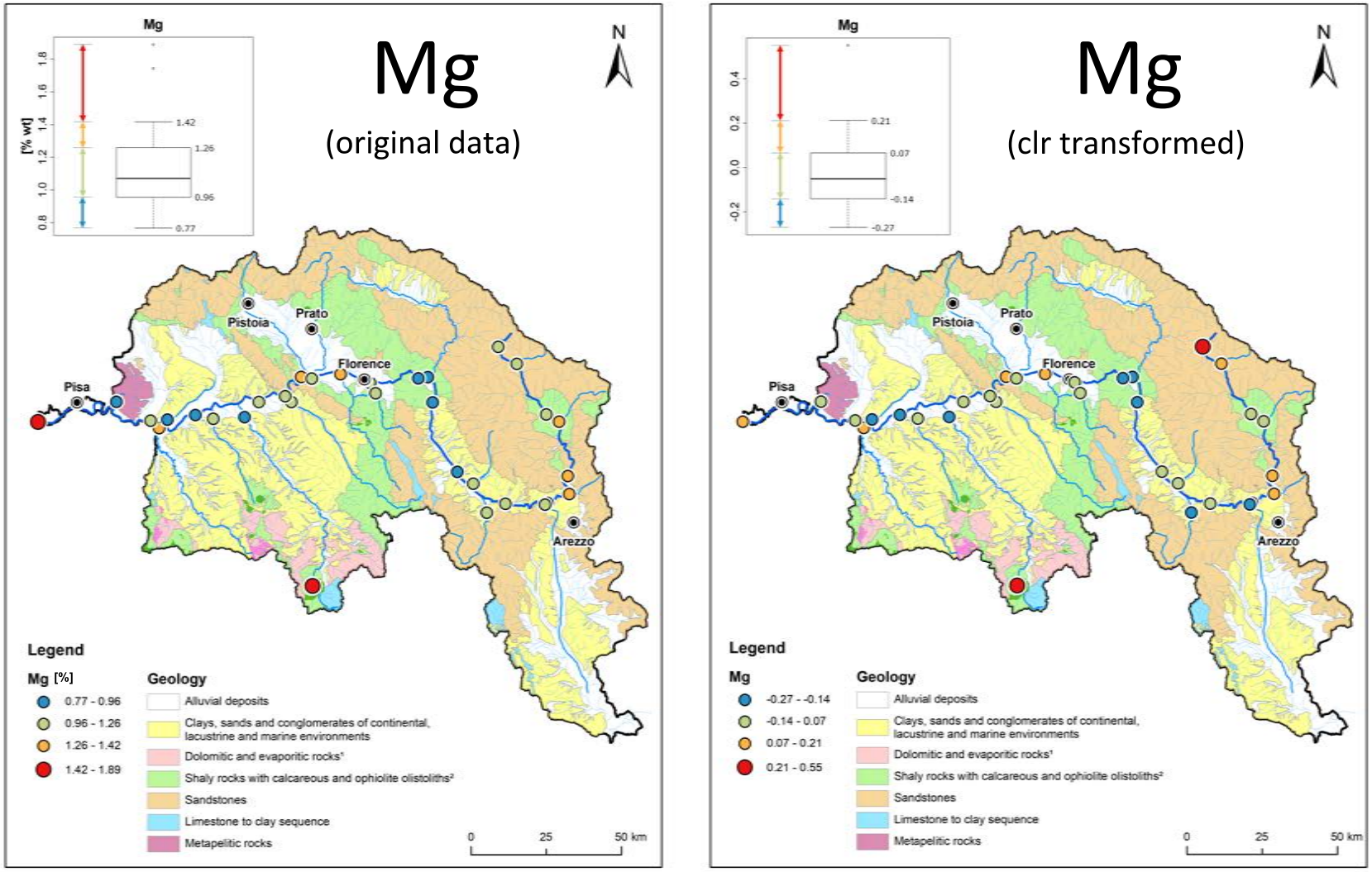

Figure 24 Distribution of the original data (left) and clr transformed data (right) of Mg in stream sediments presented on a schematic lithological map modified after Carmignani et al. (2013).

[1]: Evaporites highlighted with a more saturated color. [2]: Ophiolites highlighted with a more saturated color.

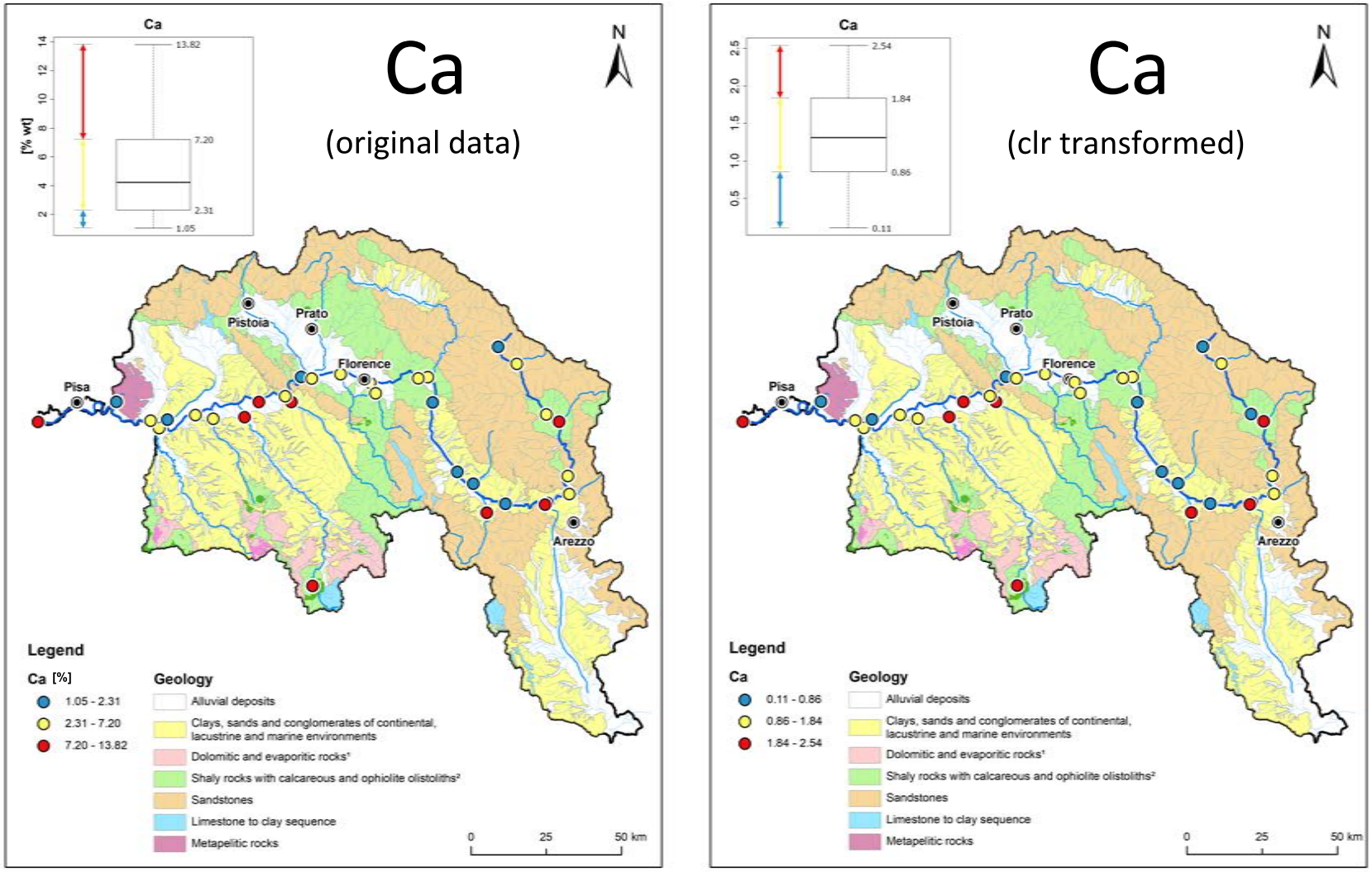

Figure 25 Distribution of the original data (left) and clr transformed data (right) of Ca in stream sediments presented on a schematic lithological map modified after Carmignani et al. (2013).

[1]: Evaporites highlighted with a more saturated color. [2]: Ophiolites highlighted with a more saturated color.

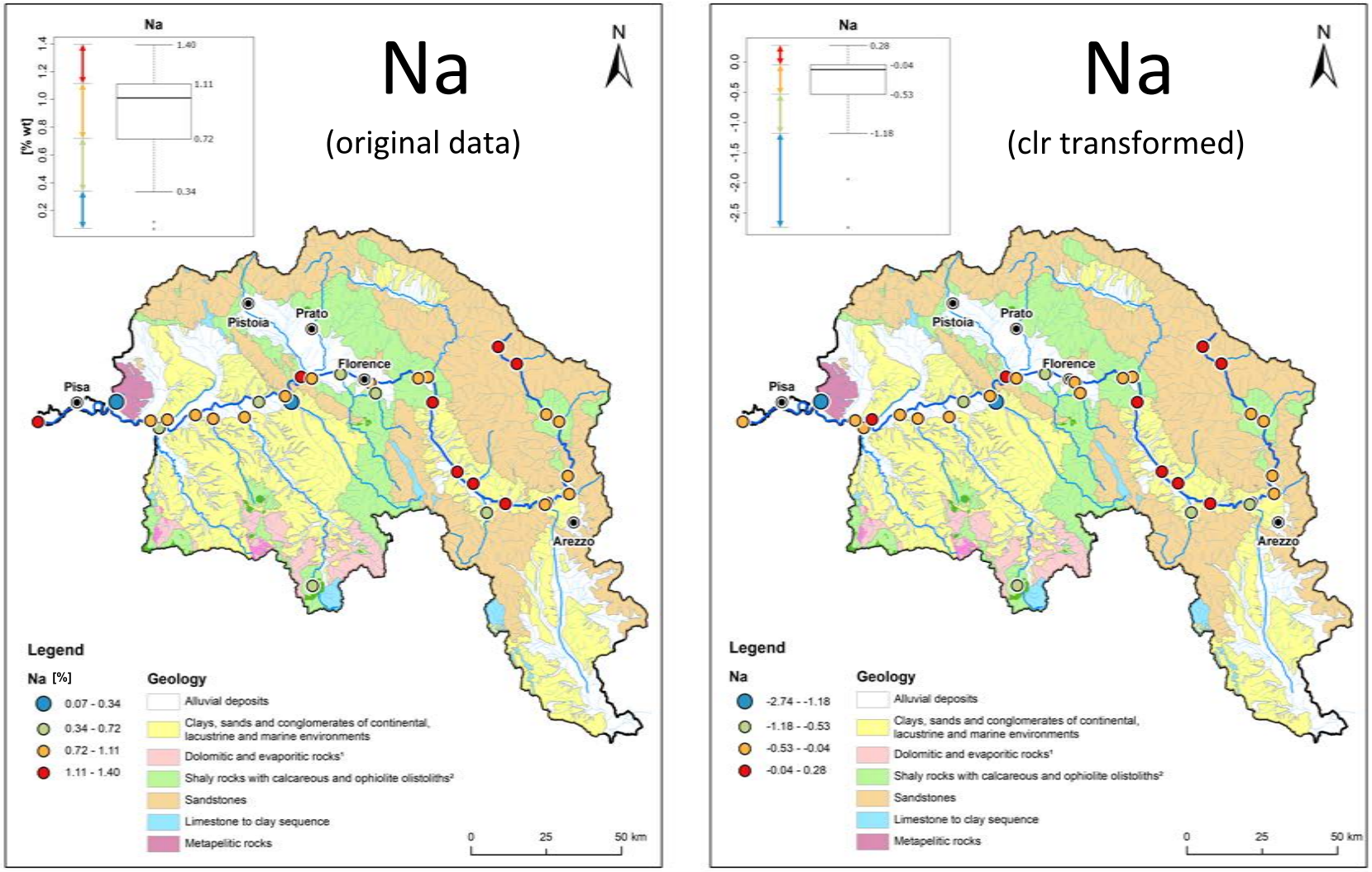

Figure 26 Distribution of the original data (left) and clr transformed data (right) of Na in stream sediments presented on a schematic lithological map modified after Carmignani et al. (2013).

[1]: Evaporites highlighted with a more saturated color. [2]: Ophiolites highlighted with a more saturated color.

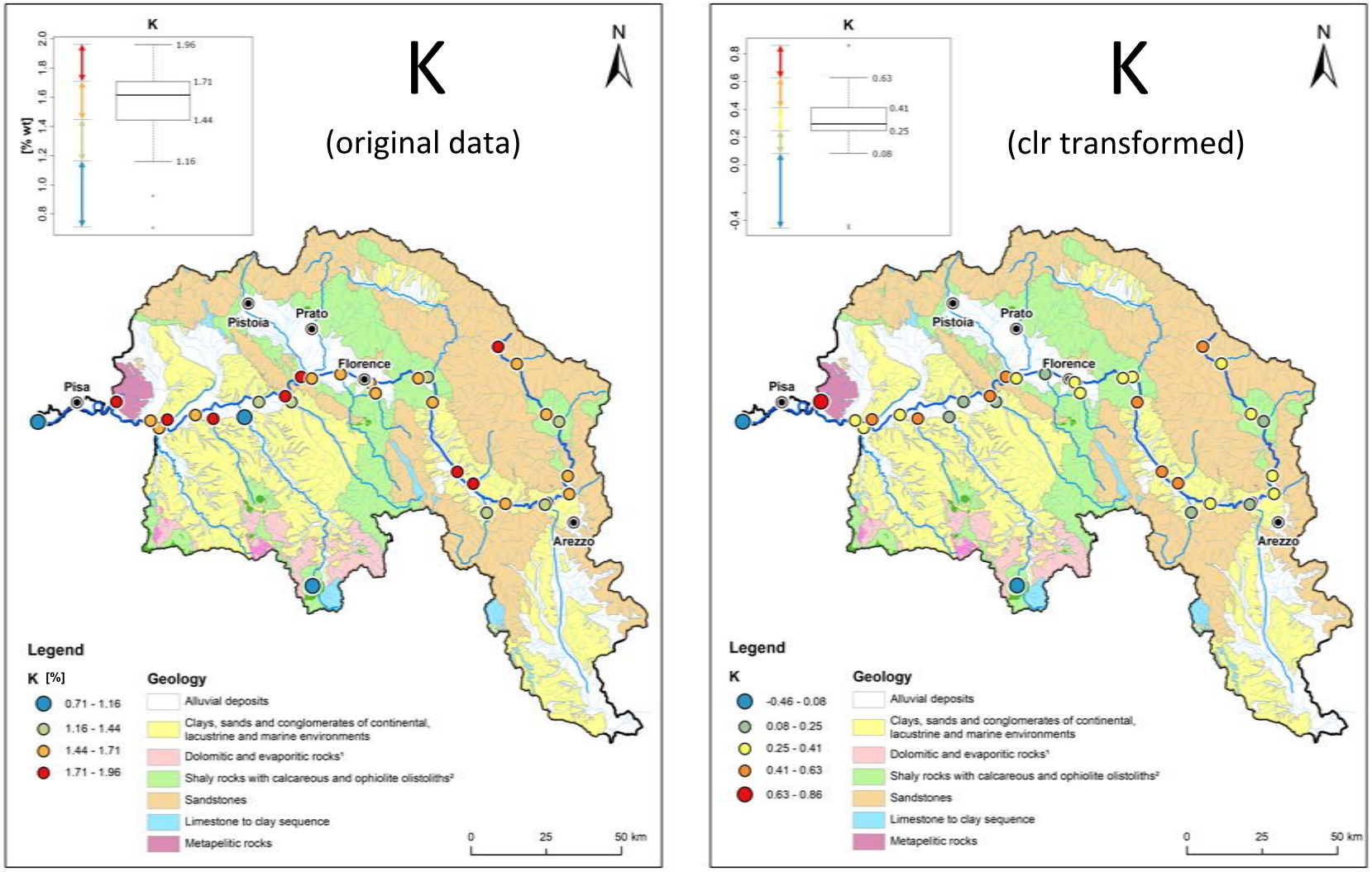

Figure 27 Distribution of the original data (left) and clr transformed data (right) of K in stream sediments presented on a schematic lithological map modified after Carmignani et al. (2013).

[1]: Evaporites highlighted with a more saturated color. [2]: Ophiolites highlighted with a more saturated color.

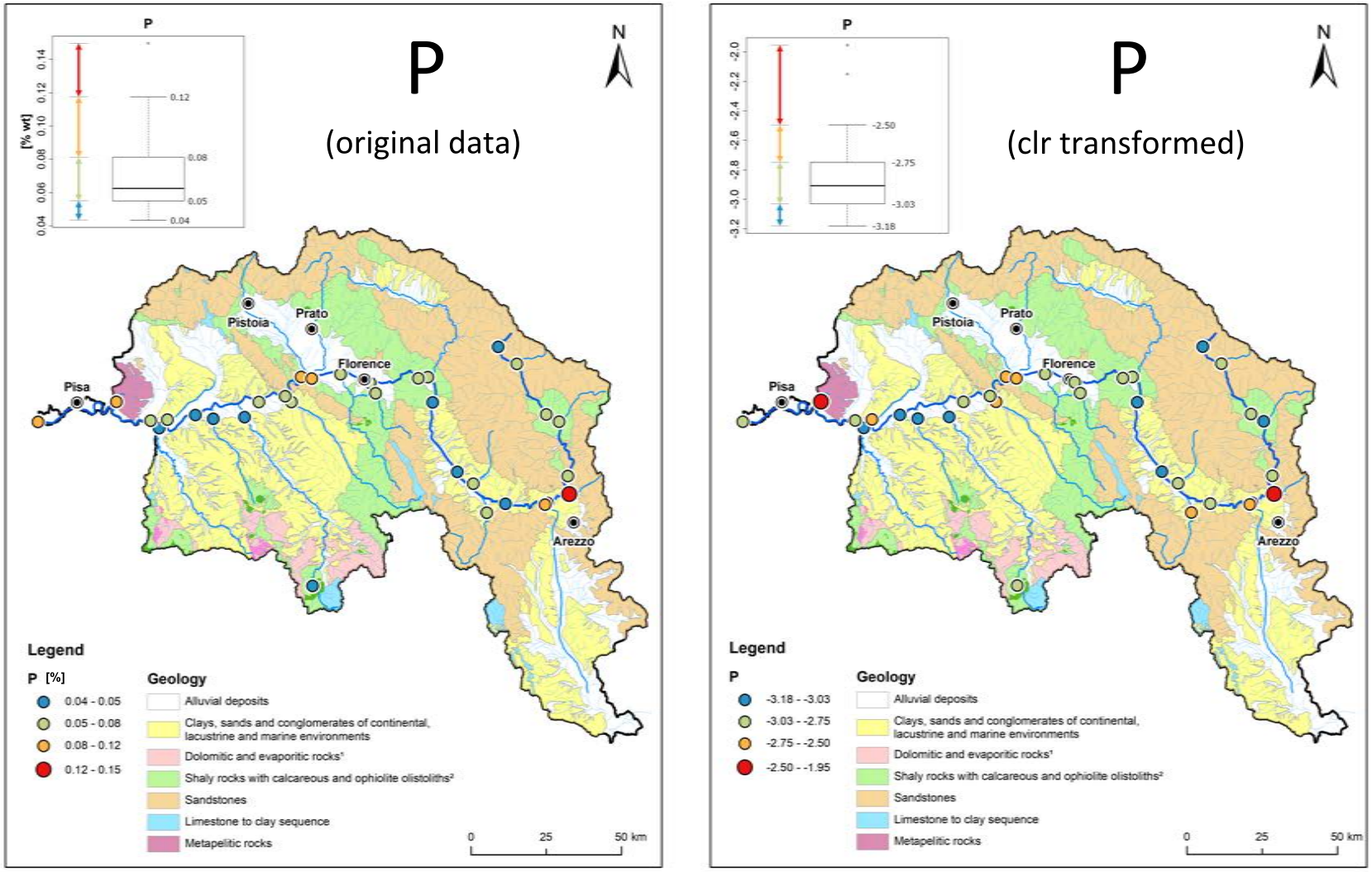

Figure 28 Distribution of the original data (left) and clr transformed data (right) of P in stream sediments presented on a schematic lithological map modified after Carmignani et al. (2013).

[1]: Evaporites highlighted with a more saturated color. [2]: Ophiolites highlighted with a more saturated color.

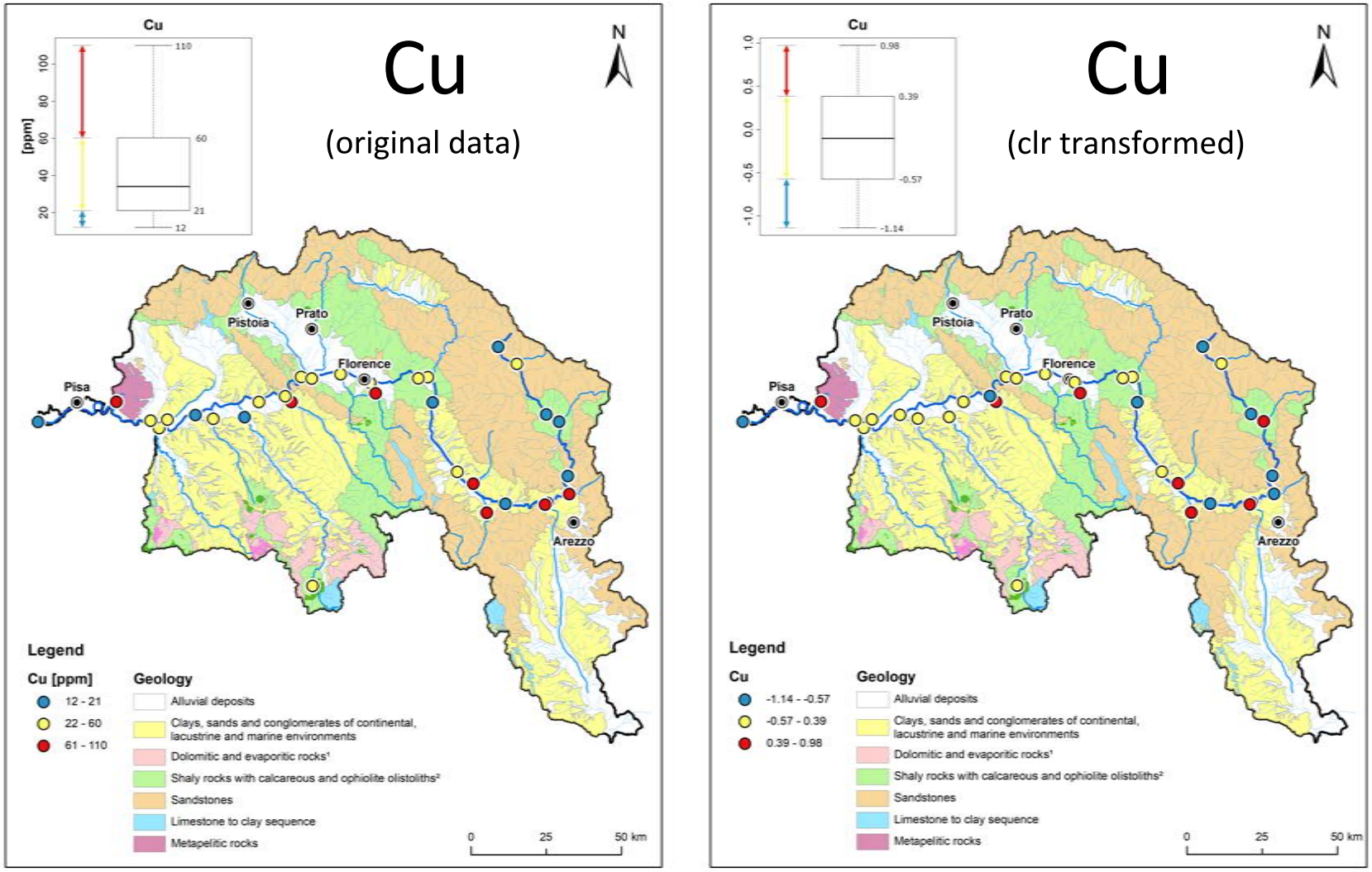

Figure 29 Distribution of the original data (left) and clr transformed data (right) of Cu in stream sediments presented on a schematic lithological map modified after Carmignani et al. (2013).

[1]: Evaporites highlighted with a more saturated color. [2]: Ophiolites highlighted with a more saturated color.

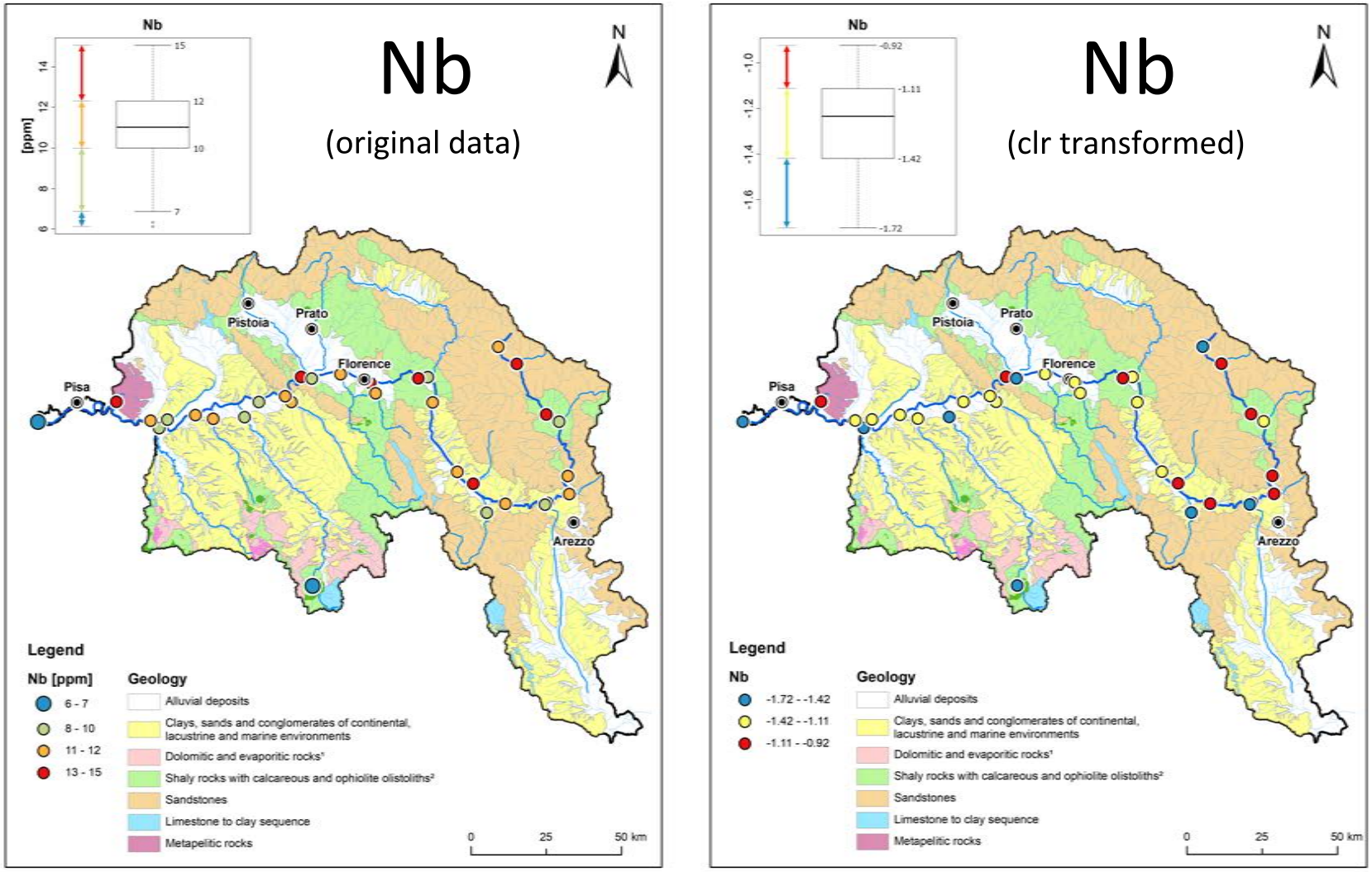

Figure 30 Distribution of the original data (left) and clr transformed data (right) of Nb in stream sediments presented on a schematic lithological map modified after Carmignani et al. (2013).

[1]: Evaporites highlighted with a more saturated color. [2]: Ophiolites highlighted with a more saturated color.

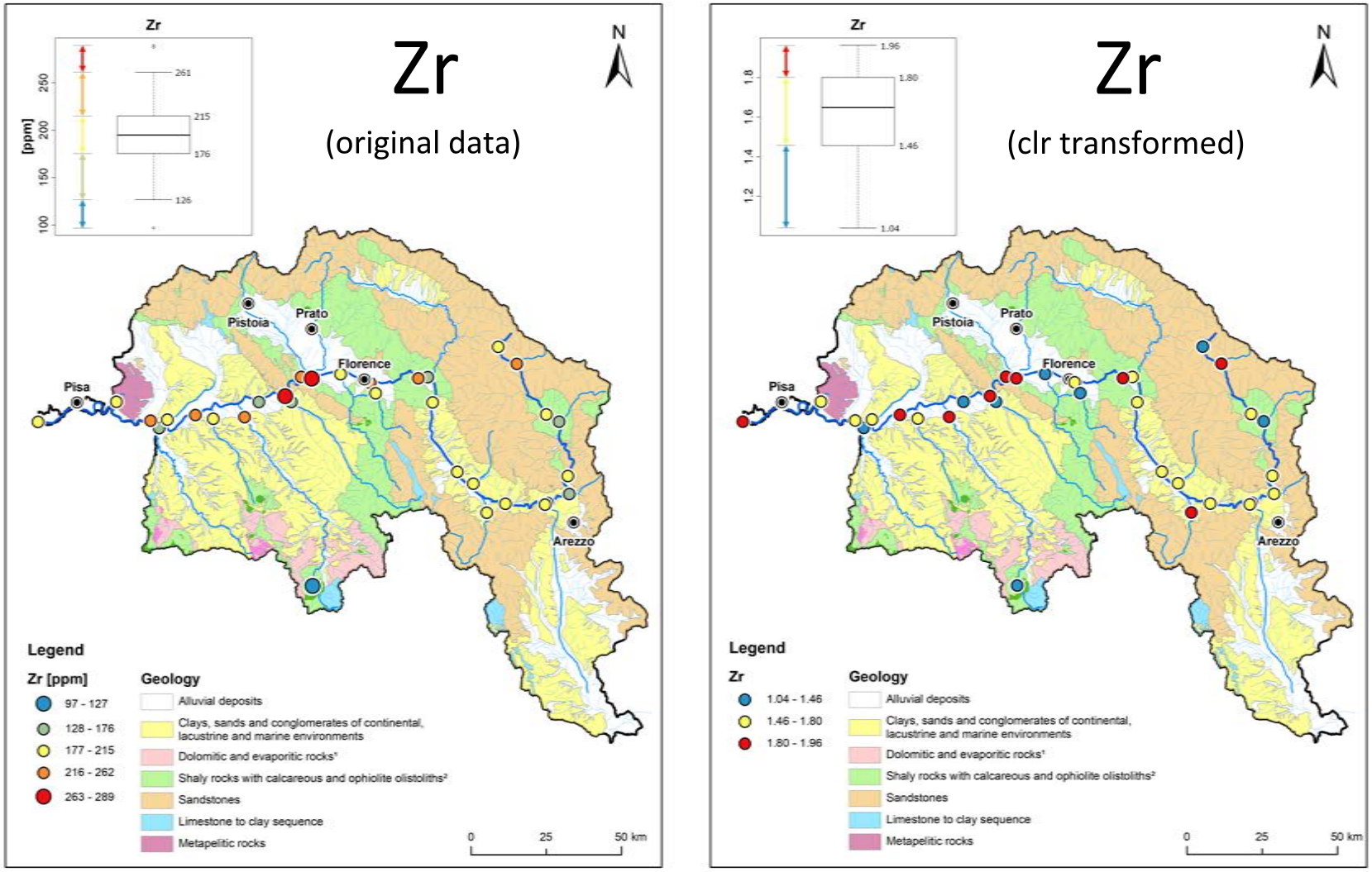

Figure 31 Distribution of the original data (left) and clr transformed data (right) of Zr in stream sediments presented on a schematic lithological map modified after Carmignani et al. (2013).

[1]: Evaporites highlighted with a more saturated color. [2]: Ophiolites highlighted with a more saturated color.

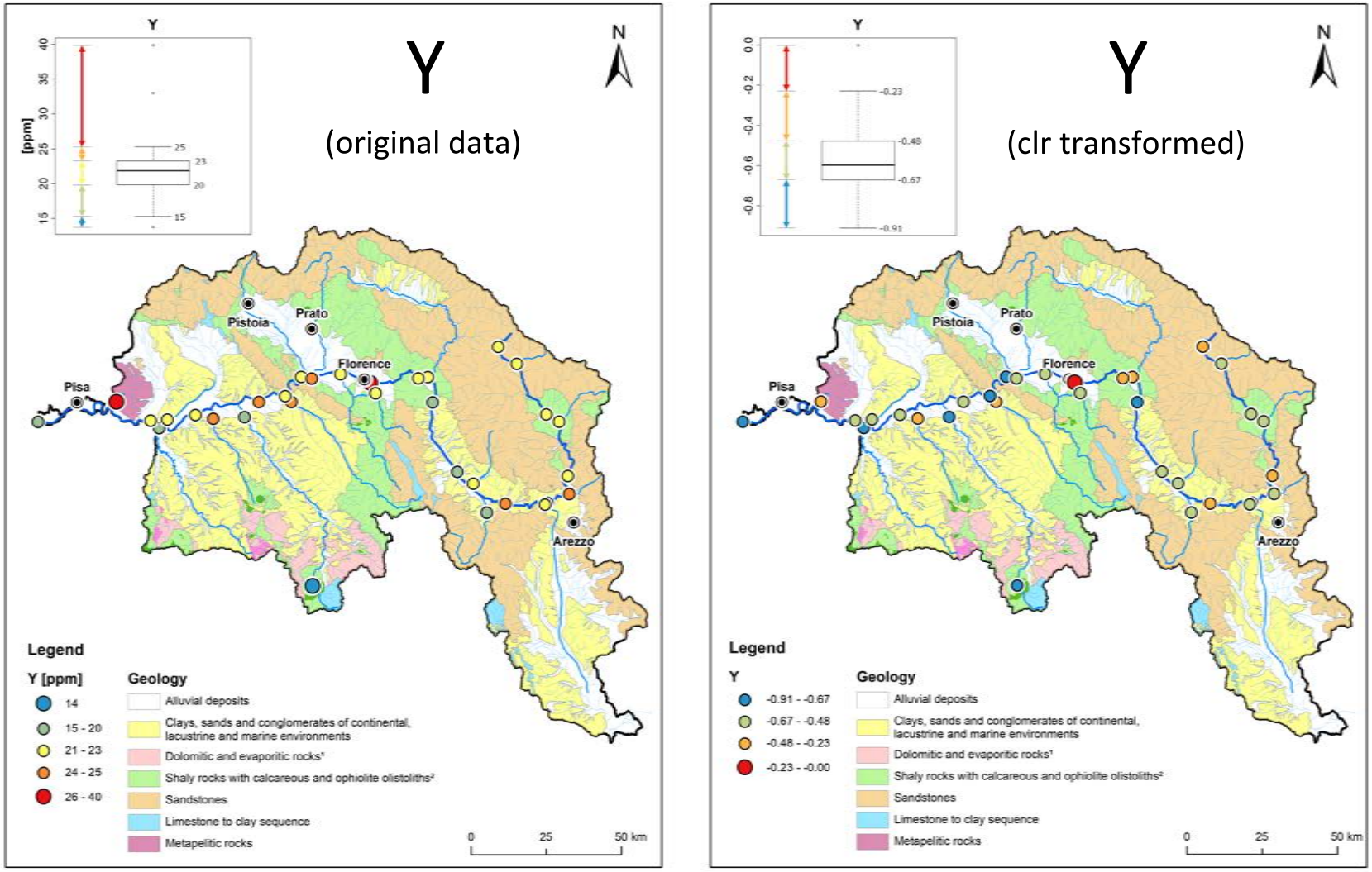

Figure 32 Distribution of the original data (left) and clr transformed data (right) of Y in stream sediments presented on a schematic lithological map modified after Carmignani et al. (2013).

[1]: Evaporites highlighted with a more saturated color. [2]: Ophiolites highlighted with a more saturated color.

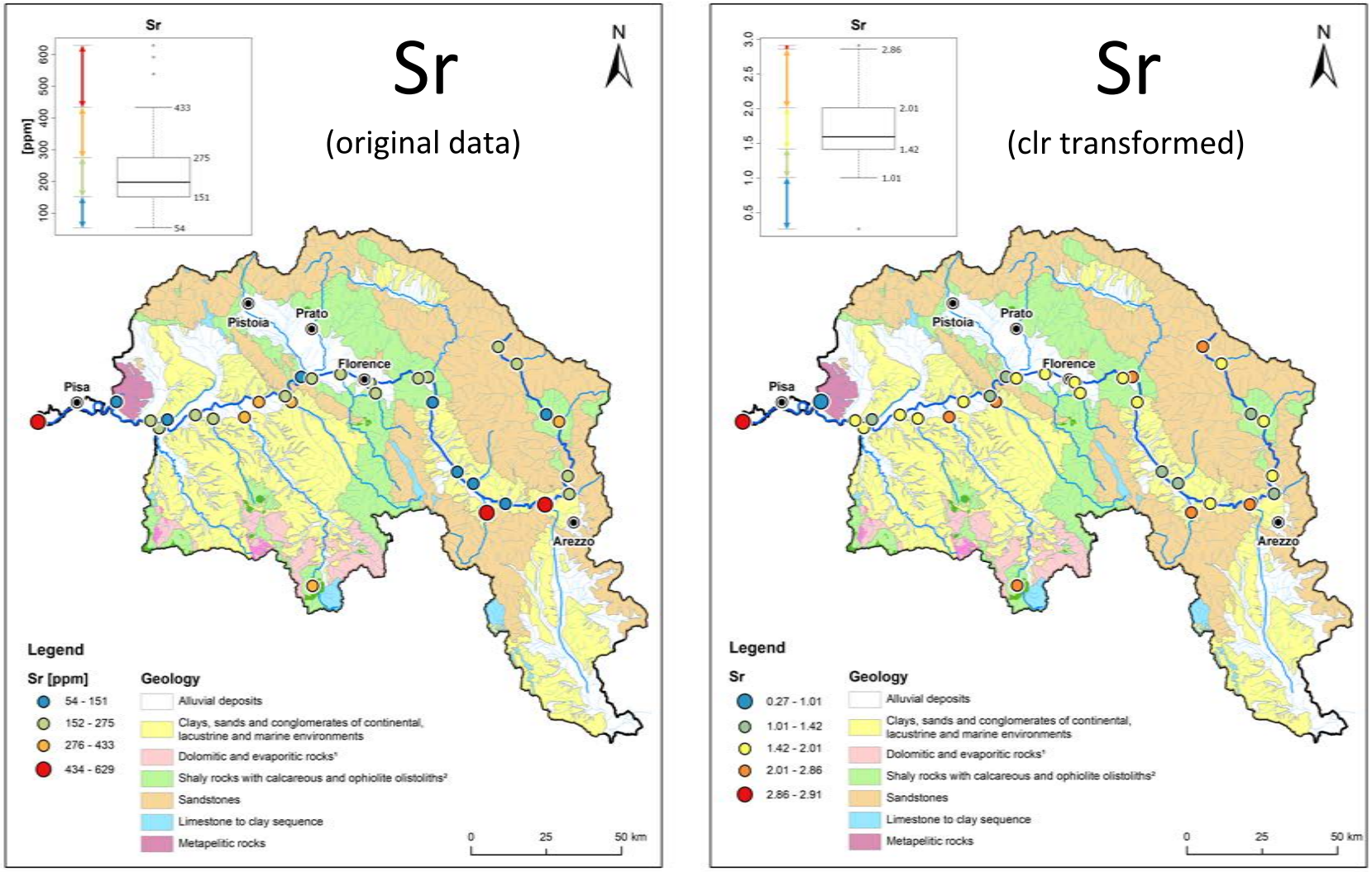

Figure 33 Distribution of the original data (left) and clr transformed data (right) of Sr in stream sediments presented on a schematic lithological map modified after Carmignani et al. (2013).

[1]: Evaporites highlighted with a more saturated color. [2]: Ophiolites highlighted with a more saturated color.

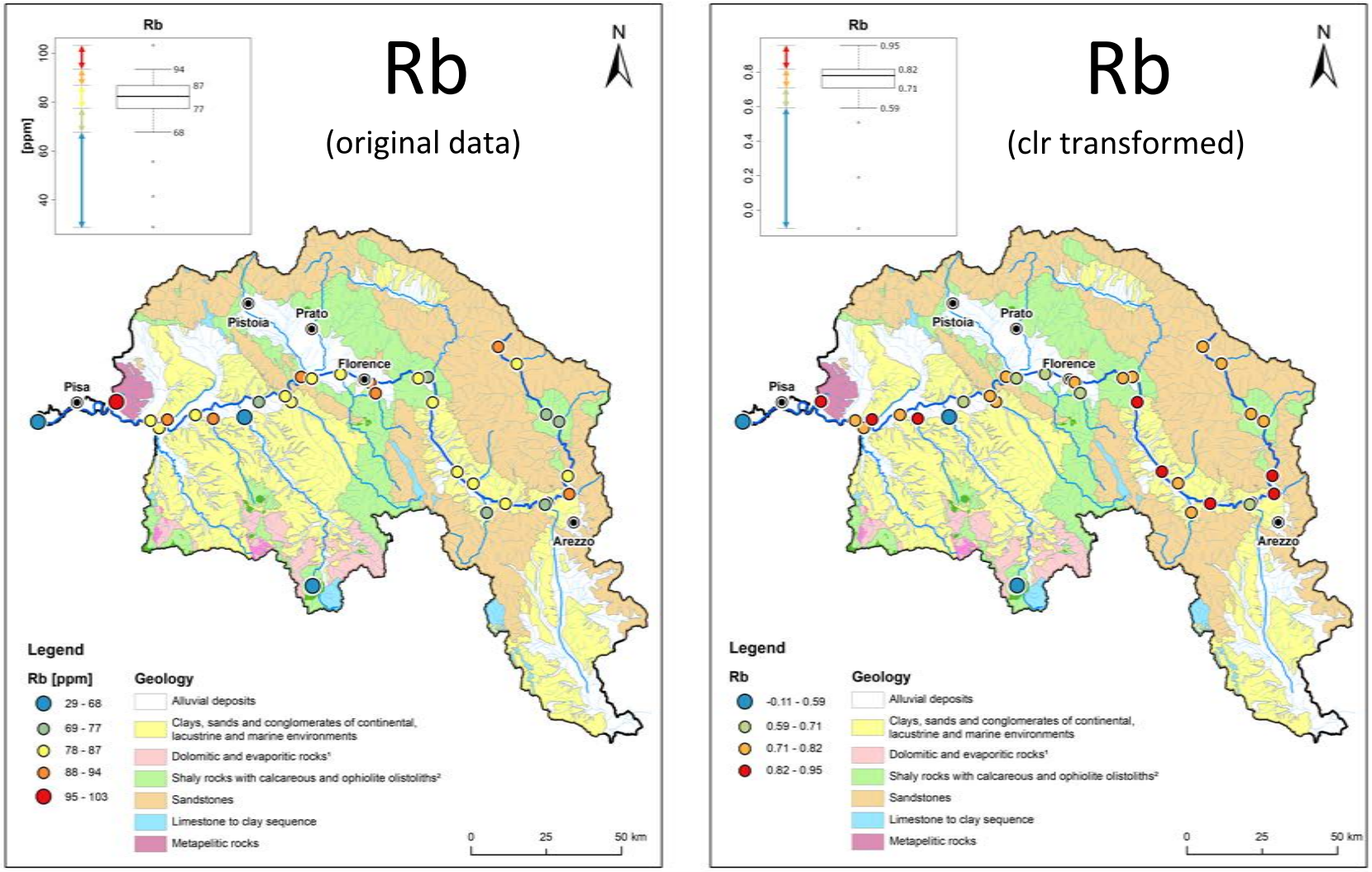

Figure 34 Distribution of the original data (left) and clr transformed data (right) of Rb in stream sediments presented on a schematic lithological map modified after Carmignani et al. (2013).

[1]: Evaporites highlighted with a more saturated color. [2]: Ophiolites highlighted with a more saturated color.

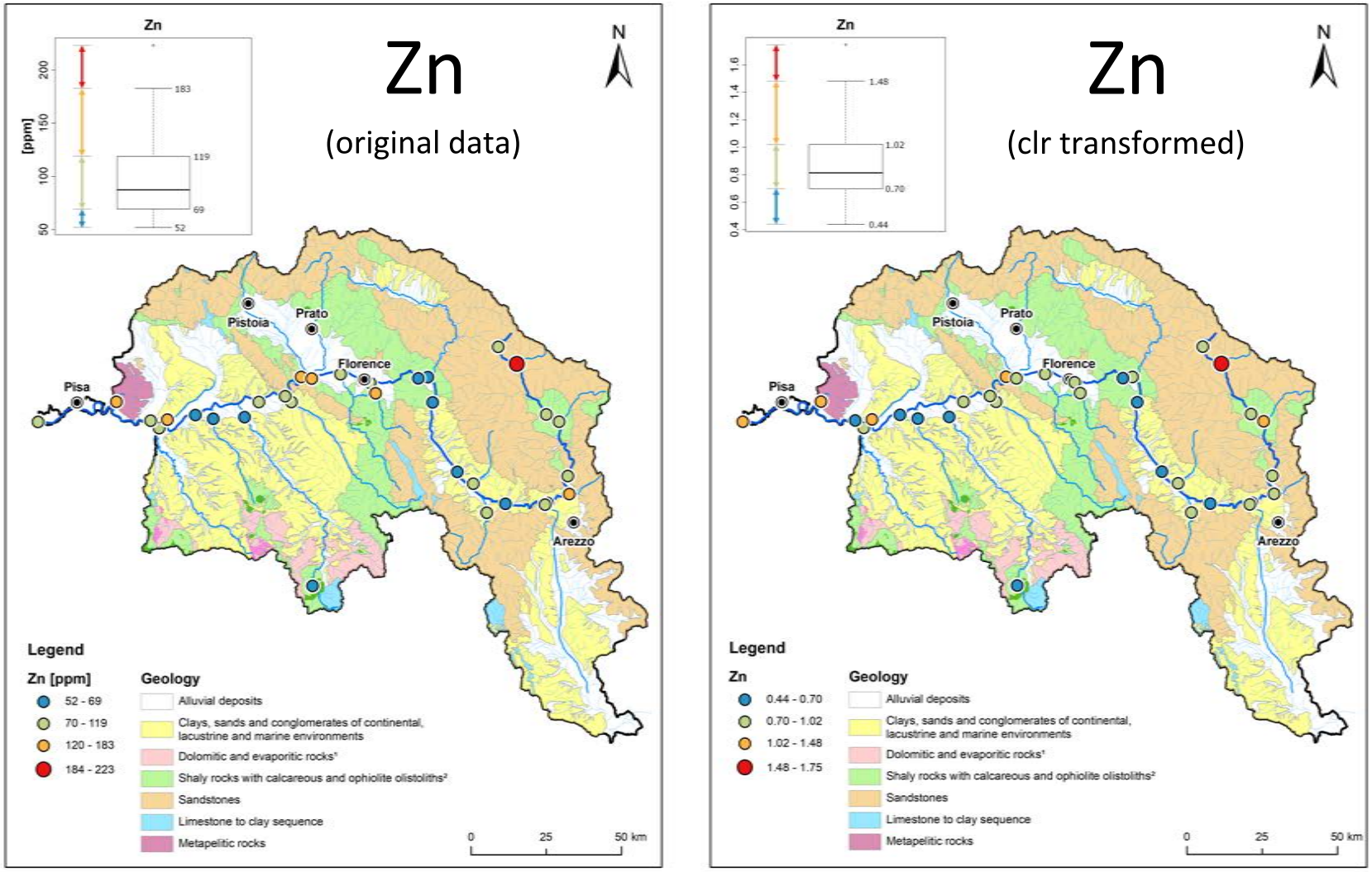

Figure 35 Distribution of the original data (left) and clr transformed data (right) of Zn in stream sediments presented on a schematic lithological map modified after Carmignani et al. (2013).

[1]: Evaporites highlighted with a more saturated color. [2]: Ophiolites highlighted with a more saturated color.

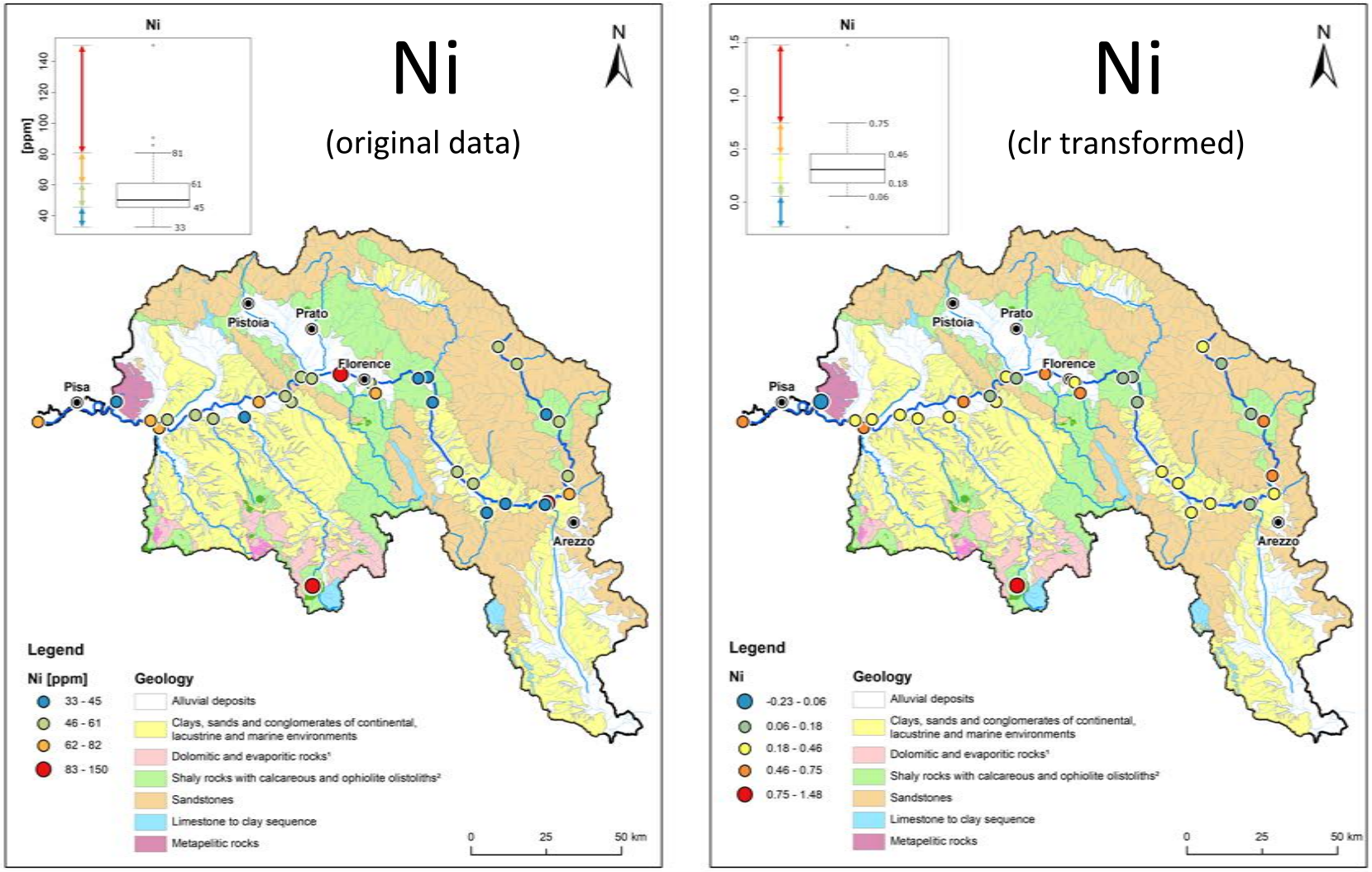

Figure 36 Distribution of the original data (left) and clr transformed data (right) of Ni in stream sediments presented on a schematic lithological map modified after Carmignani et al. (2013).

[1]: Evaporites highlighted with a more saturated color. [2]: Ophiolites highlighted with a more saturated color.

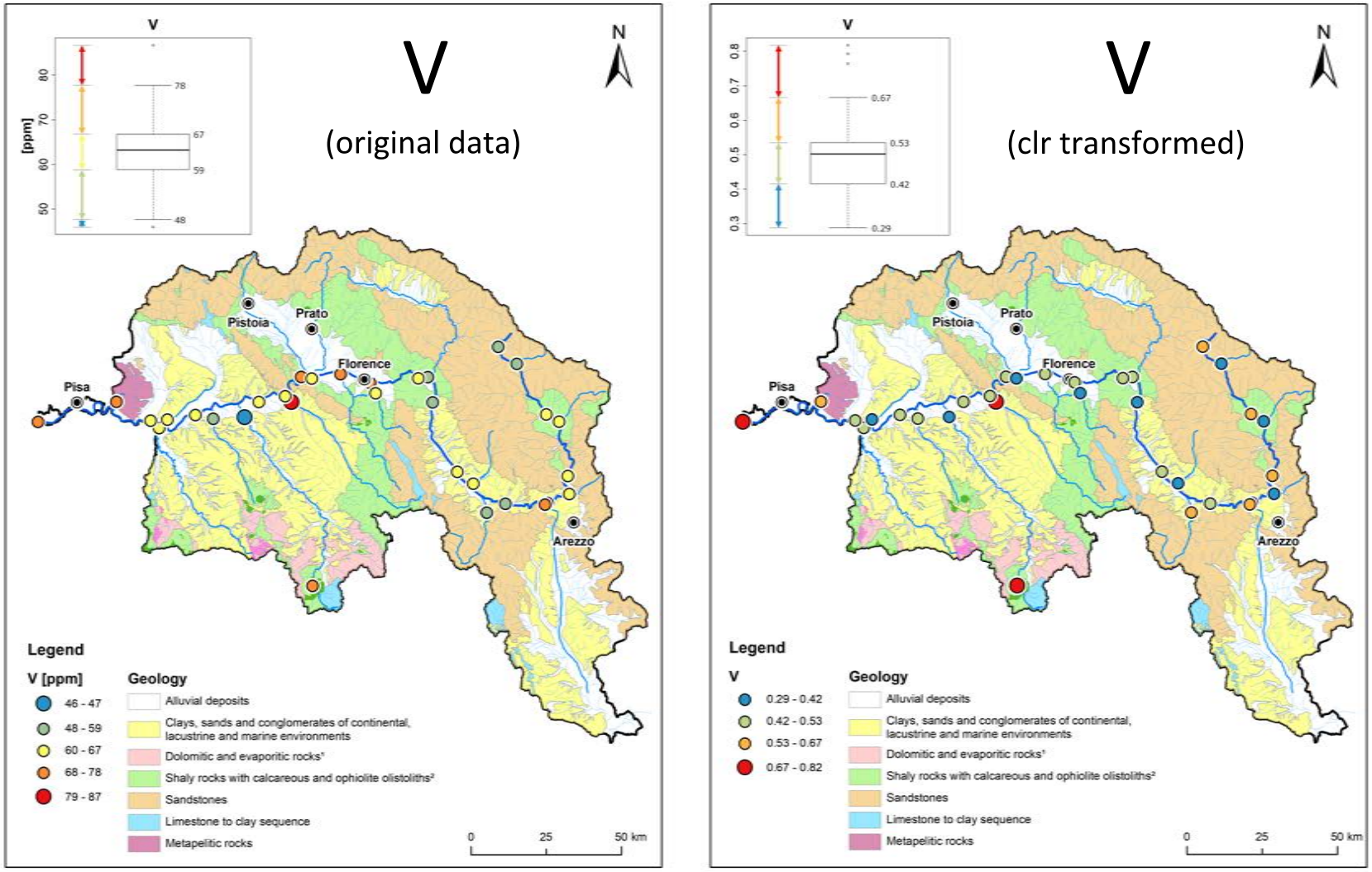

Figure 37 Distribution of the original data (left) and clr transformed data (right) of V in stream sediments presented on a schematic lithological map modified after Carmignani et al. (2013).

[1]: Evaporites highlighted with a more saturated color. [2]: Ophiolites highlighted with a more saturated color.

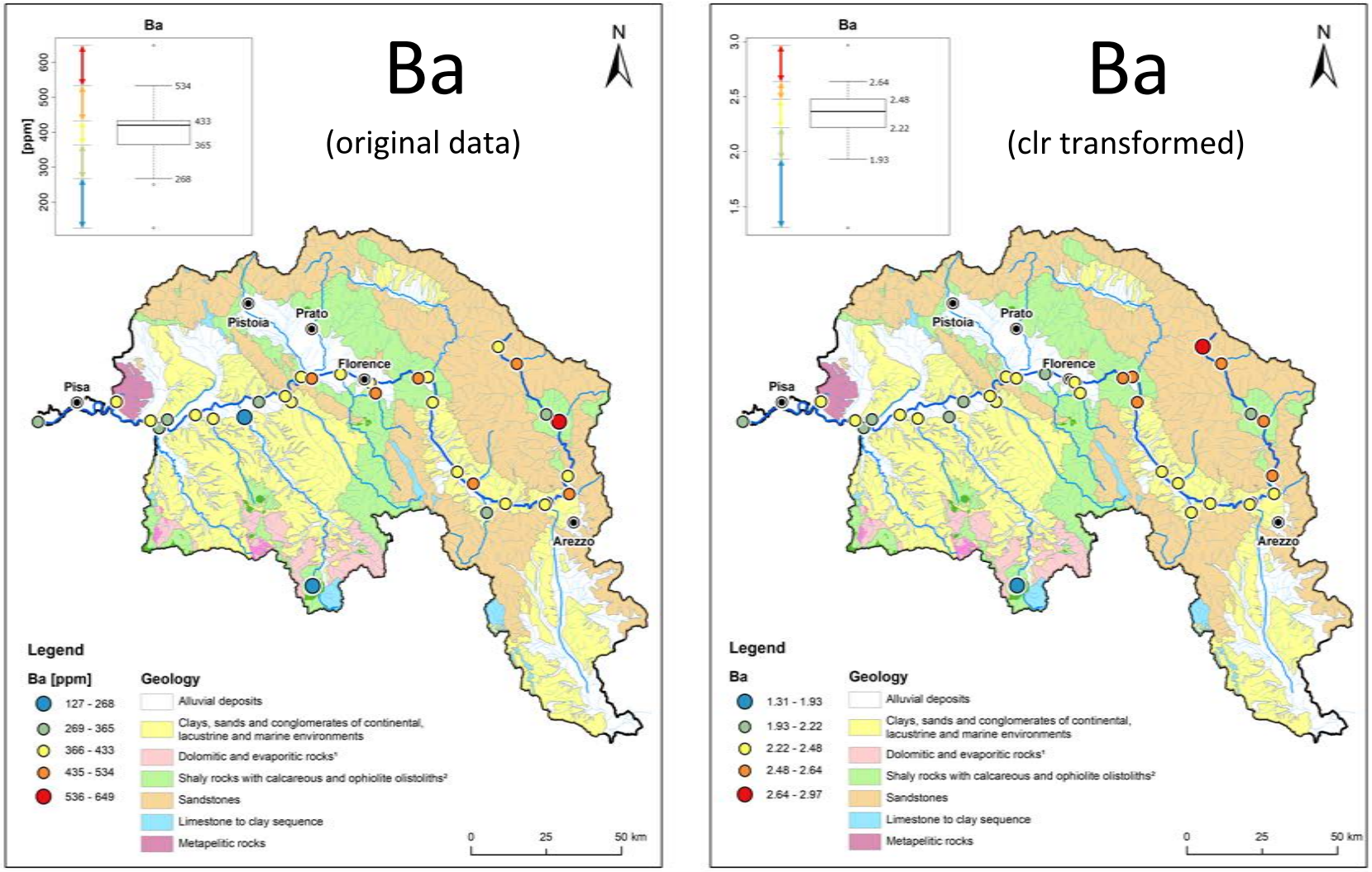

Figure 38 Distribution of the original data (left) and clr transformed data (right) of Ba in stream sediments presented on a schematic lithological map modified after Carmignani et al. (2013).

[1]: Evaporites highlighted with a more saturated color. [2]: Ophiolites highlighted with a more saturated color.

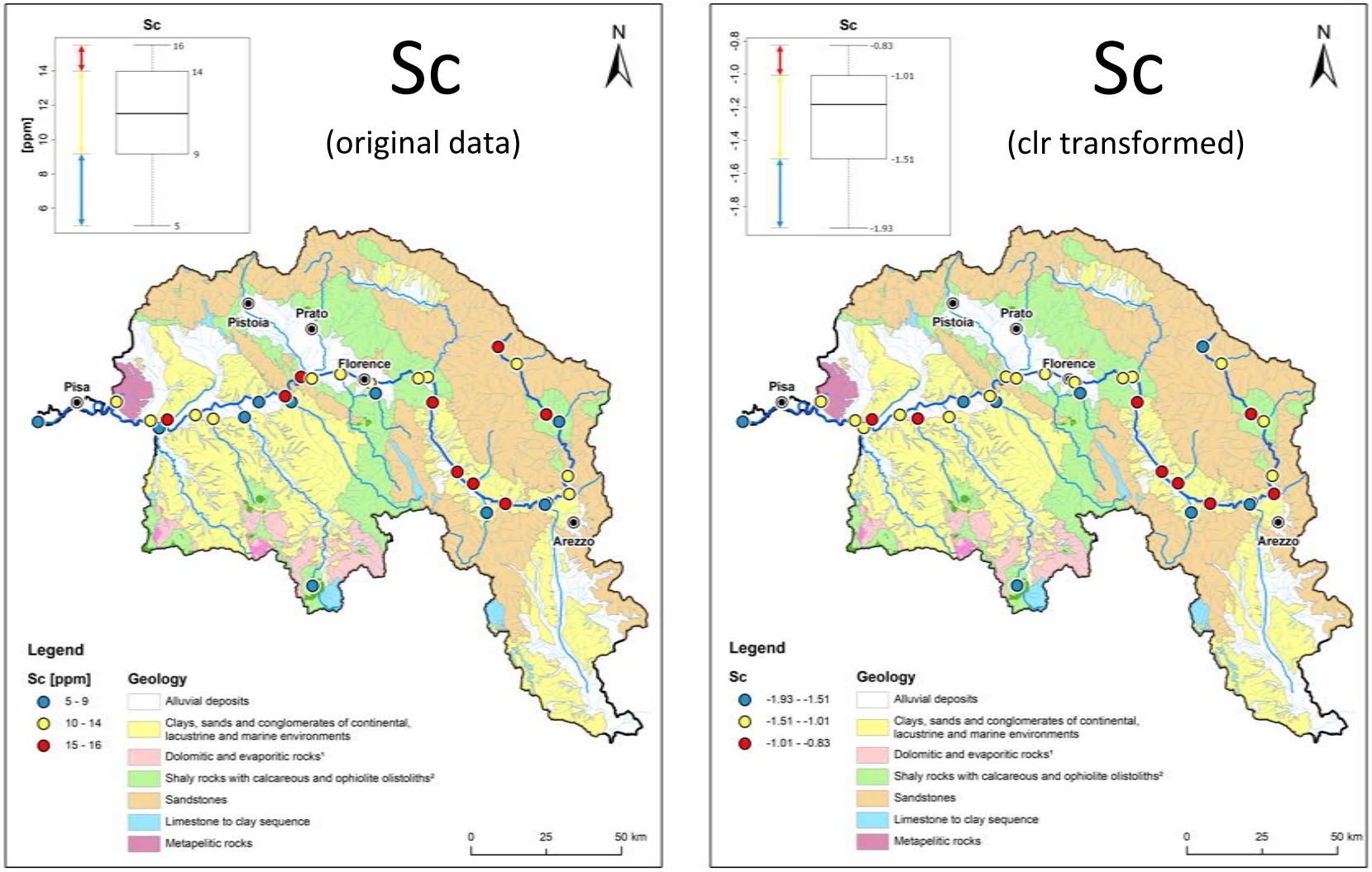

Figure 39 Distribution of the original data (left) and clr transformed data (right) of Sc in stream sediments presented on a schematic lithological map modified after Carmignani et al. (2013).

[1]: Evaporites highlighted with a more saturated color. [2]: Ophiolites highlighted with a more saturated color.

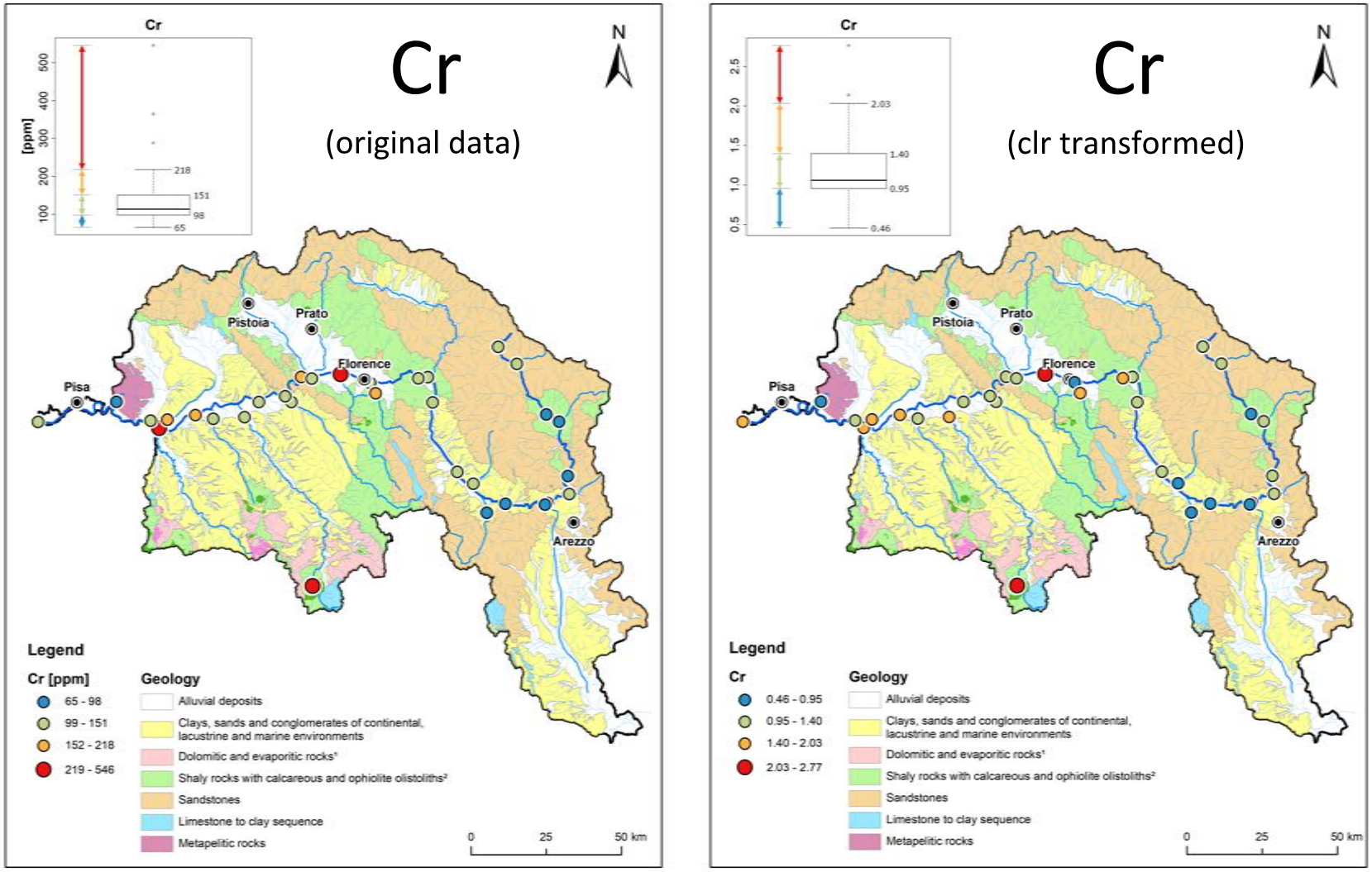

Figure 40 Distribution of the original data (left) and clr transformed data (right) of Cr in stream sediments presented on a schematic lithological map modified after Carmignani et al. (2013).

[1]: Evaporites highlighted with a more saturated color. [2]: Ophiolites highlighted with a more saturated color.

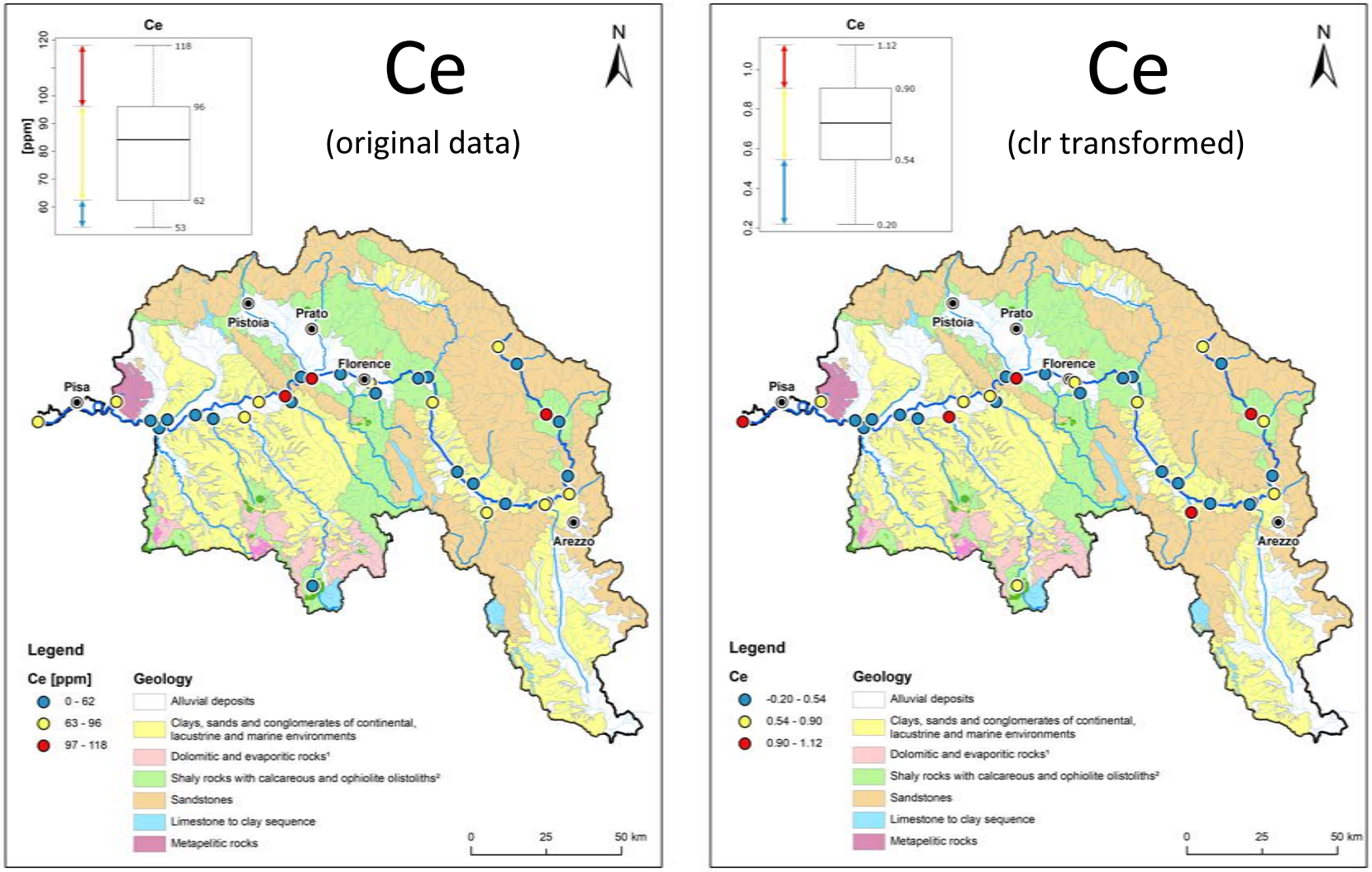

Figure 41 Distribution of the original data (left) and clr transformed data (right) of Ce in stream sediments presented on a schematic lithological map modified after Carmignani et al. (2013).

[1]: Evaporites highlighted with a more saturated color. [2]: Ophiolites highlighted with a more saturated color.

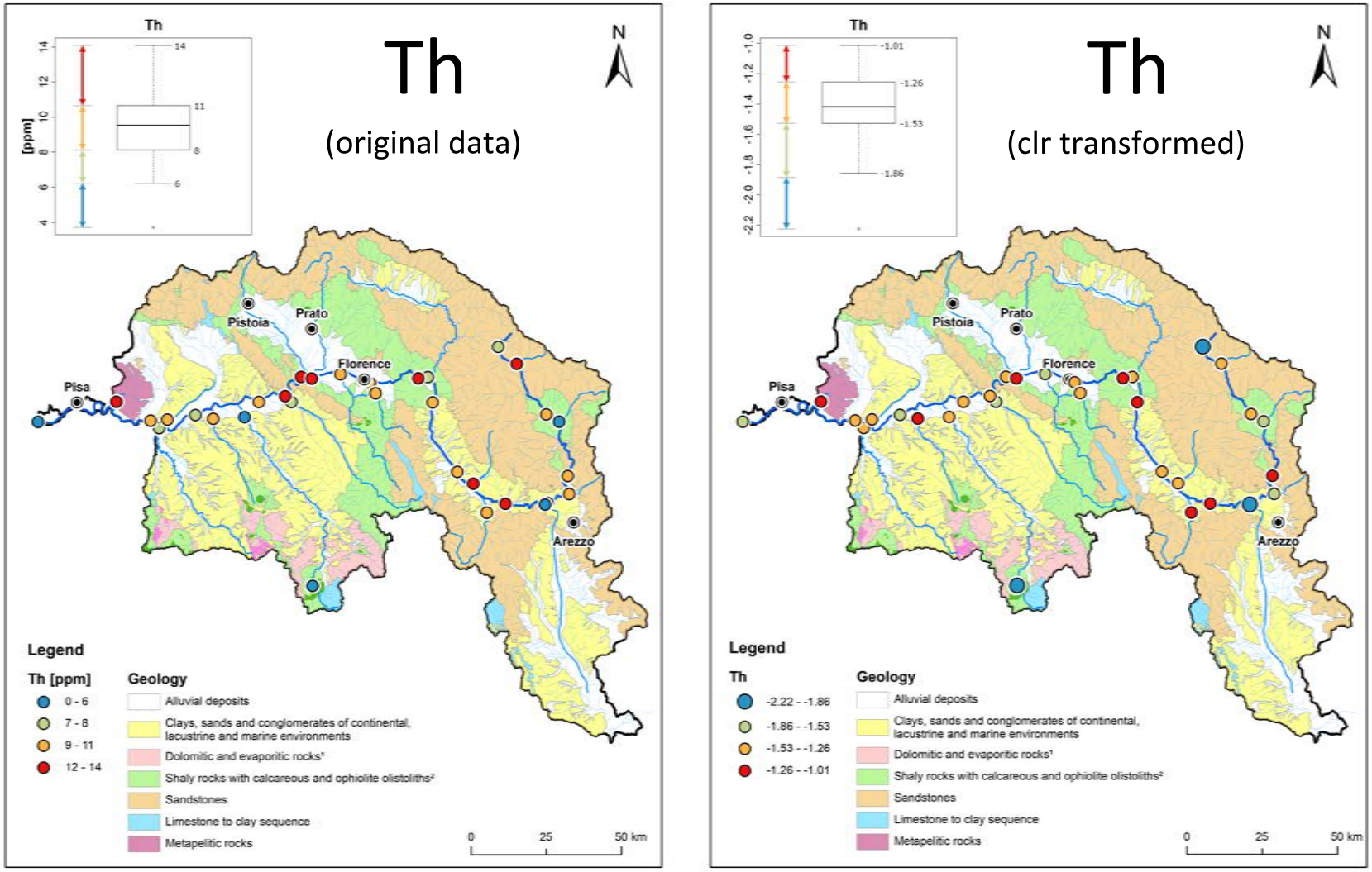

Figure 42 Distribution of the original data (left) and clr transformed data (right) of Th in stream sediments presented on a schematic lithological map modified after Carmignani et al. (2013).

[1]: Evaporites highlighted with a more saturated color. [2]: Ophiolites highlighted with a more saturated color.

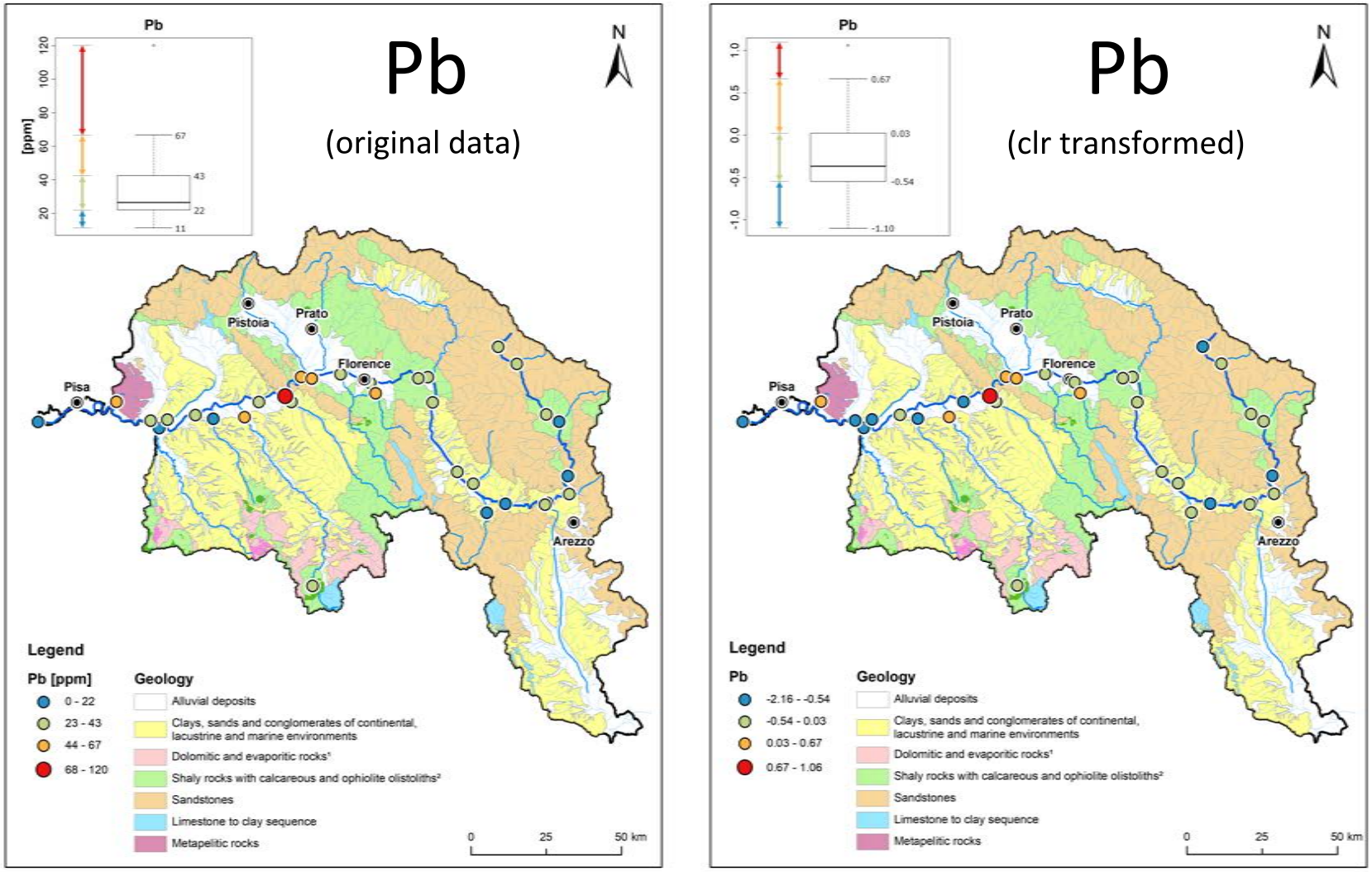

Figure 43 Distribution of the original data (left) and clr transformed data (right) of Pb in stream sediments presented on a schematic lithological map modified after Carmignani et al. (2013).

[1]: Evaporites highlighted with a more saturated color. [2]: Ophiolites highlighted with a more saturated color.

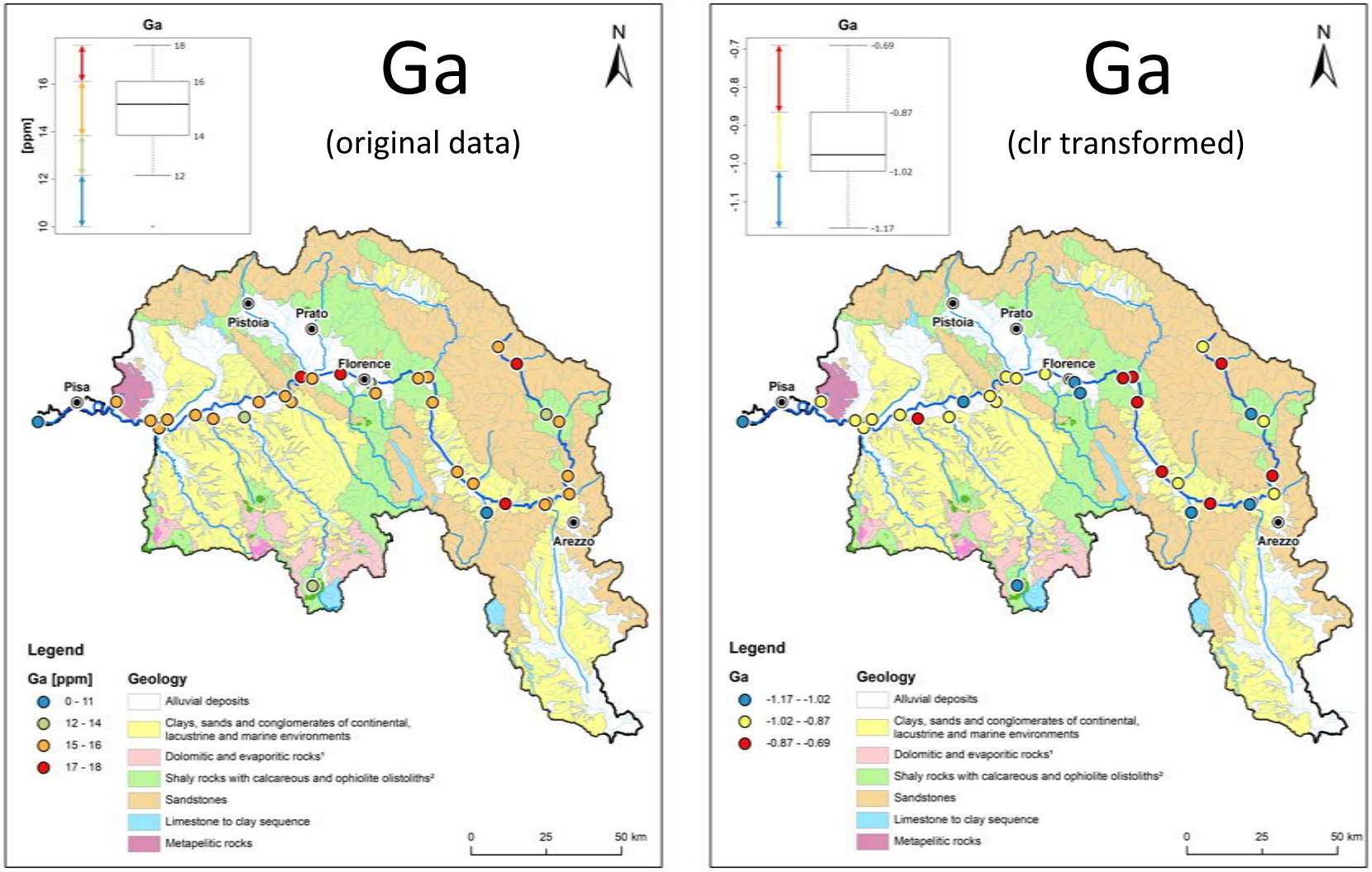

Figure 44 Distribution of the original data (left) and clr transformed data (right) of Ga in stream sediments presented on a schematic lithological map modified after Carmignani et al. (2013).

[1]: Evaporites highlighted with a more saturated color. [2]: Ophiolites highlighted with a more saturated color.

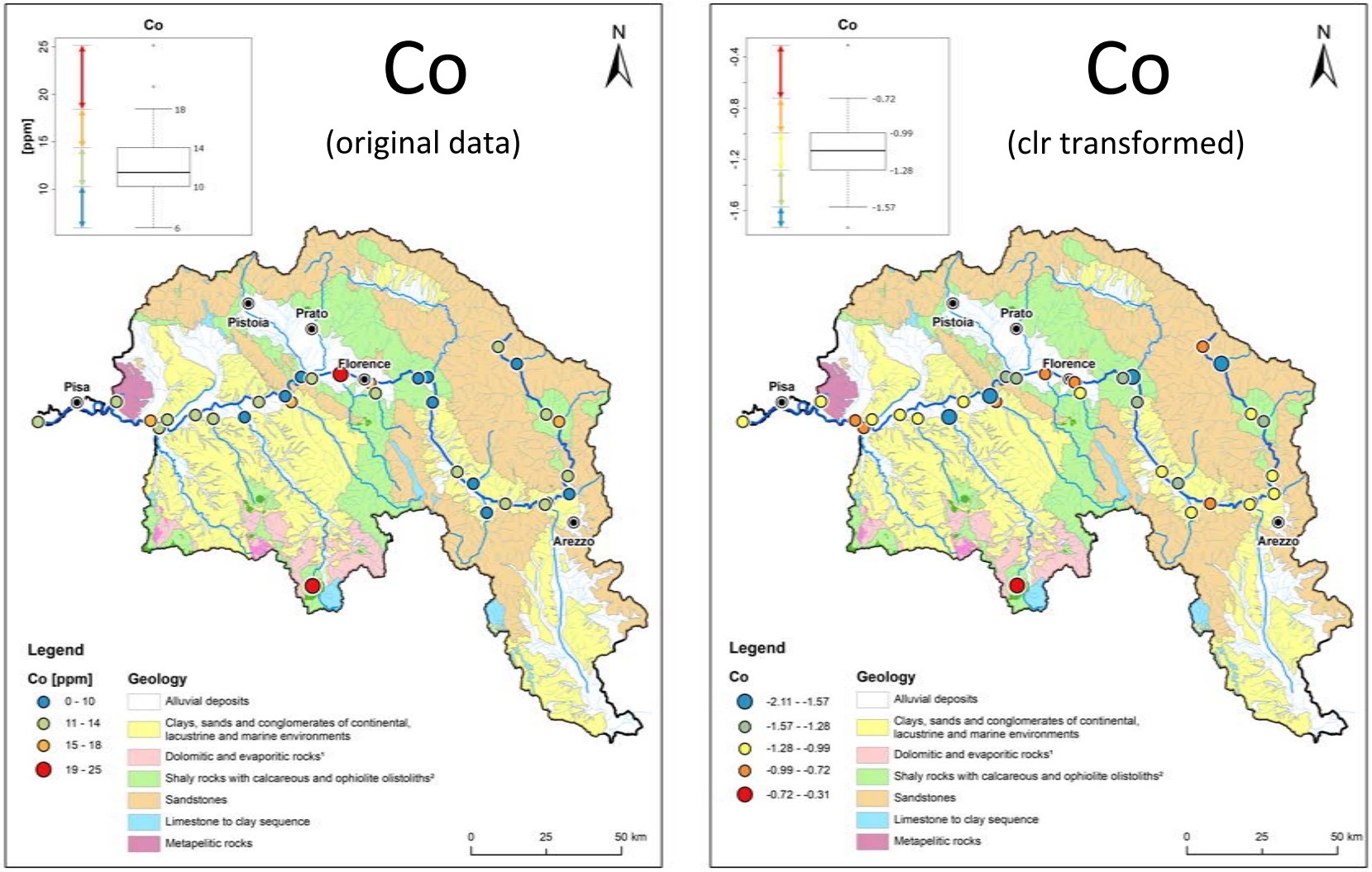

Figure 45 Distribution of the original data (left) and clr transformed data (right) of Co in stream sediments presented on a schematic lithological map modified after Carmignani et al. (2013).

[1]: Evaporites highlighted with a more saturated color. [2]: Ophiolites highlighted with a more saturated color.

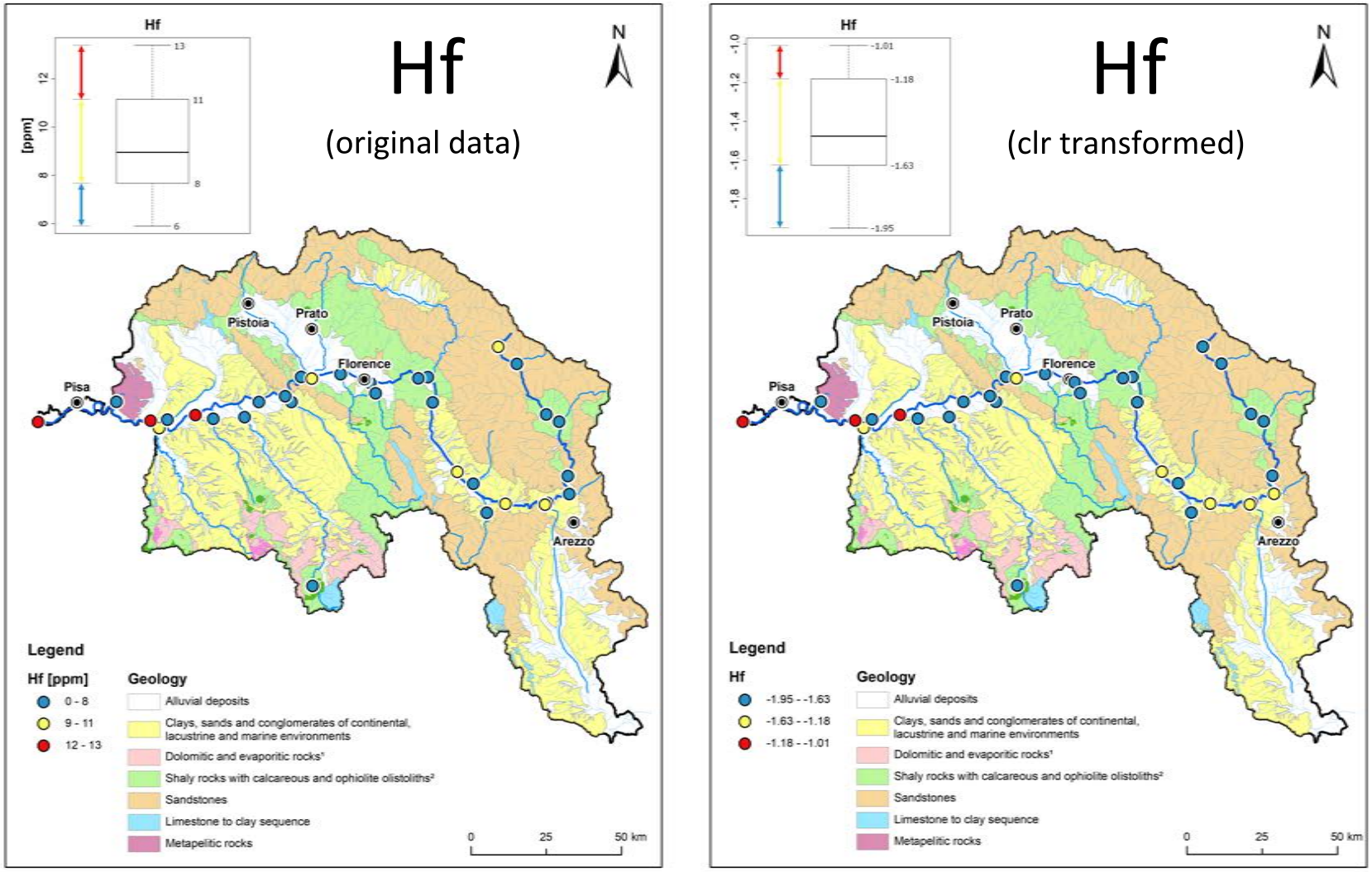

Figure 46 Distribution of the original data (left) and clr transformed data (right) of Hf in stream sediments presented on a schematic lithological map modified after Carmignani et al. (2013).

[1]: Evaporites highlighted with a more saturated color. [2]: Ophiolites highlighted with a more saturated color.

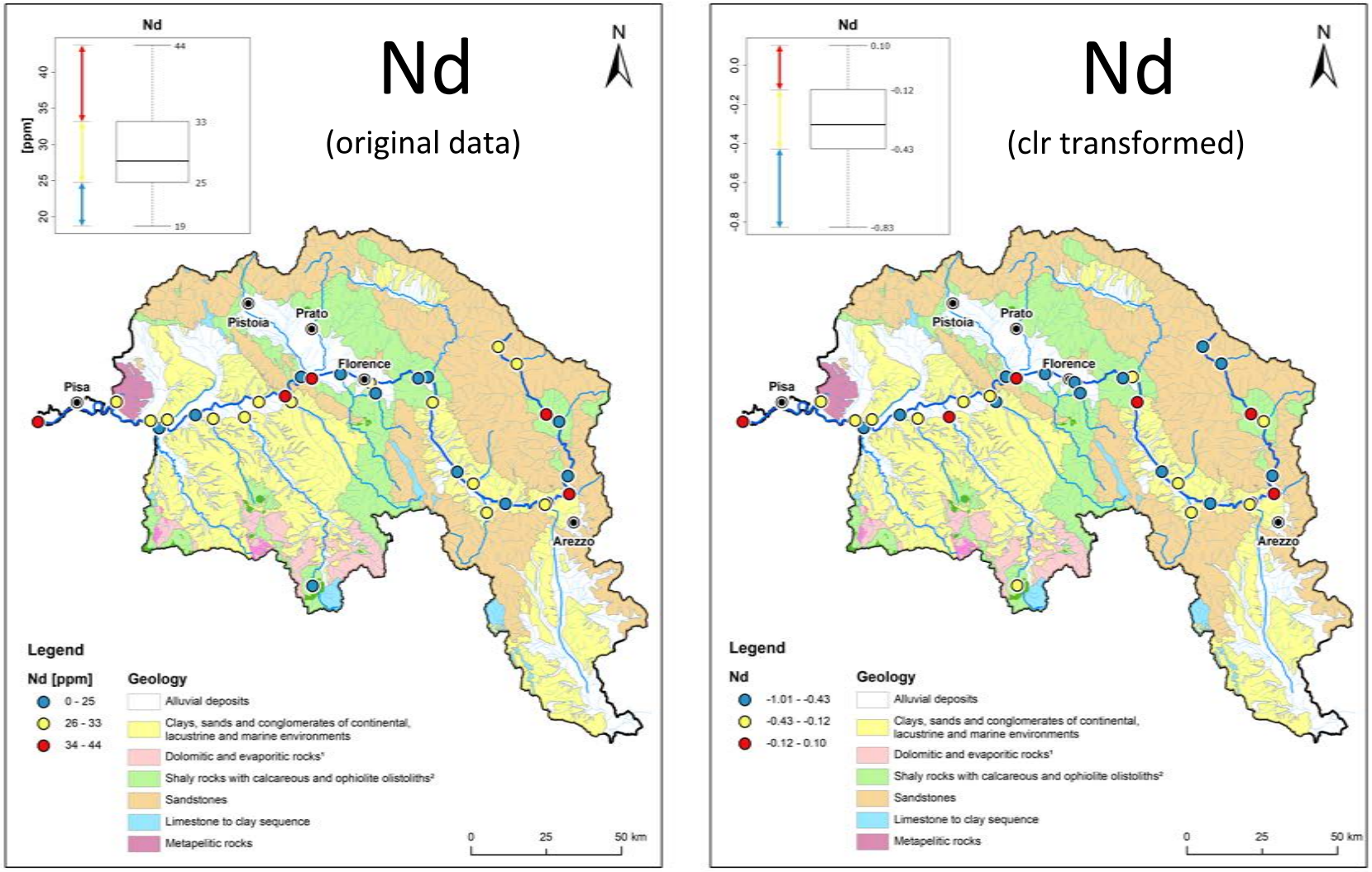

Figure 47 Distribution of the original data (left) and clr transformed data (right) of Nd in stream sediments presented on a schematic lithological map modified after Carmignani et al. (2013).

[1]: Evaporites highlighted with a more saturated color. [2]: Ophiolites highlighted with a more saturated color.

Appendix C

R Scripts

C.1 Correlation Analysis

The used script was created by Peter Filzmoser (2017).

```r
plotmatrix <- function(X,method="spearman",which="heatmap",cluster=TRUE,ind=NU
LL,
title=paste(method,"correlation"),...){



# Peter Filzmoser, Nov 14, 2017
# PURPOSE: plot heatmaps or scatterplot matrix based on symmetric coordinates
:
# X ... compositional data set
# method: all those which are supported by "cor"
# which ... either "heatmap" or "scatterplot"
# cluster ... if TRUE, the heatmap will be clustered
# "..." ... further plot arguments for scatterplot


require(robCompositions)
  require(gplots)
  D <- ncol(X)

#op <- par()
par(mfrow = c(D, D), mar = c(0.1,0.1,0.1,0.1))
R <- matrix(NA, ncol = D, nrow = D)
nam <- names(X)
dimnames(R) <- list(nam, nam)
diag(R) <- rep(1, D)
for (i in 1:D){
  for (j in 1:D){
    if (i==j){
      if (which=="scatterplot"){
        plot(0, 0, type = "n", xaxt = "n", yaxt = "n")
        text(0, 0, nam[i])
       }
    }
    else{
      Z <- pivotCoord(X[, c(i, j, (1:D)[-c(i, j)])], method = "symm")
      if (which=="scatterplot"){
        plot(Z[, 1:2],xaxt = "n", yaxt = "n", xlab = "", ylab = "", ... )
      }
      R[i,j] <- cor(Z[, 1:2],method=method)[1, 2]
    }
  }
}
if (which=="heatmap"){
  rgbcol <- colorRampPalette(c("blue4","turquoise","white","orange","red4"),
             space = "rgb")
  if (is.null(ind)){
    res <- heatmap.2(as.matrix(R), Rowv = cluster, symm = TRUE, col = rgbcol(
256),
        key = TRUE, trace = "none", main = title, margins = c(4, 4), cexRow =
1.2, cexCol = 1.2)
```

```
  }
  else { # sort differently
    res <- heatmap.2(as.matrix(R)[rev(ind),ind], Rowv = FALSE, symm = TRUE, c
ol = rgbcol(256), dendrogram="none",
        key = TRUE, trace = "none", main = title, margins = c(4, 4), cexRow =
1.2, cexCol = 1.2)
  }
}
else if ((which!="heatmap") & (which!="scatterplot")){stop("Argument `which'
not correclty defined!")}
#par(op)
if (which=="scatterplot"){
  invisible()
}
else{
  list(R=R,rowInd=res$rowInd,colInd=res$colInd)
}
}


#Load data without sample name coloumn and La, Hf and Cs (everything that has
more than 60% <LDL) and Susc.
d<-as.data.frame(Arno_XRFdata)
plotmatrix(d, title="Spearman correlation ", cex=0.5)

write.table(plotmatrix(d, title="Spearman correlation", cex=0.5), file = "plo
tmatrix_Arno.txt", sep = "\t",
          row.names = TRUE, col.names = NA)
```

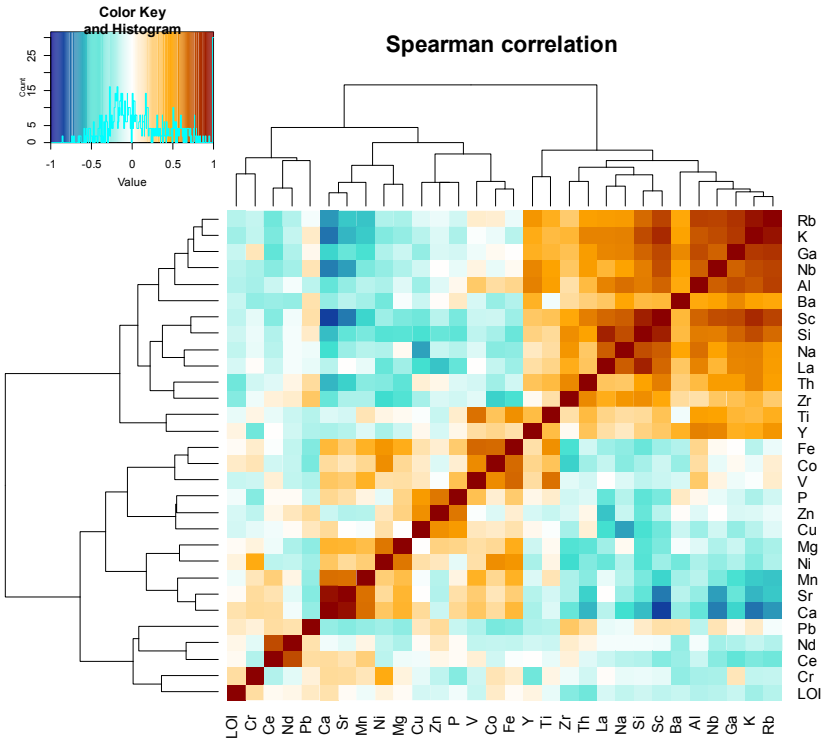

C.2 Robust Factor Analysis

The used script was created by Filzmoser et al. (2009b).

```r
Setwd(C:\PFA)

library(robustbase)
library(StatDA)
library(MASS)

# ilr transformation
ilr <- function(x){
  x.ilr=matrix(NA,nrow=nrow(x),ncol=ncol(x)-1)
  for (i in 1:ncol(x.ilr)){
    x.ilr[,i]=sqrt((i)/(i+1))*log(((apply(as.matrix(x[,1:i]), 1, prod))^(1/i)
)/(x[,i+1]))
  }
  return(x.ilr)
}

#data import
x <- read.table("data.txt", header = TRUE)

# construct orthonormal basis:
V=matrix(0,nrow=ncol(x),ncol=ncol(x)-1)
for (i in 1:ncol(V)){
  V[1:i,i] <- 1/i
  V[i+1,i] <- (-1)
  V[,i] <- V[,i]*sqrt(i/(i+1))
}

##############################log transformed PFA, n factors=4
#log transformation
set.seed(100)
x.mcd=covMcd(log10(x),cor=TRUE)

# classical scaling

# robust scaling
x.rsc=scale(log10(x),x.mcd$cent,sqrt(diag(x.mcd$cov)))


# robust PFA
res5R=pfa(x.rsc,factors=4,covmat=x.mcd,scores="regression",rotation="varimax"
)
rownames(res5R$loa)=rownames(res5$loa)

############################clr transformation PFA, n factors=4

z=ilr(x) #ilr transformed data
y=z%*%t(V) #clr transformed data

set.seed(200)
z.mcd=covMcd(z)
```

```
mean_z=z.mcd$center
mean_y=V%*%mean_z

var_z=z.mcd$cov
var_y=V%*%var_z%*%t(V)

y.rsc=scale(y,mean_y,scale=FALSE)

source("pfa1.R")
source("factanal.fit.principal1.R")

set.seed(200)
st=matrix(runif(16*200),nrow=16) # check data table


resRlogcentr=pfa1(y.rsc,factors=4,covmat=var_y,scores="Bartlett",rotation="va
rimax",start=st)
rownames(resRlogcentr$loa)=rownames(res5$loa)

####################loadings plots

#for clr transformed data
loadplot(resRlogcentr,titlepl="Robust FA (clr-transformed)", crit=0.3)
```

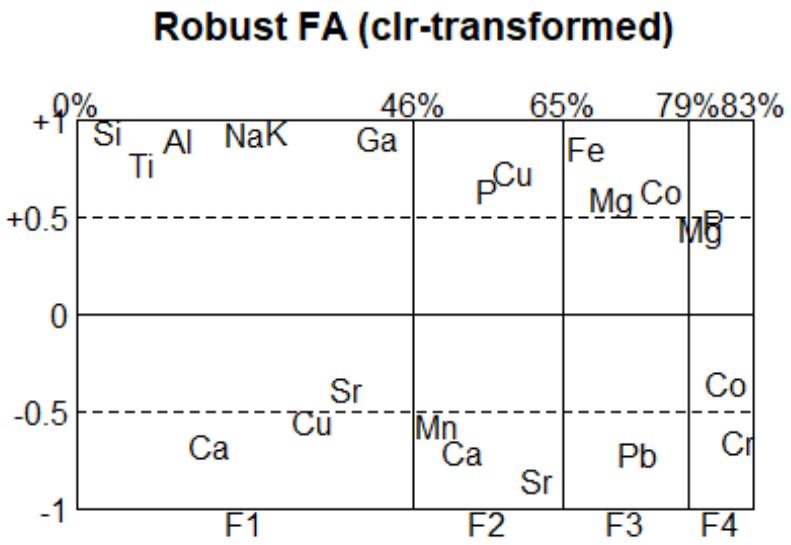


```
write.table(resRlogcentr$scores, file="scores.txt")
write.table(resRlogcentr$loadings, file="loadings.txt")
```

C.3 Robust Mahalanobis Distances

The used script was created by Caterina Gozzi.

```r
#data set import
library(readxl)
d <- read_excel("data")

# column selection
dd <- d[,6:25,]
#setting colors
grp <- d$GRP
riv <- d$Rivers
colv <- c("deepskyblue", "darkgoldenrod1")
Colv <- colv[grp] # all colors repeated



dda <- as.data.frame(dd)
majorel <- c(1,2,3,4,5,6,7,8,9,10)
traceel <- c(11,12,13,14,15,16,17,18,19,20)



#Principal Component Analysis
library(robCompositions)
library(robustbase)


# compute MCD for grp=1 observations

duse <- pivotCoord(dda[,majorel])
mcd <- covMcd(duse[grp=="1",])
mds <- sqrt(mahalanobis(duse,mcd$center,mcd$cov))
par(mfrow=c(2,1))
par(mar=c(3,5,1,4))
plot(mds,col=Colv, pch=16, cex=1.4)
crit <- sqrt(qchisq(0.975,df=ncol(duse)))
abline(h=crit, col='deeppink3')
lines(mds, col='grey')
points(mds, cex=1.4)
#text((1:length(mds))[riv==1][seq],mds[riv==1][seq],1:16, cex=0.45)



duse <- pivotCoord(dda[,traceel])
mcd <- covMcd(duse[grp=="1",])
mds <- sqrt(mahalanobis(duse,mcd$center,mcd$cov))
par(mar=c(3,5,1,4))
plot(mds,col=Colv, pch=16, cex=1.4)
crit <- sqrt(qchisq(0.975,df=ncol(duse)))
abline(h=crit, col='pink')
lines(mds, col='grey')
points(mds, cex=1.4)
```

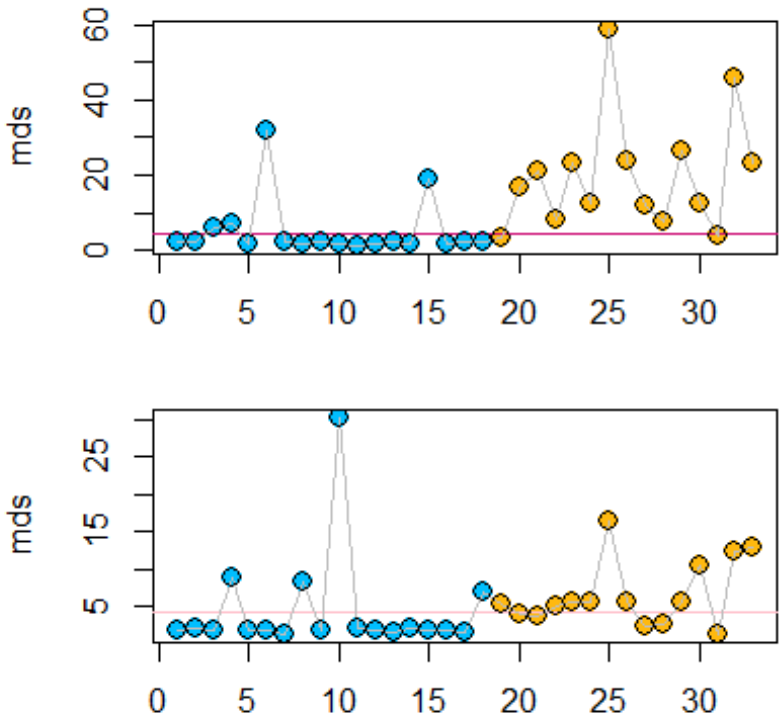
mds
0
20
40
60
0
5
10
15
20
25
30

mds
5
15
25
0
5
10
15
20
25
30

Appendix D

Conference Proceedings

D.1 EGU General Assembly 2020

EGU2020-21502
https://doi.org/10.5194/egusphere-egu2020-21502
EGU General Assembly 2020

Water-sediment interaction in the Arno- and Tiber river catchments (central Italy)

Petra Diendorfer[1], Caterina Gozzi[2], Anna Bauer[1], Antonella Buccianti[2,3], Gerd Rantitsch[1], Robert Scholger[4], Barbara Nisi[3], and Orlando Vaselli[2,3]

[1]Chair of Geology and Economic Geology, Montanuniversität Leoben, Leoben, Austria
[2]Department of Earth Sciences, University of Florence, Firenze, Italy
[3]CNR-IGG Institute of Geosciences and Earth Resources, Firenze, Italy
[4]Chair of Applied Geophysics, Montanuniversität Leoben, Leoben, Austria

The Tiber and the Arno river basins, represent the first (17,156 km^2) and the second (8,228 km^2) largest catchments in the peninsular Italy, respectively. The recent combined sampling (2017-2019) of river waters and sediments in the heterogeneous geological environment of the Apennines enables the assessment of the geochemical and mineralogical interaction between bedrock, river sediments and water. The mineralogical and geochemical composition of the stream sediments are related to the corresponding lithological composition of the hydrological catchment, thus assessing physical weathering within the river basins. On the other hand, chemical weathering is assessed by the analysis of hydrochemical data from the Arno and Tiber rivers and their main tributaries. Locally, anthropogenic processes overprint the natural signature and the magnetic properties of the sediments provide effective data to map those areas. The application of multivariate robust statistical techniques on the combined dataset evaluates the water-sediment interaction and their spatial properties in central Italy. The main goal of this research is to investigate how the linkage between surface waters and steam sediments chemistry can be influenced by catchment-specific properties (e.g. landscape attributes, anthropic impact and climate) through an effective comparative analysis between two of the most important Italian watersheds.